2016

Size, Shape, Composition and Chemical state effects in nanocatalysis

Mahdi Ahmadi
University of Central Florida

STARS Citation

Ahmadi, Mahdi, "Size, Shape, Composition and Chemical state effects in nanocatalysis" (2016). *Electronic Theses and Dissertations, 2004-2019*. 5096.
https://stars.library.ucf.edu/etd/5096

SIZE, SHAPE, COMPOSITION AND CHEMICAL STATE EFFECTS IN NANOCATALYSIS

by

MAHDI AHMADI
M.S. University of Central Florida, 2013
M.S. University of Tehran , 2011

A dissertation submitted in partial fulfillment of the requirements
for the degree of Doctor of Philosophy
in the Department of Physics
in the College of Sciences
at the University of Central Florida
Orlando, Florida

Summer Term
2016

Major Professor: Beatriz Roldan Cuenya

ABSTRACT

The field of nanocatalysis has gained significant attention in the last decades due to the numerous industrial applications of nanosized catalysts. Size, shape, structure, and composition of the nanoparticles (NPs) are the parameters that can affect the reactivity, selectivity and stability of nanocatalysts. Therefore, understanding how these parameters affect the catalytic properties of these systems is required in order to engineer them with a given desired performance. It is also important to gain insight into the structural evolution of the NP catalysts under different reaction conditions to design catalysts with long durability under reaction condition. In this dissertation a synergistic combination of *in situ*, *ex situ* and *operando* state-of-the art techniques have allowed me to explore a variety of parameters and phenomena relevant to nanocatalysts by systematically tuning the NP size, chemical state, composition and chemical environment.

OUTLINE

The outline of this dissertation is as follows. Chapter 1 contain an introduction to the field of nanoparticle catalysis. In Chapter 2, a description of the characterization techniques used through this thesis is provided. Chapter 3 describes the nanoparticle synthesis method used namely, inverse micelle encapsulation that has been used in this report.

Chapter 4 presents an investigation of the structure and chemical state of size-selected platinum nanoparticles supported on γ-Al_2O_3 during the oxidation of methanol under oxygen-rich reaction conditions following both oxidative and reductive pretreatments. X-ray absorption near-edge structure (XANES) and extended x-ray absorption fine-structure (EXAFS) spectroscopy measurements reveal that in both cases, the catalyst is substantially oxidized under reaction conditions at room temperature and only becomes partially reduced when the reactor temperature is raised to 50°C. Reactivity tests show that at low temperatures the pre-oxidized catalyst is more active than the pre-reduced catalyst. We conclude that the differences in reactivity can be linked to the formation and stabilization of distinct active oxide species during the pretreatment and under reaction conditions.

In Chapter 5, the morphology of 3D palladium and platinum NP catalysts supported on TiO_2(110) was investigated using scanning tunneling microscopy (STM). Well defined Pd and Pt NPs were synthesized via inverse micelle encapsulation. The initially spherical NPs were found to become faceted and form an epitaxial relationship with the support after high temperature annealing (e.g. 1100 ºC). Shape-selection was achieved for almost all Pd NPs, namely, a truncated octahedron shape with (111) top and interfacial facets. The Pt NPs were however found to adopt a variety of shapes. The epitaxial relationship of the NPs with the support was evidenced by the alignment of the cluster's edges with TiO_2(110)-[001] atomic rows and was found to be responsible for the shape control.

Chapter 6 describes how the size of NPs supported on TiO_2 affects the NP- support interaction. The NP-support adhesion energy calculated based on STM data was found to be size-dependent, with large NPs (e.g. ~6 nm) having lower adhesion energies than smaller NPs (e.g. ~1 nm). This phenomenon was rationalized based on support-induced strain that for larger NPs favors the formation of lattice dislocations at the interface rather than a lattice distortion that may propagate through the smaller NPs. In addition, identically prepared Pt NPs of the same shape were found to display lower adhesion energy as compared to Pd NPs. While in both cases, a transition from lattice distortion to interface dislocations is expected to occur with increasing NP size, the higher elastic energy in Pt leads to a lower transition size, which in turn lowers the adhesion energy of Pt NPs as compared to Pd.

Chapter 7 presents an investigation of the evolution of the structure, composition, and catalytic reactivity of shape-selected octahedral Pt-Ni bimetallic NPs in response to various thermal, gas-phase, and electrochemical environments. We follow the changes of the near-surface composition of the PtNi(111) facets after exposure to oxygen and hydrogen gas environments using x-ray photoelectron spectroscopy (XPS) and contrast those to surface compositional transformations during electrochemical potential cycling pretreatments in alkaline and acidic environments. Acidic electrochemical environments dissolve Ni species from the surface leaving behind a Pt rich interface. Oxygen and hydroxide (alkaline) environments promote the surface segregation of Ni(II) oxide species, which, owing to their oxophilicity and resulting affinity to water activation, show a significant promotion of the electrochemical CO oxidation and the electrocatalytic hydrogen evolution. A bifunctional synergetic effect between surface Pt atoms adjacent to Ni oxide domains was proposed.

In Chapter 8 a study of the morphological and chemical stability of shape-selected octahedral $Pt_{0.5}Ni_{0.5}$ nanoparticles (NPs) supported on highly-oriented pyrolytic graphite (HOPG) is presented. *Ex situ* atomic force microscopy (AFM) and *in situ* XPS measurements were used to monitor the mobility of $Pt_{0.5}Ni_{0.5}$ NPs and to study long range atomic segregation and alloy formation phenomena under vacuum, H_2, and O_2 atmospheres. The chemical state of the NPs was found to play a pivotal role in their surface composition after different thermal treatments. In particular, for these *ex situ* synthesized NPs, Ni segregation to the NP surface was observed in all environments as long as oxygen species were present. In the presence of oxygen, an enhanced Ni surface segregation was observed at all temperatures. In contrast, in hydrogen and vacuum, the Ni outward segregation occurs only at low temperature (<200-270°C), while PtO_x species are still present. At higher temperatures, the reduction of the Pt oxide species results in Pt diffusion towards the NP surface and the formation of a Ni-Pt alloy. A consistent correlation between the NP surface composition and its electrocatalytic CO oxidation activity was established.

In Chapter 9 the chemical and morphological stability of size- and shape-selected octahedral PtNi NPs was investigated after different annealing treatments up to a maximum temperature of 700°C in vacuum and under 1 bar of CO. AFM was used to examine the mobility of the NPs and their stability against coarsening, and XPS to investigate the surface composition, chemical state of Pt and Ni in the NPs and thermally and CO-induced atomic segregation trends. Exposing the samples to 1 bar of CO at room temperature before annealing in vacuum was found to be effective at enhancing the stability of the NPs against coarsening. In contrast, significant coarsening was observed when the sample was annealed in 1 bar of CO, most likely as a result of $Ni(CO)_4$ formation.

Sample exposure to CO at room temperature prior to annealing lead to the segregation of Pt to the NP surface. Nevertheless, oxidic PtOx and NiOx species still remained at the NP surface, and, irrespective of the initial sample pretreatment, Ni surface segregation was observed upon annealing in vacuum at moderate temperature (T<300°C). Interestingly, a distinct atomic segregation trend was detected between 300°C-500°C for the sample pre-exposed to CO, namely, Ni surface segregation was partially hindered. This might be attributed to the higher bonding energy of CO to Pt as compared to Ni. Annealing in the presence of 1-bar CO results in the occupation of the NP surface by Ni atoms at 400°C as a result of $Ni(CO)_x$ formation. Above 500°C, and regardless of the sample pretreatment, the diffusion of Pt atoms to the NP surface and the formation of a Ni-Pt alloy is observed.

Chapter 10 contains the summary and outlook of the thesis.

This dissertation is dedicated to my parents and my wife who were extremely patient and supportive with me during all these years.

ACKNOWLEDGMENT

My deepest thanks is to my advisor Prof. Beatriz Roldan Cuenya for her support and guidance during my academic and personal Phd life. Prof. Roldan gave me the freedom to approach different project in my own way, which gave me the opportunity of tackling problems independently, while at the same time her guidance in critical moments wouldn't allow me to get lost in the passage. Her broad mindedness toward diverse ideas taught me the team working and tolerance in a research group. Her hard working, honesty and commitment to scientific values would be my example of a successful researcher. I am also thankful to her for carefully reading, revising and commenting my manuscripts.

I want to also thank my group members Dr. Farzad Behafarid, Dr. Luis Ono, Dr. Lindsay Merte, Hemma Mistry, Dr. Estephania Lira, Sudeep Pandey, Jeronimo Matos, Dr. Ioannis Zegkinoglou, Dr. Nuria Jimenez Divins, Dr. Ilya Sinev, Miquel Bernal Lopez, Sebastian Kunze, Michael Meischein for continuous scientific discussions and collaborations and above all for their life lasting friendship. I want to specially thank Farzad for helping me to adapt quickly to the group and teaching me how to work with UHV systems and to use all the measurement techniques in the lab.

Thanks also to our collaborators, Prof. Peter Strasser, Prof. Lee Chow and Dr. Oleg Lupan for providing me with their support and scientific insight.

I would like to express my thanks to my committee members Prof. Abdelkader Kara, Prof. Talat Rahman, Prof. Kevin Coffey for taking time to evaluate my work and for their constructive comments and discussions. Additionally I would also like to thank Prof. Talat Rahman for her support during my research travel to Germany.

My wholehearted thanks go to my parents for their tremendous sacrifice to ensure that I get excellent life and education. I owe them my life forever.

I would also thank my brother and sister, Amin and Elahe, they both had enormous impact on my education, both Amin and Elahe had help me a lot with all physics courses during my bachelor and master back in Iran. Other than being awesome siblings they were the best tutors that I could always have at home.

I would like to thank my wife and my best friend, Parinaz, for her patience, support during my Phd program and for bringing the joy to my heart.

TABLE OF CONTENTS

LIST OF FIGURES

CHAPTER 1: INTRODUCTION

Understanding the interaction between nanocatalysts and reactants is the first fundamental step for the rational design of high quality catalyst with particular reactivity, selectivity and stability. Such understanding can be achieved by the systematic investigation of a variety of catalyst properties such as their size, shape, composition and chemical state. A deconvolution of the individual role of each of the former parameter is therefore required.

The most important property of NPs which has been widely studied is their size.[1, 2] The NPs size can affect their catalytic activity by influencing the number of low coordinated atoms, their shape, electronic structure and stability. It has been shown that the binding energy of many adsorbates also depend on the NP size.[3-7] Furthermore the size of NPs can affect the NP interaction with its support.[8]

Another parameter that can affect nanocatalysts activity is the NP shape. Since the bonding energy of many reactants depends on the facet orientation, different shapes with different surface facets may affect the activity of NP catalysts toward structure-sensitive chemical reactions.[9-11] In addition the NP shape can affect the catalytic activity by changing the number of active surface atoms and the number of atoms in contact with the support.[12-14]

The chemical state of catalysts can also be used to tune their activity. It has been shown that oxidized catalyst may display enhanced catalytic activity for some reactions, while for others it could be detrimental.[15] The oxidation state may affect reactivity by affecting the adsorbate binding energy. In some oxidation reactions higher activity of oxidized catalyst can be explained through the Mars-Van-Krevelen (MVK) mechanism which suggests consumption of lattice oxygen and their substitution by oxygen from gas phase O_2 dissociation.[16]

To reduce the price and increase the activity of the catalyst another parameter for tuning catalytic performance is the modification of the NP composition. It was shown that in some cases bimetallic catalysts have higher resistance toward poisoning as compared to their monometallic counterparts.[17, 18]. Furthermore changing the metal bond length due to the mixture of metals and consequently changing their electronic structure is another way of tuning nanocatalyst reactivity.[19, 20]

It should be mentioned that although well-defined properties of nanocatalyst is very important in designing low price high quality catalysts, the evolution of nanocatalysts under reaction condition which can cause deactivation of the catalysts is another concern that should be addressed. The evolution of nanocatalysts include the sintering of NPs, the change of surface composition, the variation of the morphology and the oxidation state of catalysts. Therefore investigating the evolution of the nanocatalysts using *operando* and *in situ* techniques is important for understanding the behavior of active catalysts in response to their environment.

In the beginning of this dissertation we present a summary of measurement techniques that have been used. Scanning tunneling microscopy (STM) and Atomic force microscopy (AFM) are the techniques that have been used for the direct imaging of the surface morphology and structure and X-ray photoelectron spectroscopy (XPS) is a surface sensitive technique used for characterizing the chemical state and composition of the elements present on the surface.

The inverse micelle encapsulation method has been used for fabrication of the NPs. Using this method, the NPs can be deposited on the planar substrates using dip coating and on powder substrates by impregnation. The synthesis method is described in Chapter 3.

As it was mentioned, the evolution of the nanocatalysts during the reaction is an exciting aspect of nanocatalysts to be considered. In Chapter 4, the evolution of the chemical state of Pt NPs supported on γ-Al_2O_3 is discussed during methanol oxidation.

In Chapter 5, STM measurements are used to study the thermodynamically stable shape of Pt and Pd NPs on TiO_2. It was found that a truncated octahedron with (111) top and interfacial facets is the most stable shape of Pd NPs on TiO_2. This observation has been explained based on the highest adhesion energy of the (111) interfacial facet to the TiO_2 (110) lattice. Chapter 6 is dedicated to investigate the interaction of Pt and Pd NPs with TiO_2 (110) as a function of their size by using the reconstructed models of the NPs extracted from STM images. Also for a given size, higher adhesion energy was found for Pd NPs as compared to Pt NPs due to the higher rate of increase in the elastic energy of Pt, which results in a preference of the NPs for lateral as compared to vertical growth.

In Chapter 7 the surface composition and stability of octahedron PtNi NPs supported on HOPG was investigated under gas phase and liquid electrochemical environment. It was found that hydroxide anions stabilized the Ni surface while an acidic electrochemical environment caused selective removal of Ni atoms. Chapter 8 discusses segregation phenomena in PtNi nanoparticles supported on HOPG under different gaseous environments, while CO electrooxidation was used as a model reaction to display the effect of different pre-treatments in different gaseous atmospheres on the catalytic activity. Chapter 9 is devoted to the investigation of atomic segregation and the morphological stability of octahedral PtNi NPs in the presence of CO.

CHAPTER 2: MEASUREMENT TECHNIQUES

2.1. Scanning tunneling microscopy (STM)

2.1.1. Fundamentals

Scanning tunneling microscopy (STM) is an instrument for surface imaging with lateral resolution of 0.1 nm and depth resolution of 0.01 nm. However achieving such high resolution is challenging and requires a sharp and stable tip, and vibrational control, and a stable sample surface.

Quantum tunneling is the basic principle of STM. To examine a surface, a conducting tip is brought very near to the surface, the bias voltage applied between the surface and the conducting tip cause a net tunneling current through the barrier. This behavior could be described by the Schrodinger equation as following:

$$-\frac{\hbar}{2m}\frac{\partial^2\psi(z)}{\partial z^2}+U\psi(z)=E\psi(z) \tag{2.1}$$

Where $\hbar$ is the reduced plank constant, m is the mass of electron and z is the position. Since E<U(z) in the case of an electron inside a barrier, the wave function would be a decaying wave,

$$\psi(z)=\psi(o)e^{\pm kz} \tag{2.2}$$

And the current in the case of small bias would be:

$$I \propto V\rho_s(0,E_f)\exp(-\frac{\sqrt{8m\varphi}d}{\hbar}) \tag{2.3}$$

Where Φ is the sample work function, ρ_s is the local density of electronic states (LDOS), V is the bias voltage and d is the distance between the tip and the surface. Due to the exponential behavior of the above formula, a small variation in the distance significantly affects the tunneling current and that is the reason for the very high vertical resolution of STM.

2.1.2. Instrumentation

A schematic of STM has been shown in figure 2.1. The components of STM are tip, inchworm motor, piezoelectric controlling height and x, y scanner and computer.

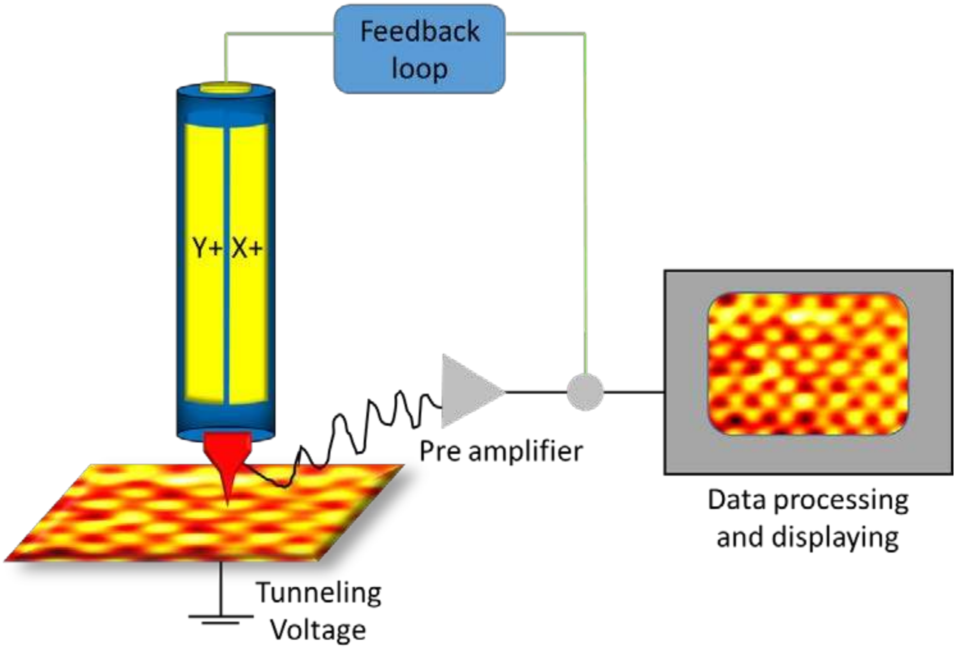

Figure 2. 1. Schematic of a scanning tunneling microscope.

The tip is often made of tungsten or Pt-Ir. A tungsten tip can be made through the chemical etching of tungsten wire while Pt-Ir tips can be made by cutting Pt-Ir wires at a glazing angle. The inchworm motor is responsible for bringing the tip near to the surface and it is made of three piezos (1 vertical and two clutch piezos) mounted inside a cylinder.

The inchworm motor brings the tip toward the sample until it detects the tunneling current. At this point another set of piezos is responsible for controlling the tip position in X, Y and Z direction. Four Piezos (X+,X-,Y+,Y-) are bending the tip in the X and Y direction in the sample plane while the piezo on top of the scanner controls the tip position in the Z direction.

2.1.3. STM images

Two examples of STM images on HOPG and TiO_2 (110) are shown in Figure 2.3. The TiO_2 atomic rows with the 13Å distance between can be seen in figure 2.3 (b).

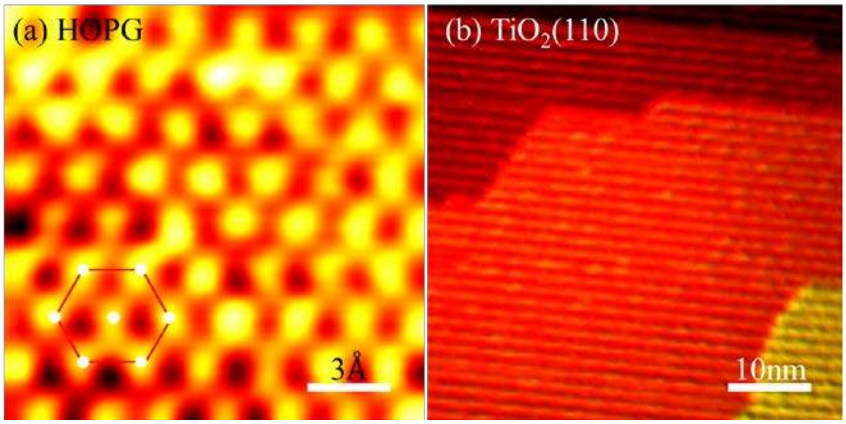

Figure 2. 2. STM images of (a) HOPG showing atomic resolution and (b) a TiO_2 (110) surface with (1×2) surface reconstruction.

2.2. Atomic force microscopy (AFM)

2.2.1. Fundamentals

Atomic force microscopy (AFM) is another technique for surface imaging with typical resolution of a fraction of a nanometer down to atomic resolution. One of the components of an AFM set up is a cantilever, with a sharp tip at its end. The interaction between the tip and the surface could be used to acquire an image of the topography of the sample surface.

According to Hooke's law, when the tip is brought close to the surface, the force between the sample surface and the tip leads to the vertical and lateral deflection of the cantilever. The angular deflection of the cantilever can be measured by an optical lever. The optical lever is made of a quadrant photodiode detector and a laser. The laser beam strikes the detector after reflecting from the cantilever, Figure 2.3. The position of the laser beam can be measured on the detector and thus the cantilever deflection.

AFM usually operates in one of the three modes, (i) contact mode, (ii) tapping mode, (iii) non-contact mode.

In contact mode the tip moves on the surface and the scanner feedback loop changes the height of the cantilever to have a constant deflection. Measuring the height of the cantilever at each point allows the software to reconstruct the morphology of the sample surface. The problem with the contact mode is that in ambient pressure most samples would be covered with a thin layer of liquid which interrupt the scanning of the surface. The tapping mode was developed to resolve this problem. In tapping mode, the cantilever is driven to oscillation near its resonance frequency with a constant amplitude through a piezo in the cantilever holder. As the tip gets closer to the sample surface the interaction between the sample and the tip causes changes in the amplitude of the oscillation and the feedback loop changes the height and follows the surface to keep the amplitude constant. In non-contact mode the tip does not touch the sample, while it oscillates at resonance frequency. Due to the van der Waals forces the resonance frequency of the cantilever decreases. Again, this decrease in the resonance frequency combined with the feedback loop system keeps the tip at constant height to the sample surface, and measuring the sample to tip distance at each point leads to the topographic image of the surface.

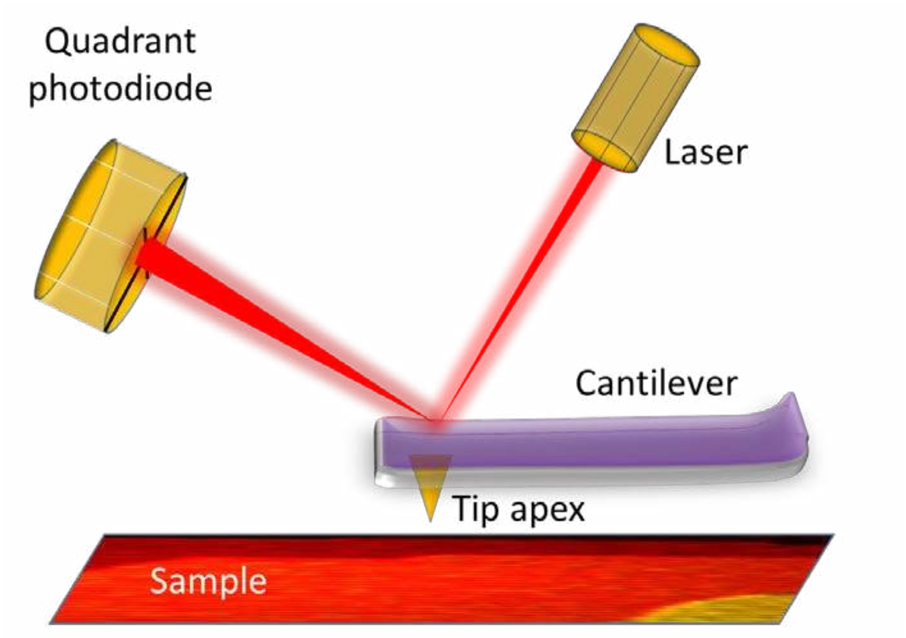

Figure 2. 3. Schematic of an AFM setup with a laser and a cantilever.

2.2.2. AFM images

Figure 2.4 displays the AFM image of PtNi NPs supported on HOPG acquired at room temperature in tapping mode.

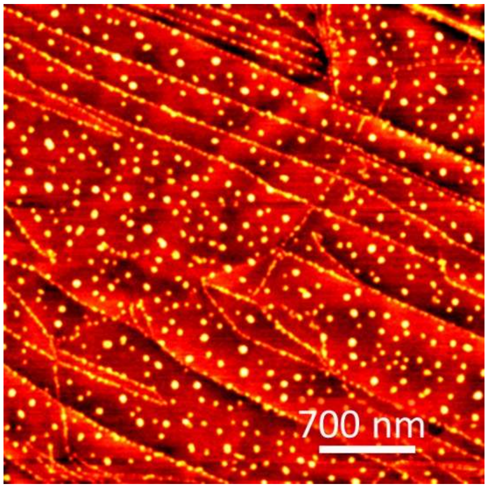

Figure 2. 4. AFM image of PtNi NPs supported on HOPG acquired in tapping mode.

2.3. X-ray Photoelectron spectroscopy (XPS)

2.3.1. Fundamentals

X-ray photoelectron spectroscopy (XPS) is a surface sensitive spectroscopic technique. XPS spectra are acquired by irradiating the sample with X-rays and measuring the energy and number of photoelectrons that come out of the surface. Although the penetration depth of X-rays in samples can be few micrometers, however due to the short inelastic mean free path of electron (~ nm) the electrons that could escape from the surface are coming from the top 10 nm of the surface.

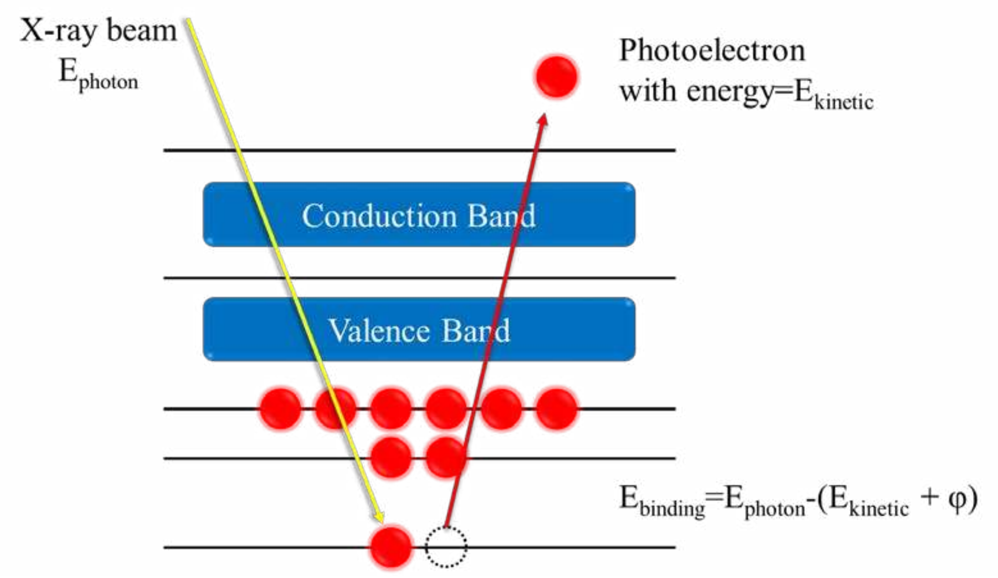

Figure 2. 5. Schematic of the XPS process.

XPS can be used to analyze the elemental composition, chemical state and the electronic state of the surface of materials. Since the energy of the X-ray is known (i.e,Al Kα X-rays 1486.7 eV) and the energy of the photoelectrons is measured by an electron analyzer, then the electron binding energy can be found using the following equation:

$E_{binding}= E_{photon}- (E_{kinteic}+\Phi)$

Where $E_{binding}$ is the binding energy of the electron, E_{photon} is 1486.7 eV in our system but it can be different in different systems and Φ is the work function which is an adjustable factor and it depends on the sample and type of detector.

Due to the unique set of electron energies of each element, XPS can be used to determine the elemental composition on the surface. Also by considering the sensitivity factor of each element the relative concentration of the given element can be extracted.

XPS is also sensitive to the electronic and chemical state of the elements. For example, in most cases the binding energy of oxidized elements is higher than that of reduce ones. The higher binding energy is due to higher electronegativity of oxygen that attracts the electrons, leading to a lower density of electrons around the nucleolus, which increases the binding energy of the remaining electrons.

2.3.2. Instrumentation

The component of XPS are an X-ray source, a UHV chamber, an electron detector and an energy analyzer system, and an X-ray monochromator.

The X-rays are produced by electron bombardment of an anode (Al in this case). To have X-ray with narrower energy width, a quartz monochromator can be used, which leads to X-rays with an energy resolution in the order of FWHM=0.2 eV. The photoelectrons that escaped from the surface are collected and directed to the hemispherical electron analyzer by a set of magnetic and electrostatic lenses. The electrostatic field within the electron analyzer only allows electrons of a given energy to arrive to the detector. The detector is made of 5 channeltrons that can induce ~10^8 for each electron that reaches to them. The XPS spectra can be acquired by sweeping the voltage of the electron analyzer and by sorting the photoelectrons as a function of their energy.

2.3.3. XPS spectra

Figure 2.6 shows high resolution XPS spectra of the Ti-2p and Pd-3d regions of a sample with Pd NPs supported on TiO_2 (110) acquired at room temperature as-prepared and after annealing in vacuum at 1100°C.

The data were fitted using CASA XPS sofwere. As can be seen the Ti-2p spectrum has two components, $2p_{3/2}$ and $2p_{1/2}$ due to spin-orbit splitting. Since the degeneracy is four for $2p_{3/2}$ and is two for $2p_{1/2}$, the ratio of the area under the $2p_{3/2}$ and $2p_{1/2}$ has been constrained to be 2. The different chemical state can be seen for the Ti-2p evolved after annealing at 1100°C, and the presence of the Ti^{3+} peak shows the partial reduction of Ti atoms.

The Pd-3d region also has two components, $3d_{5/2}$ and $3d_{3/2}$ due spin-orbit splitting. In addition because of the presence of Pd, Pd^{2+} and Pd^{4+} in the sample, the Pd core level region was fitted with three doublets. In the as prepared sample due to the oxygen plasma treatment, the Pd atoms are all oxidized, while after annealing at 1100°C only metallic Pd atoms can be observed.

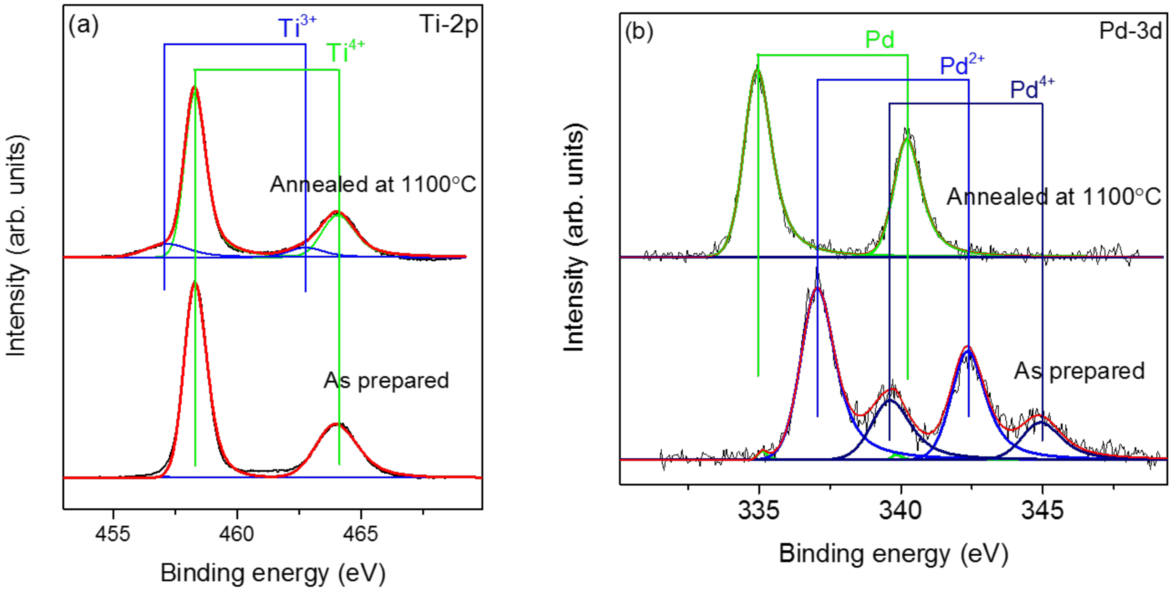

Figure 2. 6. XPS spectra of (a) Ti-2p and (b) Pd-3d core-level regions of Pd NPs on TiO_2 (110) acquired at room temperature on the as-prepared sample (O_2 plasma treated) and after annealing at 1100C in UHV. The Ti-2p region has been fitted with two doublets corresponding to Ti^{3+} ($2p_{3/2}$, 457.2 eV) and Ti^{4+} ($2p_{3/2}$, 458.3 eV). The presence of Ti^{3+} in the sample after the thermal treatment is due to the increase in oxygen vacancies on the surface. The Pd-3d region of the as prepared sample has been fitted with three doublets corresponding to Pd metallic ($3d_{5/2}$, 335 eV), Pd^{2+} ($3d_{5/2}$, 337 eV), Pd^{4+} ($3d_{5/2}$, 339.6 eV). After annealing at 1100°C, just metallic Pd has been observed, which rules out the formation of a Pd-Ti alloy after annealing in UHV.

CHAPTER 3: NANOPARTICLE SYNTHESIS METHOD

3.1. Inverse micelle encapsulation

Inverse micelle encapsulation [21-29] has been used for NP preparation. This method allows a high degree of control over the NP size, shape, and dispersion on the support, and is suitable for being scaled up to large substrate areas and material quantities [30-32]. Nanometer-sized cages can be obtained by dissolving nonpolar-polar PS-P2VP diblock copolymers, [poly(styrene)-block-poly(2-vinylpyridine)], in a selective nonpolar solvent (toluene). The polar ends of the block copolymer spontaneously form a cavity with nonpolar ends pointing out into the solvent. Self-confined mono- and multimetallic NPs are obtained by loading these micelles with metal salts (such as $NiCl_2.6H_2O$, $CuCl_2.2H_2O$, $Pd(O_2CCH_3)_2$ and H_2PtCl_6), Figure. 3. 1 (a). This approach allows the self-organized generation of monodispersed NPs with average heights in the range of 0.5 nm to 50 nm. The NP size can be tuned in two ways: i) using polymers with different head sizes (P2VP), and ii) by changing the metal-salt/polymer core ratio. The distance between the NPs can be varied by changing the length of the polymer tail (PS) (e.g. 10-200 nm). Hexagonal NP arrays on a planar substrates can be obtained after substrate dip-coating into the metal salt-micellar solution. The NP shape can be tuned by changing the metal loading [33, 34] inside a given micellar cage as well as by controlling the NP size [35] and by selecting appropriate substrate orientations. Subsequently, the encapsulating polymer can be removed by an O_2/H_2-plasma etch, Figure. 3.1 (b).

In addition to NP films supported on single crystals, powder catalysts prepared by impregnating the nanocrystalline metal oxide substrates such as Al_2O_3 and Ce_2O_3 with the micellar solution and subsequently drying the solvent. The organic ligands were then removed by prolonged annealing treatments at 375˚C for 18h in an O_2 environment, Figure. 3.1(c).

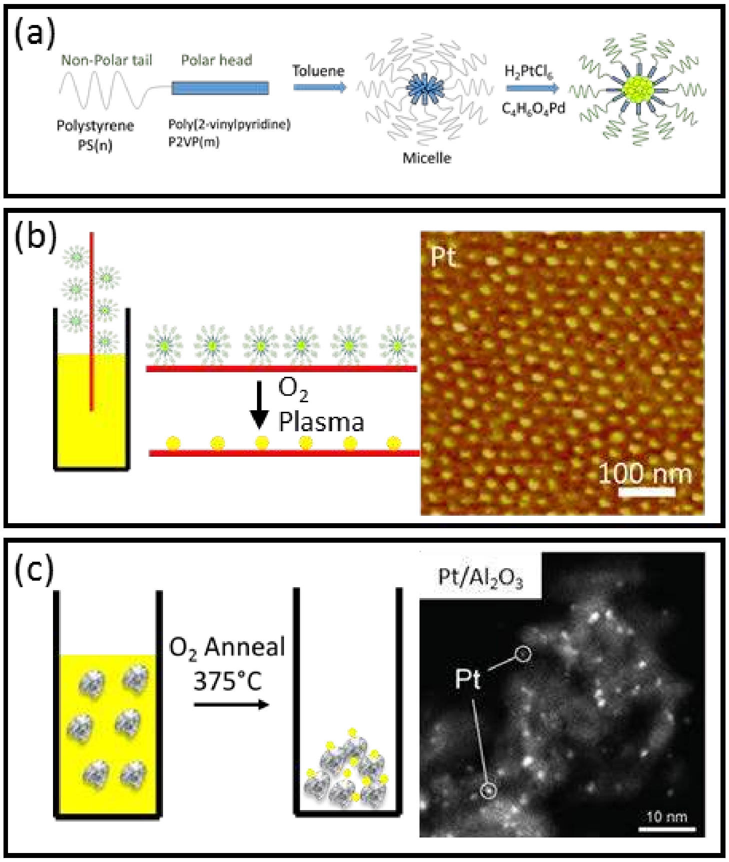

Figure 3. 1. Schematic description of inverse micelle encapsulation NP (a) solution (b)schematic description and AFM image of Pt NPs deposited on TiO_2 (110) and (c) schematic description and TEM image of Pt NPs supported on γ-Al_2O_3.

CHAPTER 4: CORRELATING CATALYTIC METHANOL OXIDATION WITH THE STRUCTURE AND OXIDATION STATE OF SIZE-SELECTED Pt NANOPARTICLES

4.1. Introduction

The partial and total catalytic oxidation of methanol are important chemical processes, the former being employed in the synthesis of industrially-relevant compounds like formaldehyde [36, 37] and methyl formate,[38, 39] and the latter in the elimination of these toxic chemicals, along with other volatile organic compounds (VOC), from exhaust gases.[40-42] While partial oxidation reactions are carried out using coinage metals or various metal oxides,[43] total oxidation is typically achieved with platinum and/or palladium, which are able to convert methanol, higher alcohols, hydrocarbons and carbon monoxide to CO_2 with high efficiencies at relatively low temperatures. Although occurring in a rather different environment, the electrocatalytic oxidation of methanol, which proceeds over Pt-based catalysts, is also relevant. The rate of this process is a limiting factor in the performance of direct methanol fuel cells (DMFC), which produce electricity from liquid fuel without the need for reforming.[44, 45]

Despite having been studied for decades, some controversy exists regarding the mechanisms of oxidation reactions over platinum, particularly regarding the formation and participation of oxide phases in the reaction process. On one hand, formation of surface oxides has long been believed to cause deactivation of Pt catalysts, for example in the oxidation of alcohols to aldehydes and ketones.[46-48] On the other hand, chiefly in the context of CO and CH_4 oxidation, studies on single crystal samples and real catalysts have suggested that oxides may form under reaction conditions which do not hinder the oxidation reaction, but in fact enhance the activity or modify the selectivity.[49-52] Although the topic remains a matter of debate,[53, 54] *operando* studies of NP samples on high-surface-area supports have supported the idea that in some cases surface oxides might enhance the activity in oxidation reactions.[55-59]

One of the primary limitations in the study of supported catalytic materials under realistic reaction conditions is the complexity of such materials and the resulting difficulty in characterizing them in detail. An emerging, successful approach to reducing the complexity of such materials, enabling more detailed characterization, without sacrificing the direct applicability of the results to commercially relevant chemical processes, is to use NP synthesis techniques that produce catalysts with well-defined sizes and shapes.[60] Taking this approach, we have used reverse micelle NP synthesis to study methanol oxidation over a $Pt/\gamma\text{-}Al_2O_3$ catalyst, with particular attention to the evolution of the structure and oxidation state of Pt under reaction conditions. Based on the knowledge of the chemical state of the catalyst at work which can be achieved via X-ray absorption fine-structure spectroscopy (XAFS), the effect of oxidative and reductive pretreatments on the catalyst's activity and selectivity will be discussed.

4.2. Experimental methods

The Pt-loaded micelles were synthesized by dissolution of H_2PtCl_6 into a solution of polystyrene-b-poly(2-vinylpyridine) [PS(27700)-b-P2VP(4300)] block copolymer (Polymer Source, Inc.) in toluene (50 mg/ml). This results in reverse micelles with the Pt salt dissolved in the P2VP core. The quantity of platinum salt added was chosen to give a Pt:P2VP molar ratio of 0.2. The mixture was stirred for 2 days to ensure complete dissolution and then filtered. The formation of uniform micelles was checked by dip-coating a natively-oxidized Si wafer in the micellar solution and imaging the wafer via AFM. The solution was then mixed with a commercial nanocrystaline γ-Al_2O_3 powder (Inframat Advanced Materials, ~150 m^2/g) to yield a nominal Pt loading of 1%. The toluene was evaporated under mechanical agitation at 50 °C. The polymer was removed by calcination in 70% O_2 (balanced with He) at 375 °C for 24h. Complete removal of the polymer was confirmed by checking the C-1s XPS signal, which showed only small intensity attributable to adventitious carbon accumulated during the brief exposure of the sample to air in the course of its *ex situ* transfer to the XPS chamber.[12, 61]

AFM measurements were conducted in tapping mode with a Veeco Multimode microscope. XPS measurements were conducted using a monochromatic Al-K_α x-ray source (1486.6 eV) and a Phoibos electron energy analyzer (SPECS, GmbH). Binding energies were referenced to the Al-2p photoemission peak of Al_2O_3 at 74.3 eV. Pt-4f photoemission peaks were not detectable for this sample due to their coincidence with the Al-2p peaks of the support, so the Pt-4d region was used instead to characterize the Pt oxidation state. High-angle annular dark field scanning transmission electron microscopy (HAADF-STEM) measurements were conducted after the EXAFS experiments using a JEOL 2100F TEM/STEM operated at 200 kV. The TEM samples were prepared by making an ethanol suspension of the Pt/γ-Al_2O_3 powder and placing a few drops of this liquid onto an ultrathin C-coated TEM grid. The probe size of the STEM mode is about 0.2 nm. The Pt NP diameters were determined by measuring the full width at half maximum of the HAADF intensity profile across the individual Pt NPs.

Catalytic tests were performed at atmospheric pressure in a vertically-mounted quartz tube continuous flow reactor with either 50 mg of pure Pt/γ-Al_2O_3 catalyst or 1 mg Pt/γ-Al_2O_3 diluted with 200 mg α-Al_2O_3, in both cases supported by a quartz wool plug. The reactant mixture consisted of 4% O_2 and 0.15% methanol by volume, balanced with He. The methanol was introduced to the mixture by passing He gas through a bubbler at ambient temperature. Gas concentrations were varied using mass flow controllers (MKS) and the total flow rate was set to 50 sccm. Prior to catalytic testing, the catalyst was first reduced in H_2 (50% in He) at 240 °C for 30 min. To test the influence of the catalyst oxidation state on its catalytic activity, the reduction step was followed by an oxidation step in O_2 (70% in He) at 240 °C for 30 min. The methanol, carbon dioxide, and methyl formate concentrations were measured with an online mass spectrometer (Hiden HPR20) sampling the reactor outlet. Conversion versus temperature measurements were carried out in two different ways. For testing the reactivity of the pure catalyst, the catalyst temperature was varied manually between 5°C and 100°C by cooling the quartz reactor cell with isopropanol, passed through a coil wrapped around the reactor tube, and counter-heating with a heating tape powered by a variable-voltage AC transformer. Measurements were made in increasing temperature steps and the conversion was allowed to reach a steady state at each temperature. For testing the reactivity of the diluted catalyst, the temperature was controlled with a tube furnace and a PID controller (Watlow) and ramped from 30°C to 150°C and then back at a rate of 10°C/hour while monitoring the reactant and product concentrations continuously.

XAFS spectra were acquired at the Pt-L_3 edge in transmission mode at beamline X18B of the National Synchrotron Light Source (NSLS I), Brookhaven National Laboratory (BNL). Spectra were recorded from 150 eV below the absorption edge to 1230 eV above the edge ($k_{max} = 18$ Å^{-1}). The reactor used for the *operando* XAFS measurements consisted of a Kapton tube into which 25 mg of undiluted catalyst powder was loaded and held in place by quartz wool plugs, forming a catalyst bed ~10 mm in length. The same space velocity (25 sccm total flow), gas concentrations and pretreatment conditions were used at BNL and UCF for the reactivity measurements. During the XAFS measurements, reactants and products were monitored via an online mass spectrometer (SRS RGA100).

The Athena and Artemis programs[62] were used for normalization, background subtraction, and fitting of the extended X-ray absorption fine-structure (EXAFS) spectra. Theoretical scattering amplitudes and phase shifts used in the fits were calculated with the FEFF8 *ab initio* code[63, 64] using *fcc* Pt to simulate Pt-Pt scattering paths and $Na_2Pt(OH)_6$ to simulate Pt-O scattering paths. To provide absolute energy calibration, the EXAFS spectrum of a Pt foil placed after the sample was measured simultaneously. Energies given in this work are referenced to the first inflection point of the Pt foil spectrum defined to be 11564 eV.

4.3. Results

4.3.1. Sample characterization

An AFM image of the Pt-loaded PS-b-P2VP micelles used as the precursor to prepare the γ-Al_2O_3-supported NP catalyst is shown in Figure. 4. 1(a). The strong quasi-hexagonal ordering and uniform interparticle separation (~27 nm) observed for the dip-coated sample indicate the successful synthesis of monodisperse micelles, consistent with previous reports utilizing this method.[65-67] After impregnating the micelles onto γ-Al_2O_3 powder and removing the polymer by heating in oxygen, the XPS spectrum, showing a Pt $4d_{5/2}$ photoemission peak at 316.9 eV [Figure. 4.1(b)], revealed that the sample contained oxidized platinum.[68] STEM measurements of the sample after the *operando* XAFS experiments revealed small Pt particles with an average diameter of 0.7 nm, distributed with a standard deviation of 0.2 nm [Figure. 4.1(c,d)]. According to our previous work,[61, 69] no sintering is expected after our *in situ* treatments during the XAFS measurements which involved annealing treatments in H_2 and O_2 up to only 240°C and in a mix of methanol and O_2 up to 50°C.[61, 69]

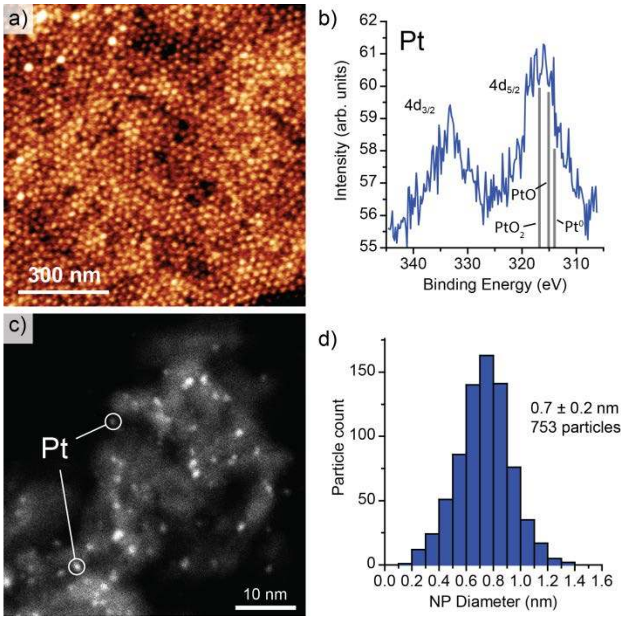

Figure 4. 1. (a) AFM image of the Pt-loaded PS-b-P2VP micellar precursor used to prepare the Pt/γ-Al_2O_3 catalyst used in this study. Micelles were dip-coated onto SiO_2/Si(111) wafer for imaging; polymer ligands were not removed. (b) Pt-4d XPS spectrum of the as-prepared (calcined) Pt/γ-Al_2O_3 catalyst. Binding energies expected for Pt, PtO and PtO_2 are indicated. (c) HAADF-STEM image of the Pt/γ-Al_2O_3 catalyst after ligand removal and after operando XAFS measurements. (d) Particle size distribution extracted from HAADF-STEM measurements.

4.3.2. Catalytic activity

Catalytic activity of the undiluted Pt/γ-Al_2O_3 sample for methanol oxidation was tested at temperatures between 5°C and 100°C following a reductive and an oxidative pretreatment, respectively, and the measured conversions are plotted in Figure. 4. 2. Each experiment was performed twice using untreated catalyst samples and the measurements are plotted together. The only products detected were carbon dioxide (CO_2) and methyl formate ($CHOOCH_3$), as expected from the following reaction pathways:

$2CH_3OH + 3O_2 \rightarrow 2CO_2 + 4H_2O$ (4.1)

$2CH_3OH + O_2 \rightarrow CHOOCH_3 + 2H_2O$ (4.2)

At low temperatures, the total conversion over the pre-oxidized catalyst was significantly higher than that observed for the reduced catalyst. At 5°C, the lowest temperature at which reactivities were tested, the oxidized catalyst converted ~80% of the methanol, while the reduced catalyst only converted ~40%. Product selectivities were also different for the two pretreatments, even after accounting for the differences in overall conversion. Over the pre-reduced catalyst at 80% conversion (observed at about 22°C), selectivity to methyl formate was ~40%, while over the oxidized catalyst at the same total conversion (observed at 5°C), the selectivity to methyl formate was only ~12%.

To obtain more accurate quantitative measurements of methanol oxidation reaction rates above room temperature (RT), we carried out similar reactivity measurements using a diluted sample, consisting of 1 mg Pt/γ-Al_2O_3 mixed thoroughly with 200 mg of α-Al_2O_3. In this experiment, the temperature was ramped linearly from ~30°C to 150°C and back at a rate of 10°C/min. Total conversions as well as CO_2 and methyl formate yields for the pre-reduced and pre-oxidized catalysts during the upward sweep are shown in Figure. 4.3(a) and 3(b), respectively. Measurements were constant above 120°C and were excluded from the plots. At low temperatures (<40°C), the oxidized catalyst was significantly more active than the reduced catalyst; the former showed ~45% conversion at 35°C, while the latter showed negligible conversion below that temperature. At higher temperatures the conversions of both were similar, each exceeding 90% total conversion at ~60°C and showing increased conversion to CO_2 at the expense of methyl formate with increasing temperature. Both the pre-oxidized and pre-reduced catalysts showed high selectivity to methyl formate at low temperature and complete conversion to CO_2 above ~100°C, though the transition point (where conversions to CO_2 and methyl formate are equal) occurs at slightly higher temperature for the reduced catalyst (67°C) compared to the oxidized one (60°C). Reactivity measurements obtained during the subsequent downward temperature sweep are shown in Figure. 4.3(c), with those from the oxidized catalyst overlaid on those from the reduced. Differences in reactivity in this case are almost negligible, indicating that the effect of the pretreatment is lost following the initial temperature ramp to 150°C. The low-temperature reactivities measured during the reverse temperature ramps are intermediate between those obtained for the pre-oxidized and pre-reduced catalysts during the initial upward temperature ramp, each showing conversion of ~20% at 35°C.

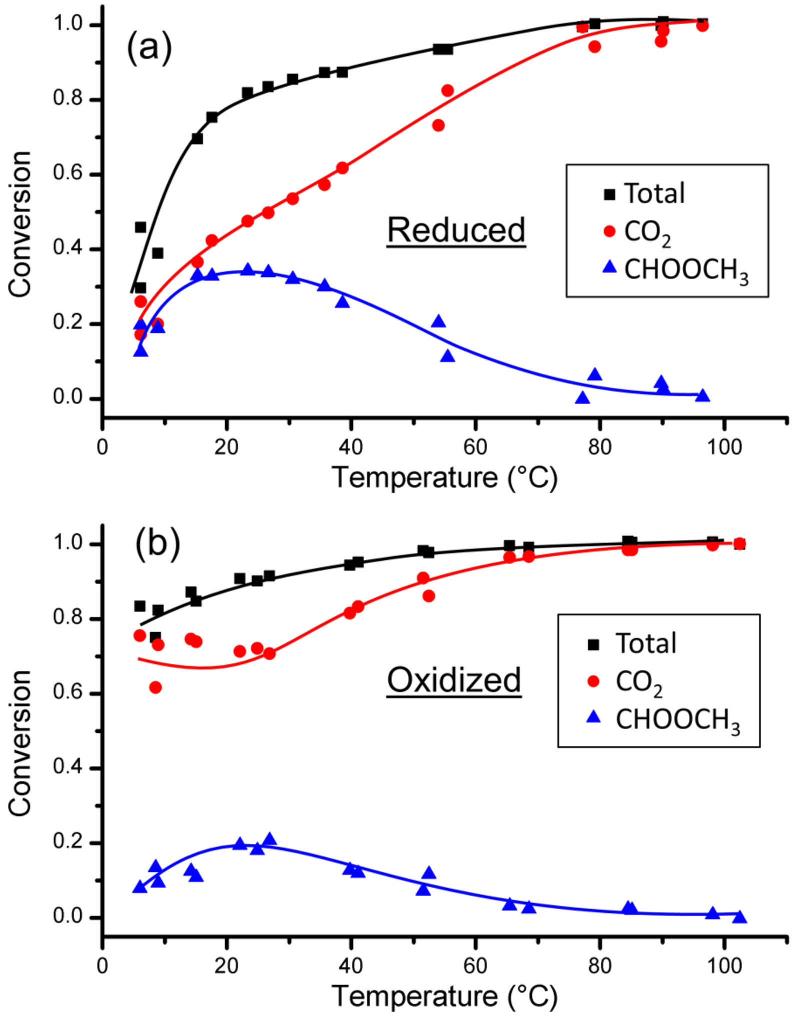

Figure 4. 2. Reactivity of the undiluted Pt/γ-Al_2O_3 catalyst for methanol oxidation following (a) reductive (240 °C in 50% H_2 for 30 mins.) and (b) oxidative (240 °C in 70% O_2 for 30 mins.) pretreatments. Conversion refers to the molar fraction of methanol in the feed converted to a particular product. Plotted points are individual measurements and solid curves are guides to the eye. Carbon dioxide (CO_2) and methyl formate ($CHOOCH_3$) were the only products detected in significant quantities. All data shown correspond to steady-state reaction conditions at each given temperature.

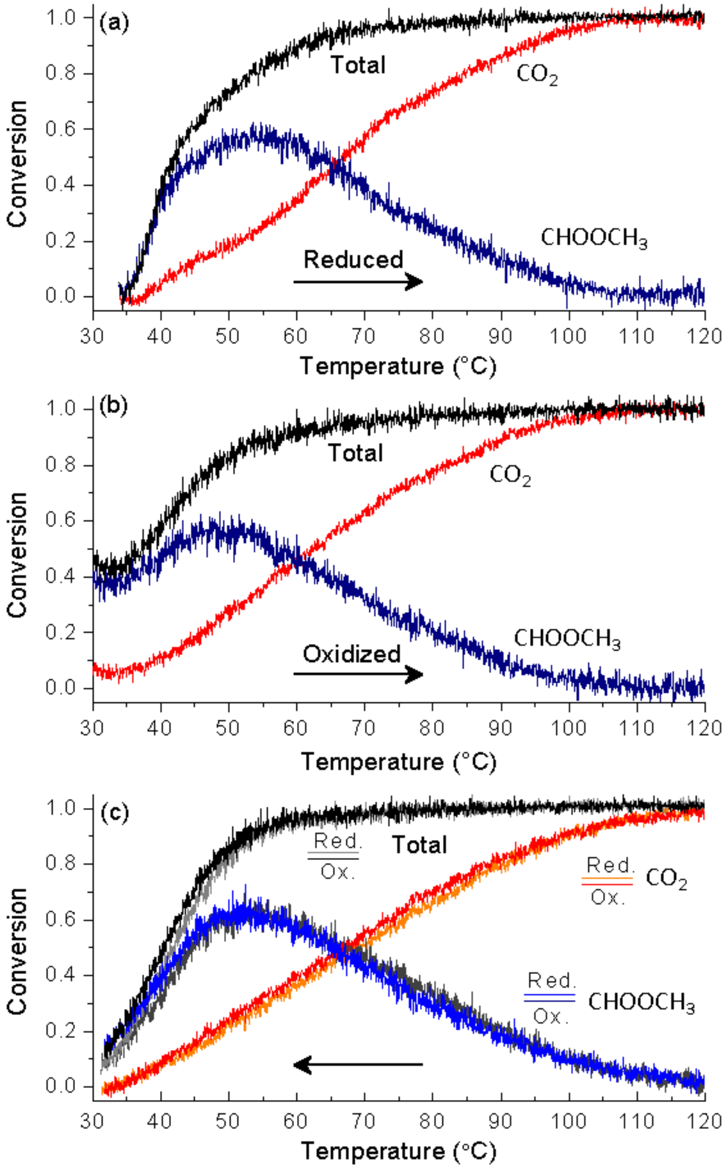

Figure 4. 3. Reactivity of the diluted Pt/γ-Al_2O_3 catalyst for methanol oxidation. Reactivity following (a) reductive, and (b) oxidative pretreatments, measured with increasing temperature. (c) Reactivity following reductive and oxidative pretreatments, measured with decreasing temperature following the measurements shown in (a) and (b).

4.3.3. XANES and EXAFS

Operando XAFS measurements were conducted under similar conditions as the catalytic tests described above. The catalyst was first reduced in hydrogen at 240°C and characterized at 25°C in H_2 in the reduced state. After this, the sample was exposed to the reaction mixture (MeOH and O_2) and measured at 25°C and 50°C under steady-state reaction conditions. After the measurements of the catalyst following the reduction pre-treatment, the same sample was oxidized in O_2 at 240°C and again exposed to the reaction mixture at 25°C and at 50°C.

Figure 4. 4(a) shows X-ray absorption near-edge (XANES) spectra obtained for the catalyst in the reduced state, in the oxidized state, and in the MeOH + O_2 reaction mixture, all at 25°C, following the two different pretreatments. Similar data from a Pt foil are also included for reference. Pt-L_3 absorption spectra exhibit a prominent peak, referred to as a "white line" (WL), just above the edge, resulting from electronic transitions from $2p_{3/2}$ to 5d states. The intensity of the WL is determined primarily by the unoccupied 5d density of states, and thus reflects the average oxidation state of the platinum atoms. The as-prepared sample, measured following a 24-h calcination in O_2 at 375°C, exhibits an intense WL, most likely indicating that a substantial fraction of the platinum in the catalyst is in the form of PtO_2.[70-72] Compared to a metallic platinum foil, the WL of the reduced nanosized catalyst exhibits a shift to higher energy as well as some broadening, due to a combination of NP size/shape effects and changes in the electronic structure resulting from hydrogen chemisorption.[73, 74] Exposure of the reduced catalyst to the oxygen-rich reaction mixture led to an increase in the white line intensity and decrease in the peak energy, indicating the presence of either chemisorbed oxygen on Pt or PtOx species[72]. In the case of the pre-oxidized sample, exposure to the reaction mixture at 25°C led to a very slight decrease in WL intensity,

indicating only a very small change in the oxygen content of the Pt NPs. However, the intensity of the WL of the pre-reduced sample upon exposure to the reaction mixture at 25°C was slightly lower than that of the sample following oxidation at 240°C.

Although the XANES spectra of the pre-oxidized and pre-reduced catalysts under reaction conditions at 25°C are rather similar, the difference between them increased upon heating to 50°C, as shown in Figure. 4. 4(b). In both cases, heating to 50°C led to a decrease in the WL intensity with no change in peak position, but the difference in intensity between the 25°C and 50°C data was significantly larger for the pre-reduced catalyst than for the pre-oxidized catalyst.

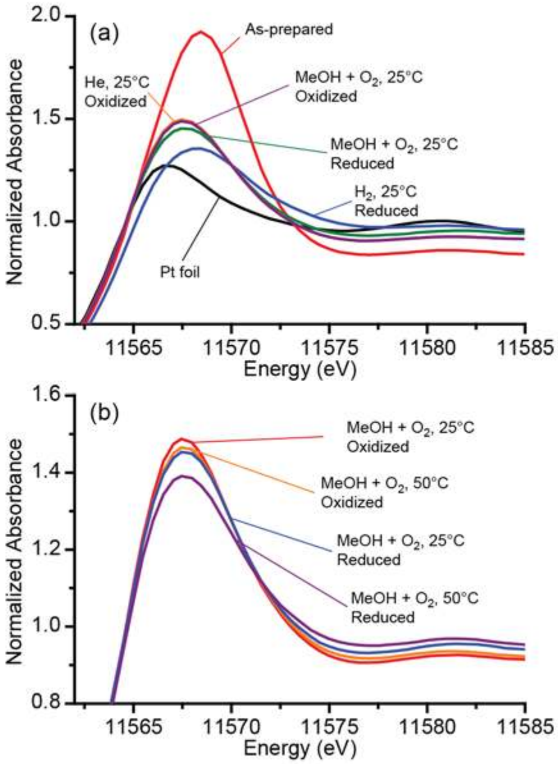

Figure 4. 4. Pt-L_3 XANES spectra of a Pt/γ-Al_2O_3 catalyst acquired following oxidative and reductive pretreatments and under methanol oxidation conditions after these pretreatments. (a) Comparison of spectra acquired under reaction conditions at room temperature beginning in the reduced state (treated in H_2 at 240°C) and an oxidized state (treated

in O_2 at 240°C), respectively. XANES spectra acquired of the as-prepared (oxidized) catalyst and of a bulk Pt foil are shown for reference. (b) Comparison of spectra acquired under reaction conditions at different temperatures.

The EXAFS oscillations extracted from the post-edge region of the Pt-L_3 absorption coefficient result from interference effects due to the scattering of emitted photoelectrons by the surrounding atoms and thus reflect the average local coordination environment of the Pt atoms. Fourier-transformed EXAFS spectra in Figure. 4. 5. exhibit characteristic peaks at positions corresponding roughly (neglecting element- and momentum-dependent phase shifts) to the nearest-neighbor distances in the sample. The EXAFS spectra of the Pt catalyst in the as-prepared, pre-reduced and pre-oxidized initial states (pre-reaction), as well as in the MeOH + O_2 mix at 25°C and at 50°C are shown in Figure. 4. 5, together with the spectrum of a bulk Pt foil. The spectrum of the pre-reduced catalyst shows primarily a peak at ~2.6 Å (phase uncorrected) corresponding to Pt-Pt nearest-neighbor scattering, similar to that of the Pt foil, but reduced in intensity due to the small size (and thus reduced average coordination numbers) and enhanced static atomic disorder of the NPs. The as-prepared sample (with the highest PtOx content due to its extensive oxidation at 375°C for 24 h), in contrast, shows a dominant peak at ~1.7 Å (phase uncorrected) due to Pt-O nearest-neighbor scattering. The spectrum of the pre-oxidized catalyst (O_2 treatment at 240°C for 30 min) and those of the catalyst obtained under reaction conditions exhibit features corresponding to both Pt-Pt and oxidic Pt-O scattering [designated as Pt-O(1) in Figure. 4.5], as well as a third feature at an intermediate scattering distance (~2.1 Å phase uncorrected) designated as Pt-O(2).

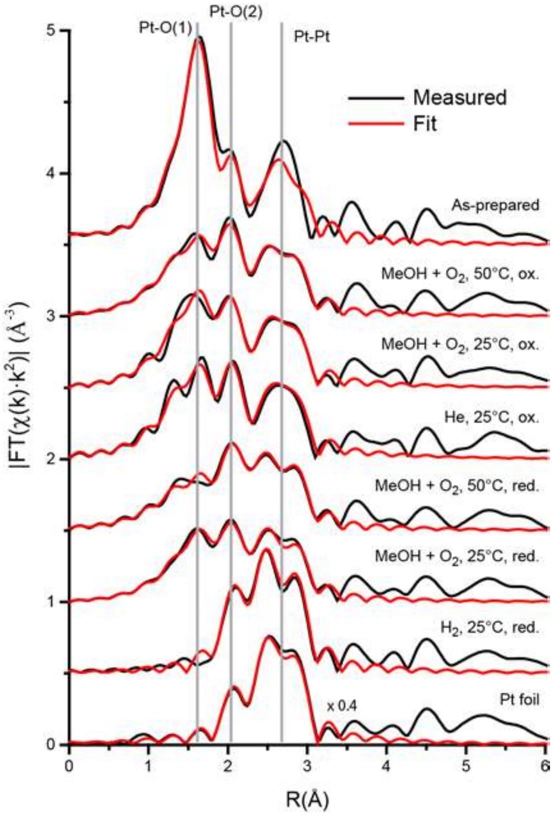

Figure 4. 5. Fourier-transformed k^2-weighted EXAFS spectra of the Pt/γ-Al_2O_3 catalyst after reduction, oxidation and under MeOH oxidation reaction conditions following the two pretreatments leading to the oxidation and reduction of the catalysts. Shown also are first-shell fits to the experimental data using a combination of three scattering components, as described in the text. A Hanning window from 2.5 to 13 $Å^{-1}$ with $\Delta k=1$ $Å^{-1}$ was used to compute the Fourier transforms. The data are vertically displaced for clarity.

To separate and quantify the overlapping components of the EXAFS spectra, least-squares fitting was carried out using theoretically-calculated scattering amplitudes and phase shifts generated using FEFF. The best-fits obtained in this way are plotted together with the experimental data in Figure. 4. 5. The combination of a Pt-Pt scattering component and two Pt-O scattering components was found to adequately reproduce the experimental spectra, as suggested by the observations above. An example of one of the fits, corresponding to the initially-reduced catalyst under methanol oxidation reaction conditions at 25°C, is shown in Figure. 4. 6, with the contributions of the individual scattering components plotted separately in both r-space (Fourier-transformed) and k-space. From these fits, the following distances (phase-corrected) were obtained: Pt-Pt (2.76 Å), Pt-O(1) (2.0 Å), and Pt-O(2) (2.5 Å).

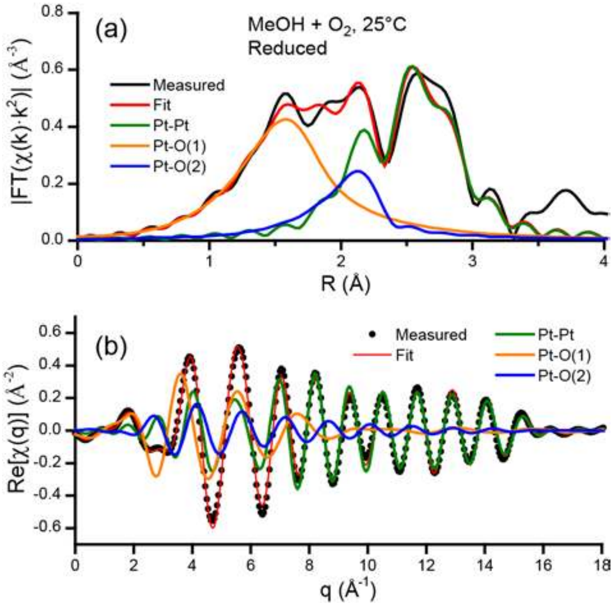

Figure 4. 6. (a) Fourier –transformed (k=2.5-15.5 Å^{-1}) EXAFS spectrum of the initially-reduced catalyst measured at 25°C in MeOH+O$_2$. The fitted spectrum as well as the magnitudes of the three contributing scattering components corresponding to metallic Pt, a Pt-O(1) bond at ~2.0 Å, and Pt-O(2) at ~2.5 Å are also shown. (b) Inverse-Fourier-transformed (R=1.2-3.2 Å) EXAFS spectrum corresponding to that in (a).

Best fit parameters from the analysis of the EXAFS data are given in Table 1 and the Pt-Pt, Pt-O(1) and Pt-O(2) coordination numbers (CNs) are plotted in Figure. 4. 7. The fitted Pt-Pt CN for the reduced catalyst of ~7 corresponds to particles of ~1 nm in diameter,[75, 76] which agrees well with the mean particle diameter *d* measured by STEM, provided that the volume-averaging nature of the XAFS measurement is accounted for by weighting the histogram by d^3. Although the particles measured by STEM had a mean diameter of 0.7 nm, the greater contribution of larger particles results in an apparent diameter (volume-weighted) of 0.9 nm. The Pt-O(1) scattering component of the EXAFS spectra, with a bond length of 2.0 Å, is typical of strong platinum-oxygen bonds, and its appearance upon exposure of the reduced catalyst to the reaction mixture and after oxidation treatments, concomitant with a decrease in the Pt-Pt coordination number, indicates that we do not have chemisorbed oxygen on Pt, but the formation of platinum oxides. Consistent with the XANES measurements, more extensive oxidation is observed following the oxygen pre-treatment at 240°C than during exposure of the reduced catalyst to methanol and oxygen at 25°C, and little change in the oxidation state is observed after exposure of the oxidized catalyst to the reactant mixture. Determination of the extent of oxidation and of the stoichiometric ratio of the oxides formed is not straightforward. Since both the XANES and EXAFS spectra give averaged information for the entire sample, it is difficult to distinguish between a mixture of phases and a single phase of intermediate stoichiometry. The persistent presence of a metallic Pt-Pt EXAFS component following oxidative treatments appears to indicate only partial oxidation of the NPs, yielding a structure with an oxide shell around a metallic core. Nevertheless, we cannot rule out potential contributions from large grains of Pt in the sample which could be only partially oxidized, while the smaller NPs might be completely oxidized. Although not detected in STEM measurements of this sample, even an extremely small number of grains of only modest diameter (10-20 nm) can potentially make a detectable contribution to the XAFS spectra owing to their much greater volume.[58] We note, however, that due to the very low surface-to-volume ratio of such large grains, their contribution to the catalytic activity should in any case be negligible.

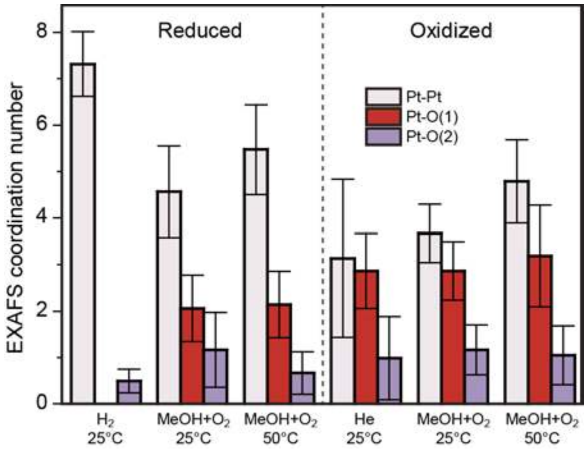

Figure 4. 7. Coordination numbers of three different Pt species extracted from first-shell analysis of EXAFS spectra. The sample was exposed to two different pre-treatments under reductive (left) and oxidative (right) conditions. Spectra were acquired under the conditions indicated, in order from left to right.

The Pt-O(2) scattering component, modeled as a platinum-oxygen bond with a length of ~2.5 Å, could not be quantified with great accuracy due to its strong overlap with the Pt-Pt and Pt-O(1) components, but exclusion of this component led to significantly poorer fits to the EXAFS spectra. The need to include a long Pt-O component in EXAFS spectra of noble metals on various supports has been noted in several previous studies.[58, 77-79] Koningsberger and Gates observed such a component in spectra of various catalysts, and assigned it to bonds between platinum atoms and oxide ions of the Al_2O_3 support, with the unusual length attributed to the presence of hydrogen at the interface.[47, 77] A theoretical study investigating hydrogenated platinum clusters on γ-Al_2O_3 appears to support this, showing also drastic NP shape changes and breakage of Pt-substrate bonds upon adsorption of high coverages of hydrogen at the NP/support interface.[80] However, we consistently observe this long-bond component more prominently under oxidizing conditions than in the exclusive presence of hydrogen. We interpret its consistent presence under oxidizing conditions as a sign of significant contact area between the NPs and the Al_2O_3 support surface, possibly due to a modification of the NP shape (flattening) under reaction conditions. The latter is in agreement with data from Markusse et al.[47] on C-supported NPs which suggested spherical to hemispherical (or flattened) shape transformations when reducing environments were replaced by oxidizing reaction conditions.

In agreement with the XANES measurements, which showed a decrease in WL intensity upon raising the reactor temperature to 50°C, we observe an increase in the Pt-Pt coordination number in EXAFS spectra of both the initially-reduced and initially-oxidized catalysts, as would be expected upon either partial reduction of Pt oxides to Pt metal or upon changing the NP shape from a 2D to 3D morphology. Such a transformation would also be expected to lead to a decrease in Pt-O(1) and Pt-O(2) coordination numbers, which is not clearly observed, although the latter changes may be within the uncertainty of the measurements.

4.4. Discussion

Our experiments reveal that Pt NP/γ-Al_2O_3 catalysts exhibit a complex behavior in the oxidation of methanol which is substantially different from that of bulk Pt. Over pure Pt wire catalysts, McCabe and McCready[81] found that methanol oxidation exhibited similar reaction kinetics to CO oxidation, which is characterized by CO-saturated surfaces and low activity at low temperatures, versus oxygen-saturated surfaces and high activity at high temperature. It was therefore proposed that methanol oxidation over Pt proceeds through a strongly-bound intermediate such as CO, which prevents adsorption of O_2 and thus limits the rate at low temperature. This is similar to what has been observed for electrochemical methanol oxidation over Pt/C catalysts, where poisoning of the Pt anode surfaces with CO has been directly observed and found to cause large overpotentials in the reaction.[44] However, such poisoning does not seem to occur in our experiments, since according to Safonova et al.,[82] a significant shift and broadening to higher energy of the Pt-L_3 white line is expected upon adsorption of CO, which was not observed in our data. In our experiments, XANES measurements indicate that under reaction conditions at 25°C, the platinum catalyst is in an oxygen-rich state qualitatively similar to that of the pre-oxidized sample, regardless of the pretreatment.

In addition, the observation of methyl formate as the main partial oxidation product is consistent with a different mechanism for MeOH oxidation over highly dispersed Pt NPs/Al_2O_3 as compared to pure Pt.[83, 84] In particular, over pure Pt catalysts the main partial oxidation product was formaldehyde, and was only formed in small yields.[81, 85] For Pd/Al_2O_3 catalysts, methyl formate has been observed to be the only product over PdO surfaces[86]. Methyl formate production could occur through different reaction paths involving surface formate species (HCHO).[86] Our high selectivity toward CO_2 at moderate temperatures suggests that the oxidation of formate species is faster than the condensations of absorbed methoxide with HCHO, dimerization of HCHO, or esterification of formic acid (HCOOH) intermediates. [86]

Furthermore, the oxidation state effect seems to be even complex, and system dependent. For example, in methanol oxidation reactions over high surface area palladium catalysts (Pd/Al_2O_3), the reverse trend to what we observed was reported, with a higher catalytic activity[86, 87] (up to 40 times) and a lower selectivity toward methyl formate[86] being detected for the reduced Pd catalysts as compared to PdO. Moreover, the methanol oxidation turnover frequency was shown to be significantly lower for smaller Pd NPs[86] due to stronger binding of chemisorbed oxygen resulting in higher O coverages and the blockage of active sites.[88] A similar size-dependent binding was also reported for the O-Pt system,[5, 89] but no poisoning due to chemisorbed oxygen was observed in our study since both the initially reduced and initially oxidized samples were found to become/remain oxidized in the presence of the reactants (evident from the decrease in Pt-Pt coordination number and increase in Pt-O), and the sample with the highest content of oxygen (pre-oxidized) was also found to be the most active.

Nevertheless, although XANES and EXAFS measurements indicate that in both cases the samples are oxidized under reaction conditions, our experiments show clearly that the initial oxidation state of the Pt NPs has a strong effect on the catalysts' low-temperature reactivity, and that a greater degree of oxidation leads to larger reaction rates. The results of the EXAFS analysis displayed in Figure. 4. 7 reveal a higher degree of oxidation (larger contribution of the Pt-O(1) bond) for the pre-oxidized NPs under reactant exposure at 25°C and 50°C. The latter finding is in accord with previous results by Markusse et al.[47] revealing more extensive catalyst oxidation under aqueous alcohol oxidation reaction conditions after an oxidative catalyst start-up versus a reductive start-up.

It should be mentioned that in our case the pre-oxidized catalyst cannot be considered a true oxygen reservoir, since the amount of oxygen stored in the form of Pt oxide is insignificant as compared to the oxygen consumed during the reaction. Therefore, if any constituents of the catalysts' lattice (in this case oxygen) leave the NP surface as part of the reaction products, they should be subsequently replenished by the oxygen reactant in the gas stream following a Mars-van-Krevelen process.[90] On the other hand, a Langmuir–Hinshelwood (L-H) mechanism in which the reactants both adsorb on the NP surface and then react has also been observed, mainly on reduced metal surfaces,[91, 92] but also on some metal oxide surfaces (e.g. RuO_2)[93, 94]. Furthermore, in numerous previous studies the drastic differences in reactivity observed for oxidized versus reduced catalyst have been attributed to the onset of one of the former distinct reaction mechanisms. For instance, in CO oxidation reactions over Pd catalysts it has been shown that the Langmuir–Hinshelwood mechanism takes place over reduced Pd surfaces, but with a lower activity as compared to oxidized surfaces following Mars-van-Krevelen (MvK) processes.[91, 95] Similar behavior has also been reported for Pt, showing higher activity for the oxidized catalyst during CO oxidation.[49, 50, 96] Nevertheless, the NP/support interface and oxygen or hydroxyl exchange between the metal NP phase and the oxide support might also need to be considered.[97, 98]

In our case, the difference in reactivity between the pre-oxidized and pre-reduced catalysts cannot be attributed to a distinct reaction mechanism taking place over reduced versus oxidized Pt surfaces (e.g. MvK vs. LH), since our *operando* spectroscopic characterization (XANES and EXAFS) revealed that both catalysts are oxidized under reaction conditions. In contrast, our *operando* data indicate that the catalytic activity of the NPs is influenced not only by the presence of oxide overlayers, but also by their precise structure, chemical composition, and possibly also thickness, which likely differ due to the difference in temperature during the initial oxygen exposure (240°C in the case of the pre-oxidized catalyst, 25°C in the case of the pre-reduced catalyst). This is in line with previous studies showing that the catalytic activities of different PtO_x phases vary substantially. For example, theoretical calculations by Seriani et al.[99] showed that while PtO and PtO_2 layers on Pt surfaces are inert towards CO and CH_4 oxidation, a Pt_3O_4 surface can be highly active for these reactions. Other studies have shown that Pt oxides with higher oxidation states such as PtO_2 or $Pt(OH)_3$ could act as poisonous species for primary alcohol oxidation (e.g. methanol), while lower oxidation states such as PtO and Pt(OH) were identified as active species.[100] Unfortunately, EXAFS cannot be used to distinguish the different PtOx phases, since they are all characterized by a nearly identical Pt-O distance of ~2 Å.

The differences in the XANES peak intensity and position observed between the as-prepared NPs (PtO_2-rich) and those measured under reaction conditions [Figure. 4. 4(a)] can serve as guidance to distinguish different chemical states of Pt in PtOx compounds. In particular, the XANES spectra of our catalyst under reaction conditions and after the oxidative pretreatment exhibit white lines which are significantly less intense than that of the as-prepared sample, measured following a 24-h calcination at 375°C. The drastic difference in intensity, despite substantial Pt oxide formation under reaction conditions at 25°C and in oxygen at 240°C, is an indication that the oxides formed under these conditions consist primarily of Pt in a 2+ oxidation state, while the prolonged higher-temperature treatment (375°C) likely produces Pt in the 4+ oxidation state. Such self-limiting oxidation of Pt NPs at low temperatures (and also at low potentials under electrochemical conditions[72]) has been observed in a number of studies to date. Considering that the thermodynamically favored, well-ordered PtO_2 phase has been found to be catalytically inert for a number of reactions, the existence of partially oxidized species (e.g. PtO) appears to be an important element in the high oxidation activities observed for certain catalytic reactions.[55]

Furthermore, XANES data acquired at 50°C on the pre-reduced sample (Figure. 4. 4b) revealed a significant decrease in the WL intensity, not observed on the pre-oxidized sample, which might be either assigned to a more facile reduction of PtOx species, or to the loss of chemisorbed oxygen species. Since no significant changes are observed in the Pt-Pt and Pt-O(1) EXAFS components upon heating the sample to 50°C, a removal of chemisorbed species (which should have a weaker overall effect on the EXAFS coordination numbers) appears more likely. Nevertheless, it should be noted that the measured catalytic activity of such sample is still lower than that of the pre-oxidized counterpart.

Recent theoretical and experimental studies of methanol oxidation over Pd catalysts assigned the most active Pd species to either metallic Pd or a thick and well-ordered PdO structure, with catalysts containing only one layer of oxide having higher reaction barriers and lower reactivity.[101] According to our *operando* spectroscopic data, it is plausible that a better-ordered oxide layer (likely PtO) might be present in the pre-oxidized sample, while a thinner surface oxide layer might exist under reactant exposure on the reduced sample. This might be responsible for the initially higher activity observed for our oxidized sample as compared to the reduced sample.

In summary, our study highlights the importance of the specific chemical structure (Pt coordination environment and degree of disorder) and thickness of the oxidic species formed on NPs after different sample pre-treatments as well as directly under *operando* reaction conditions for oxidative catalytic reactions.

4.5. Conclusions

We have investigated the chemical state of micelle-synthesized Pt NPs supported on γ-Al_2O_3 under methanol oxidation reaction conditions. Reactivity measurements following oxidative and reductive pretreatments show clear differences at low temperature, with an enhanced reactivity of the oxygen pre-treated NPs. The most highly active NPs are shown by XANES and EXAFS measurements to consist predominantly of platinum oxides. Similar measurements of the pre-reduced catalyst show that metallic NPs are also partially oxidized upon exposure to the reactants at room temperature, but with a different structure than those formed in the oxidative pretreatment at 240°C, which makes them less active and less stable. Our study supports the notion that platinum oxides enhance the activity of oxidation catalysts at low temperature, but reveals some subtleties regarding the precise nature of the oxides formed which are key for the understanding of the reactivity trends observed. In particular, our work illustrates the importance of *operando* studies in order to gain fundamental insight into structure, chemical state and reactivity correlations of nanoscale catalysts.

CHAPTER 5: SHAPE-SELECTION OF THERMODYNAMICALLY STABILIZED COLLOIDAL Pd AND Pt NANOPARTICLES CONTROLLED VIA SUPPORT EFFECTS

5.1. Introduction

Oxide supported metal NPs have long been used in chemical sensing and heterogonous catalysis applications.[102-104] The catalytic performance of such systems is affected by a number of parameters, including their size, shape, chemical state, and support. This study focuses on gaining insight into NP/support interactions, which directly influence the final structure and stability of the supported NPs.[105-109] Some of the aspects that need to be considered include the roughness of the support, oxidation state, and NP/support lattice mismatch.[35, 107, 110-115]

A variety of ensemble-averaging[113, 116-123] as well as local spatially-resolved[105, 108, 109, 112, 123-130] experimental techniques have been used to explore the interaction of NPs with supports and the resulting NP morphology. In particular, scanning tunneling microscopy (STM) has been employed to solve the structure of NPs synthesized via physical vapor deposition (PVD) [123, 131, 132] for systems such as Pd NPs/Al_2O_3/NiAl(110)[127], Fe NPs/MgO(100)[133], Au NPs/HOPG[134], Ni[128], Co[135], Ag[135], Pd[105], Cu[136], and Ir NPs/$SrTiO_3$(100) (STO)[137]. Fewer studies are however available describing the shape of thermodynamically stable NPs, such as those prepared via colloidal chemistry methods and subsequently subjected to high temperature annealing treatments. [35]

Experimentally resolving the structure of thermodynamically stable faceted NPs provides the opportunity of analyzing their shape using the Wulff-Kaischew theorem.[105, 127] Following this model, information on important physical parameters affecting the properties of the NPs such as the surface energy anisotropy and the NP-support adhesion energy[11, 31-33] can be extracted.

Nevertheless, not all faceted NP systems can be analyzed following the above theorem, but only those that have been exposed to post-preparation thermal treatments providing sufficient energy to allow the NPs to adopt their thermodynamically-favored structure. For instance, NPs deposited by PVD at high temperature tend to form large flat islands, a geometry mainly driven by NP growth kinetics rather than by a thermodynamic energy minimization. The present work investigates the thermodynamically stable shapes of colloidal Pd and Pt NPs synthesized by inverse micelle encapsulation.

In addition to the role of the NP size on the stabilization of certain NP shapes,[35] strong metal support interactions (SMSI) [111, 122, 138, 139] leading to perturbations in the electronic properties of NPs,[111] or their complete encapsulation by ultrathin support coatings,[111, 122, 139] are expected to influence the surface energy, and consequently the NP structure. Moreover, the NP/support lattice mismatch could be the driving force for the alteration of the NP morphology as compared to the most thermodynamically stable shape of a similarly-sized but unsupported cluster.[133] Nevertheless, only in certain cases, where the NP interfacial facet has the same 2D crystalline lattice structure than the support, the definition of lattice mismatch becomes straightforward.

This work presents a STM investigation of the thermodynamically stable shapes of micelle-synthesized Pd and Pt NPs supported on $TiO_2(110)$. A new computational method to study the effect of interfacial mismatch in the case of NP/support systems of dissimilar lattice structure is introduced. Based on the latter approach, the shape selection observed via STM for Pd NPs on $TiO_2(110)$ is explained by considering the best overlap between the interfacial Pd and TiO_2 lattices. While for the Pt NPs shape-selection was only obtained within a certain NP size range, the vast majority of the Pd NPs supported on TiO_2 were found to adopt an octahedron shape, regardless of their size. Our study highlights that a combination of colloidal chemistry approaches and the selection of an advantageous NP support can be used to obtain thermodynamically stable NP shapes over a broad range of NP sizes.

5.2. Experimental methods

Size selected Pd NPs were prepared using inverse micelle encapsulation.[140] Pd(II) acetate was dissolved in a poly(styrene-b-2vinyl pyridine) [PS(48500)-P2VP(70000)] micellar solution by stirring for two days. A palladium/P2VP molecular ratio of 0.2 was used. The NP size was determined by the molecular weight of the diblock copolymer P2VP head as well as by the Pd/P2VP ratio. The length of the polymer PS group determined the interparticle spacing. A monolayer of uniformly spaced size-controlled metal NPs was obtained by dip-coating a $TiO_2(110)$ substrate into the micellar solution. The Pt NPs were synthesized using an identical procedure but with a H_2PtCl_6 metal precursor. In this case, a PS(27700)-P2VP(4300) polymer with a metal/P2VP ratio of 0.6 was used.

Prior to the *ex situ* NP deposition, the $TiO_2(110)$ substrate was cleaned in ultrahigh vacuum (UHV) by cycles of Ar^+ sputtering (1keV and 10^{-6} mbar) and annealing at 1000°C. An O_2-plasma treatment (15 min at 0.4 bar) was used to remove the encapsulating ligands. Subsequently, the Pd samples were stepwise annealed in UHV in 100°C intervals for 20 min from 300°C to 900°C, one of the samples was annealed for 300 min at 900°C and the second sample annealed for 10 min in 50°C intervals from 900°C to 1100°C and 20 min at 1100°C. The same thermal treatment as the second sample was conducted on the Pt sample. The above thermal treatment was required to allow the NPs to reach their thermodynamically favored shape. In addition, it served to partially reduce the TiO_2 substrate (which was exposed to air and O_2-plasma treatments) and to increase its conductivity for the STM measurements.

The characterization of the initial sample morphology was done via atomic force microscopy (AFM) using a Veeco multimode microscope (Digital Instruments, Nanoscope IIIa) operated in tapping mode. All STM images were acquired at room temperature using an Aarhus 150 HT STM microscope (SPECS GmbH) with tunneling current of I_t =0.1 nA and U_s =1.25 V sample bias. An electrochemically-etched tungsten tip was used for the STM measurements. Before each STM session, the tip was cleaned *in situ* via Ar^+ sputtering (3keV and 10^{-5} mbar).

5.3. Results and Discussion

5.3.1. NP morphology

Figure 5. 1(a) displays an AFM image of the as-prepared micellar Pd NP supported on SiO_2/Si(111). An STM image of the Pd NPs supported on TiO_2(110) acquired at 25°C after ligand removal and annealing at 900°C for 300 min is displayed in Figure. 5. 1(b). A (2×1) reconstruction of the TiO_2(110) substrate is evident in Figure. 5.1(b) based on the atomic row spacing of ~13 Å. Despite the *ex situ* NP synthesis and initial O_2-plasma treatment resulting in a destruction of the ordered TiO_2 surface upon NP deposition and ligand removal, the micellar Pd NPs were found preferentially at step edges of TiO_2(110) after annealing in UHV. The latter might be due to the mobility of the NPs and their preferential stabilization at step edge sites, as well as to their ability to stabilize certain TiO_2 step edges, in particular, TiO_2(110)-[$1\bar{1}0$].[141]

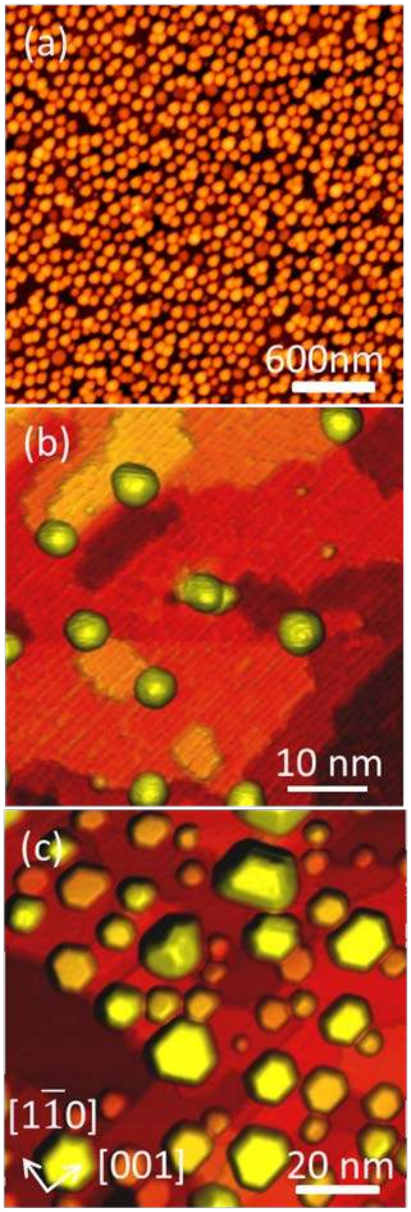

Figure 5. 1. (a) 3×3 µm AFM image and (b) 50×50 nm STM image of micellar Pd NPs supported on SiO2/Si(111) and TiO2(110), respectively, acquired at 25°C. The image in (a) corresponds to the as-prepared NPs before ligand removal and that in (b) was acquired after polymer removal and subsequent annealing at 900°C for 5 hours. (c) 100×100 nm STM image of Pd NPs acquired at 25°C after polymer removal and annealing in UHV at 1100°C for 20 min.

Additional sample annealing at 1100°C for 20 min, Figure. 5.1(c), lead to a widening of the initially narrow NP size distribution due to NP coarsening. Moreover, NP faceting (re-shaping) and the formation of NP shapes with 3-fold symmetry is observed after annealing at this temperature. The majority of the NPs were found to have a (111) facet at the interface with the TiO_2 support. This finding is in agreement with observations made for PVD-grown Pd NPs on graphite and Al_2O_3.[109, 127, 132, 142] At 1100°C, all Pd NPs appear with their edges parallel to the TiO_2(110)-[001] direction, which is a direct indication of an epitaxial relation between Pd(111) and the TiO_2(110) surface.[122]

In order to rule out the encapsulation, Pd-Ti alloy formation, and the loss of Pd during the annealing treatment, (XPS) measurements were acquired. XPS spectra of the (a) O-1s, (b) Ti-2p and (c) Pd-3d core level regions of a Pd NP/TiO_2(110) sample acquired after two different treatments are shown in Figure 5. 2. The O-1s peak was observed at 529.6 eV. The Ti-2p region was fitted by two doublets corresponding to Ti^{3+} ($2p_{3/2}$, 457.2 eV) and Ti^{4+} ($2p_{3/2}$, 458.3 eV).48-50 The formation of Ti^{3+} species was observed as a result of oxygen vacancies enhancement after thermal treatment. The Pd-3d region was fitted by three doublets corresponding to Pd metallic ($3d_{5/2}$, 335 eV), Pd^{2+} ($3d_{5/2}$, 337.1 eV), and Pd^{4+} ($3d_{5/2}$, 339.6 eV). Moreover, after annealing at 1100 °C, only metallic Pd was detected on our samples, ruling out the formation of Pd-Ti alloys after our pre-treatment in atomic oxygen and subsequent annealing in UHV. Also, no loss of Pd was detected via XPS, which is in agreement with the NP volume (Pd coverage) calculations extracted from our STM data up to our maximum annealing temperature.

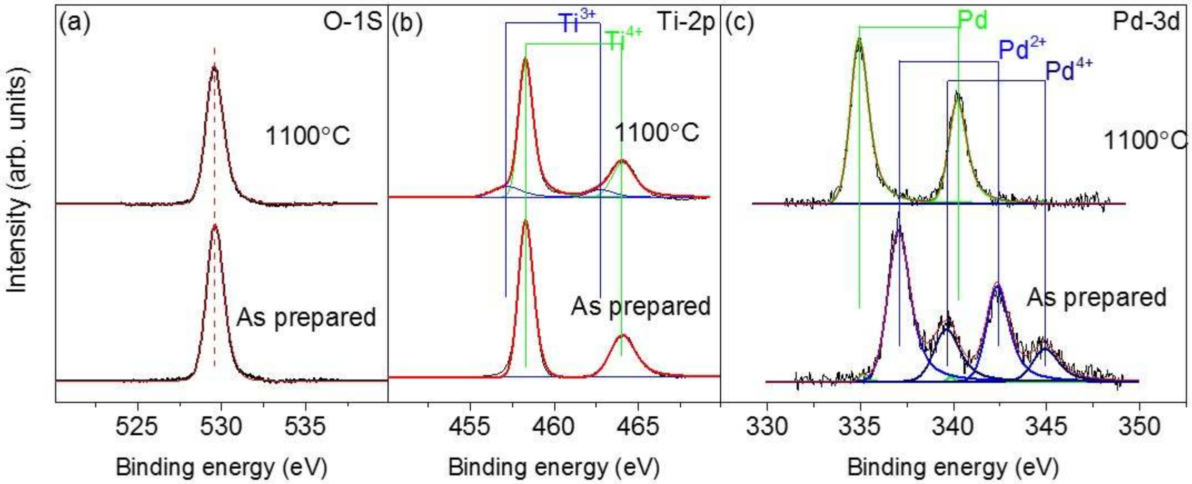

Figure 5. 2. XPS spectra from the (a) O-1s, (b) Ti-2p and (c) Pd-3d core level regions of Pd/TiO_2 (110) sample acquired at 25°C as prepared and after annealing in UHV at 1100 °C.

It is known that tip convolution effects could result in a serious overestimation of a NP's lateral dimension, and volume. However, since the highest points of the NPs are not affected by artifacts from the STM tip apex, they can be used to reconstruct the exact shape of the NP and to reliably obtain additional geometrical parameters such as the area of each facet, the NP volume, the total number of atoms in the NP, as well as the area of the NP-support interface. Here, similar facet orientations [e.g. (111), $(11\bar{1})$, $(1\bar{1}1)$, etc.] are considered to have the same surface energy (γ). Figure 5. 3(d-f) shows the model shapes reconstructed based on the STM data in Figure 5. 3(a-c). Nearly all Pd NPs resolved in this study have a truncated octahedron shape with a (111) interfacial facet (87 out of 90 NPs), similar to those shown in Figure 5. 3(a-c). All the Pd NPs observed in this study have two edges parallel to the TiO_2 rows, which is an indication of theirepitaxial relation with the support.

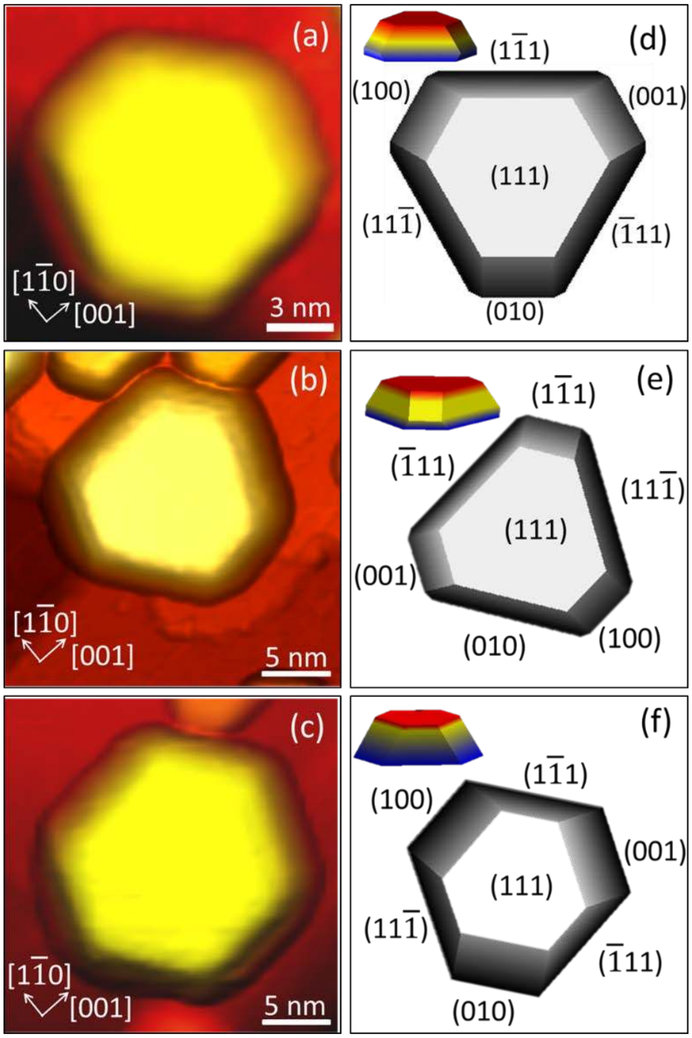

Figure 5. 3. STM images of Pd NPs supported on $TiO_2(110)$ acquired at 25°C after annealing at 1100°C for 20 min (a-c). Tunneling current $I_t = 0.1$ nA and sample bias $U_s = 1.25$ V. Schematic models of the NPs (side and top views) shown in (d-f) are reconstructed based on STM images on the left.

The few NPs observed with atypical shape are featured in Figure 5. 4. Figure 5. 4 displays the only three palladium NPs observed among 90 Pd NP shapes resolved on $TiO_2(110)$ with atypical shape. In figure 5. 4(a), the top facet was found to be tilted by 20° about the $TiO_2(110)$-$[1,-1,\sqrt{2/3}]$ axis, indicating that the interfacial facet is (211). The model shape as well as the cross section profile and facet directions are depicted in figure 5. 4(d). A 16° tilted top facet about the TiO_2 (110)-[001] axis is observed for the NP shown in figure 5. 4(b), with an (122) interfacial facet. The corresponding cross section profile and model shape are included in figure 5. 4(e). The last atypical shape has (100) top and bottom facets. The corresponding model shape with assigned facet orientations is shown in figure 5. 4(f).

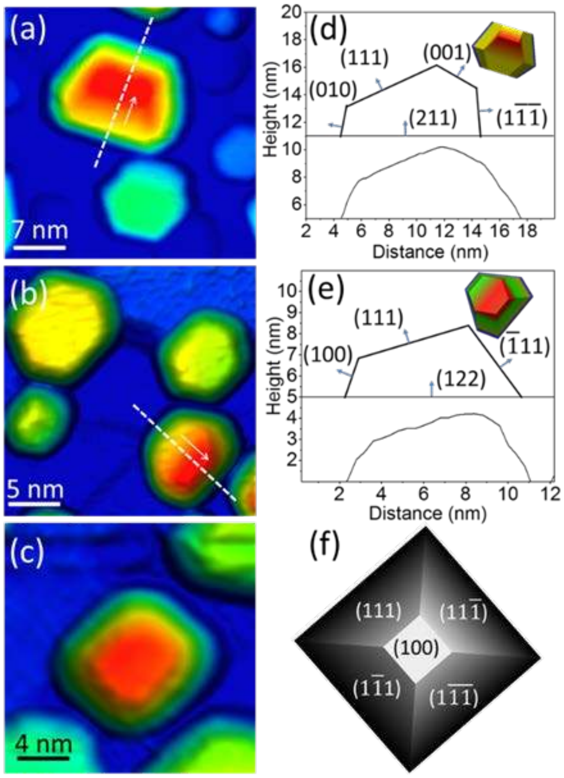

Figure 5. 4. STM images of tilted micellar Pd NPs acquired at 25°C after annealing at 1100°C with (a) (211) interfacial facet and (b) (122) interfacial facet. There corresponding line profiles and model shapes are depicted in (d,e). (c) NP with (100) interfacial and top facets.

Our findings for colloidal Pd NPs are in clear contrast with those obtained for Pt NPs also supported on TiO_2(110), which were found to appear in three different shape categories after similar treatments[35], as shown in Figure 5. 5. The interfacial facets of the Pt NPs are Pt(111) in Figure. 5.5(a), Pt(100) in Figure. 5.5(b), and Pt(110) in Figure. 5.5(c). The fact that for similarly synthesized Pt NPs three different interfacial orientations are observed, while mainly one for the Pd NPs is somewhat surprising, since all NP types were found to have an epitaxial relationship with the TiO_2 support. Moreover, the small difference in the lattice parameter of both systems (Pt: 3.92 Å, Pd: 3.89 Å) makes it difficult to explain such distinct behavior based on lattice mismatch with TiO_2((a= 2.96 Å in [001] and b=6.5 Å in $[1\bar{1}0]$ directions, $\gamma=90^o$ lattice parameters). Since the initial shape of the synthesized micellar NPs is spherical, there is no doubt that the final faceted shapes observed by STM are the result of energy minimization. However, it seems that the higher melting temperature of Pt as compared to Pd (1768°C for Pt vs. 1555 °C for Pd) as well as the shorter annealing times in the case of the Pt NP study plays an important role. In other words, it appears to be more difficult for Pt NPs to achieve the global energy minimum, and the higher melting point may only allow the NPs to achieve metastable morphologies associated with local energy minima, while for the Pd NPs such energy minimization may be achieved within the temperature and time range of the present experiments.

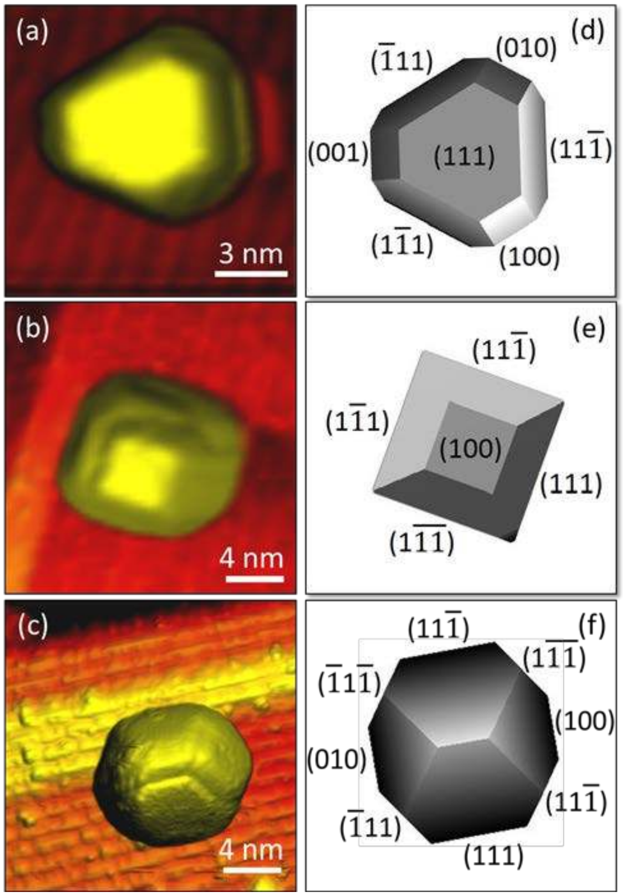

Figure 5. 5 STM images of Pt NPs acquired at 25°C after annealing at 1100°C for 20 min with (a) (111), (b) (100) and (c) (110) interfacial facets. Schematics of the NP shapes are also shown in (d-f).

5.3.2. Epitaxial relationship

In general it is not straight forward to define the epitaxial relationship between the metal NPs and the oxide support when the two surfaces have entirely different structures. For instance, in this study the $TiO_2(110)$ surface has a rectangular lattice (a= 2.96 Å in [001] and b=6.5 Å in $[1\bar{1}0]$ directions, γ=90º), while the Pt(111) and Pd(111) surfaces, which are the most common interfacial facets obtained here, have equilateral triangular lattice (a=b=2.77 Å for Pt and 2.75 Å for Pd,

γ=60º). However, in spite of the entirely different surface lattices, the epitaxial relationship between the Pt and Pd NPs and the TiO_2 support is clearly evident in our experimental data from the perfect alignment of the NP edges or symmetry axes with TiO_2 atomic rows.

Here, we introduce a new approach to study the mismatch effect in cases of dissimilar lattice structure as is the case for our Pt and Pd NPs on TiO_2(110). A MATLAB code was written to construct 2D atomic models of the NP interfacial facet and the TiO_2(110) support. By distorting the metal lattice in all possible ways, the best configuration to accommodate the support lattice could be determined. The overall NP-support binding energy is defined based on the energy of Pt-Ti or Pd-Ti bonds following Lennard-Jones atomic interaction. Different Pd and Pt surface orientations were considered, including, (111), (110), (100), (211) and (221). The interfacial metal surface was modified by changing its in-plane rotation angle (θ), the expansion/compression of the metal lattice in the TiO_2[001] and TiO_2[$1\bar{1}0$] directions (ε_x, ε_y, respectively), a metal lattice shift in x and y directions, as well as the distance between the metal and TiO_2 surfaces (h). It is worth mentioning that the rutile structure has the highest stability among all TiO_2 phases and therefore no TiO_2 phase transformation is expected to occur. In addition, the relaxation of TiO_2 interfacial atoms in presence of the NPs was neglected.[143, 144]

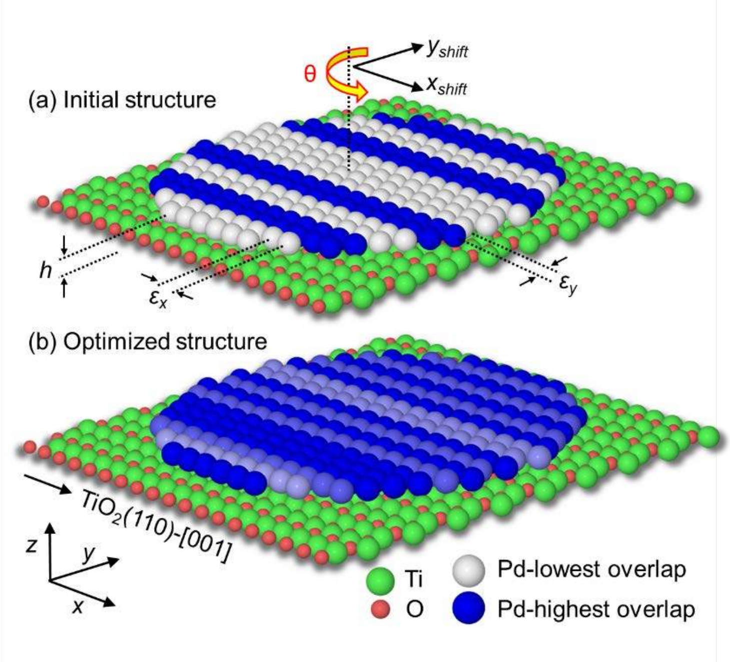

Figure 5. 6. Schematic of the (111) Pd interfacial facet on the TiO_2 substrate: (a) initial structure and (b) structure obtained after maximizing the adhesion between the Pd(111) and TiO_2(110) atomic lattices via the contraction/expansion of the Pd lattice and other optimizations. The Pd atoms with lighter color are those having weaker bonds with the underlying TiO_2 lattice, and vice versa.

Figure 5. 6 displays an example of the Pd(111)/TiO_2(110) interface. In the initial structure depicted in Figure. 5. 6(a), most of the atoms have weak bonds with the substrate lattice (light color). However, after optimizing the Pd lattice structure (expansion/contraction, rotational orientation, etc.) in Figure. 5. 6(b), Pd atoms are observed with a stronger bonds with the substrate (darker color). Figure 5. 7 (panels a and b) shows the changes in the NP/support adhesion as a function of the rotation orientation and shift in X and Y direction for the (111) interfacial facet. For the (111) interfacial facet, the optimum rotational angles of the Pd lattice with respect to TiO_2 (110) were found to be 0°, 60°, 120°, etc., leading to two edges of the Pd NPs being parallel to the TiO_2 (110)-[001] direction. This is in excellent agreement with our STM experimental observation.

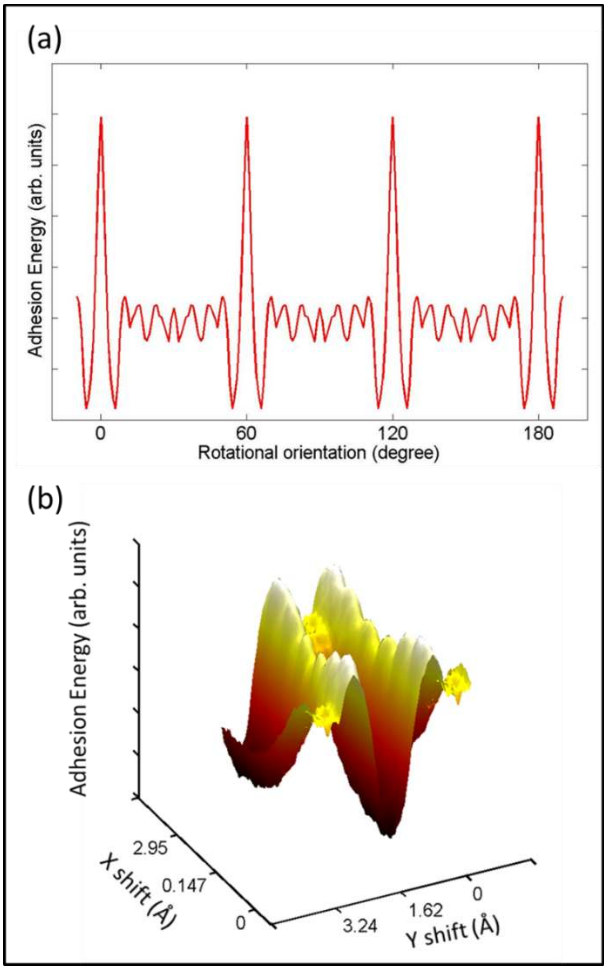

Figure 5. 7. Pd/TiO_2(110) adhesion energy as a function of the (a) rotational orientation and (b) the shift in X and Y directions.

Following the above simple calculations, Figure 5. 8 shows the normalized adhesion energy of Pd NPs with the TiO_2(110) support for different Pd interfacial facets. All the adhesion energies for different Pd facets are normalized by that of the Pd(111)/ TiO_2(110) interface. The highest adhesion energy is observed for the Pd(111) interfacial facet, which was the predominantly observed interface in our experiments belonging to hexagonal top Pd NPs. In addition, for the (111) interfacial facet, the optimum rotation angle of the Pd lattice with respect to TiO_2(110) was found to be 0°, 60°, 120°, etc., leading to two edges of the Pd NPs being parallel to the TiO_2 (110)-[001] direction. This is in excellent agreement with our STM experimental observation.

The same calculation on Pt NPs also resulted in the highest adhesion energy for the (111) interfacial facet, which confirms that the interaction with the support alone cannot be the reason behind the different shapes obtained for the Pt NPs. Instead, considering the higher melting temperature of Pt as compared to Pd (1768 °C vs. 1555 °C) it is likely that the maximum annealing temperature used in our experiments was not high enough to allow the Pt NPs to reach their most stable shapes, but only one of the closest structures having a local energy minimum.

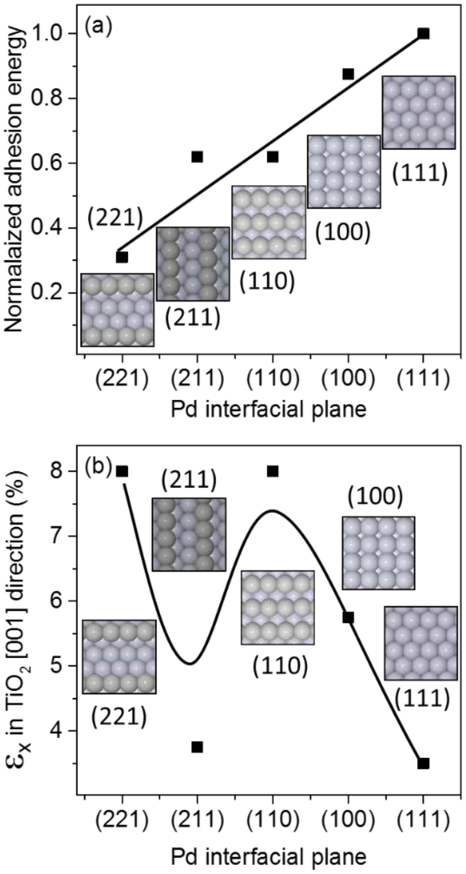

Figure 5. 8. (a) Normalized Pd/TiO_2(110) adhesion energy and (b) contraction/expansion of the Pd lattice for different Pd interfacial planes. The solid lines are only guides for the eye.

5.4. Conclusion

We have achieved shape-selection for Pd NPs supported on TiO_2(110), irrespective of their size, via the combination of colloidal NP synthesis and a post-preparation thermal treatment, resulting in NP faceting and an epitaxial relationship with the support.

Our study demonstrates that the most thermodynamically stable shape of Pd NPs supported on TiO_2(110) is a truncated octahedron with Pd(111) top and interfacial facets, which could be achieved by annealing the micelle-synthesized Pd NPs at 1100°C and subsequent cooling to 25°C. Furthermore, the alignment of the NP edges with the TiO_2 (110)-[001] direction was observed, and considered as evidence for the achievement of an epitaxial relation with the support for the *ex situ* prepared NPs. Moreover, the epitaxial orientation and the preferred Pd(111) interfacial facet was explained based on the maximization of its adhesion with the TiO_2 (110) lattice. By comparing similarly synthesized colloidal Pt and Pd NPs, our study reveals the importance of the melting temperature of the metal as well as NP-support interactions in determining the preferred NP shape and orientation.

CHAPTER 6: SIZE-DEPENDENT ADHESION ENERGY OF SHAPE-SELECTED Pd AND Pt NANOPARTICLES

6.1. Introduction

Late transition metal nanoparticles (NPs) supported on oxides are widely used in heterogeneous catalysis applications. One of the factors influencing the catalytic efficiency of NP catalysts is their interaction with the support. The NP support may affect the stability and sintering rate of the NPs, their geometric and electronic structure, as well as their chemical state.[1, 60, 129, 145-151] Furthermore, for metal NP/oxide support systems composed of metals with high surface energy (e.g., Pt, Pd, Ni, Fe) and reducible oxide substrates with low surface energy (e.g., CeO_2, TiO_2, $SrTiO_3$), strong metal/support interactions are expected, which could change the chemical activity of the NPs by modifying their electronic structure or via encapsulation of the active sites within the NP surface by support atoms.[102, 111, 122, 123, 152-157]

Although various spectroscopic and imaging methods have been used to study NP-support interactions, open questions regarding related modifications of the NPs electronic structure, the stability of certain NP shapes on different support materials and support orientations, as well as the size dependency of NP/support interactions still remain.[105, 108, 109, 116-119, 121-130, 154, 158] Since NP-support interactions may affect the morphology of the NPs, an experimental analysis of structurally well-defined supported NPs could be helpful in understanding these interactions. STM can be used to resolve the shape and atomic structure of such NPs, as well as to study NP/support interactions, as demonstrated in multiple examples for oxide-supported metal NPs,[105, 127-129, 133-135, 137, 159-161] including Pt and Pd NPs on TiO_2.[129, 144, 162, 163]

By directly resolving the shape of faceted NPs via STM and by using the Wulff- Kaischew theorem, information on surface energy anisotropy as well as the NP-support adhesion energy can be extracted.[112, 130-132] The adhesion energy of physical vapor deposited (PVD) Pd NPs on Al_2O_3,[127] Ni[128] and Pd[105] on $SrTiO_3$(100), and Pt NPs on Fe_3O_4 (111) single crystals and films[123] has been determined following the former approach. However, in the previous examples, the average aspect ratios of all NPs in a given non-homogeneous sample were considered. Nevertheless, it has also been demonstrated that the strain induced by the lattice mismatch of two dissimilar materials and its relaxation mechanism depend on the NP size,[164, 165] and therefore, a size- and shape-dependent adhesion energy should be considered.

Since the Wulff- Kaischew theorem is built on the assumption that the NP structure has reached its minimum energy, not all faceted NP systems may be analyzed following this theory, but only those systems where the most thermodynamically stable NP shapes were achieved. The latter corresponds to systems where post-preparation thermal treatments were applied, and where thermodynamic energy minimization is guaranteed. This is in contrast with NP shapes that are achieved based on NP growth kinetics, as it is favored in PVD-grown NPs or in other kinetically shape-selective synthesis methods.[166-168]

Furthermore, in many chemical reactions such as the oxidation of styrene, 2-butanol, 2-propanol, and formic acid, as well as the hydrogenation of 2-methyl-3-buten-2-ol, the reactivity and selectivity was found to depend on the structure of the NPs, which could be optimized by having a particular facet orientation on the surface.[2, 12, 13, 169-174] In some of the mentioned studies the NPs were thermodynamically stable,[12, 172] however, most of the up to date shape-controlled NPs have been grown kinetically,[13, 169-171, 175-177] which makes the stability of such catalysts under reaction conditions doubtful.[175, 178] On the other hand, since the NP structure also depends on its interaction with the support, understanding such interaction could be useful in designing a stable NP structure optimized for a particular chemical reaction or reaction pathway.

In this study, the shape of thermodynamically-stable ligand-free colloidal Pt and Pd NPs supported on TiO_2 (110) was resolved by STM, and the Wulff- Kaischew theorem was used to determine NP/support adhesion energies as a function of the NP size. Furthermore, since the relative ratio of different facet orientation areas on the surface was observed to be size- dependent, a new method is suggested to design NPs with desired ratio of exposed facet areas.

6.2. Experimental Methods

The inverse micelle encapsulation method has been used to prepare size-selected Pt and Pd NPs.[1, 60] Chloroplatinic acid (H_2PtCl_6) and Pd(II) acetate ($C_4H_6O_4Pd$) were dissolved in [PS(27700)-P2VP(4300)] and [PS(48500)-P2VP(70000)] micellar solutions, with metal/P2VP molecular ratios of 0.6 and 0.2, respectively. A monolayer of NPs was obtained by dip-coating TiO_2(110) substrates in the metal-loaded micellar solution. Before dip-coating, the TiO_2(110) single crystal was cleaned in ultrahigh vacuum (UHV) via cycles of Ar^+ sputtering (1keV and 10^{-6} mbar) and annealing at 1000°C. An *in situ* oxygen plasma treatment (400 mbar for 15 min) was used to remove the encapsulating ligands and XPS measurements were acquired to confirm complete polymer removal. In order to obtain thermodynamically stable NP shapes as well as to increase the conductivity of the substrate for STM measurements (by increasing the density of oxygen vacancies in TiO_2), the samples were stepwise annealed in UHV in 100°C interval from 300°C to 900°C and in 50°C intervals from 900°C to 1100°C.

The sample morphology (size, shape and substrate dispersion) was resolved via STM. STM images were acquired at room temperature (RT) using an Aarhus 150 HT STM microscope (SPECS GmbH) with an electrochemically-etched tungsten tip. The STM measurements were done *in situ* after the annealing treatments. Before each scanning session, the tip was cleaned in UHV via Ar^+ sputtering (10^{-5} mbar and 3 keV). The tunneling current (I_t) was set to 0.1 nA and the sample bias (U_s) to 1.25 V.

6.3. Results and Discusssion

Figure 6. 1(a) shows an STM image of Pd NPs acquired at 25°C after ligand removal and subsequent annealing in UHV at 900°C for 5 hours. A total Pd coverage of approximately 1 monolayer was estimated from the STM images. The relatively narrow NP height distribution (3.2 ± 0.7 nm) observed after such high temperature treatment reveals the high stability of the NPs against sintering. Further sample annealing at 1100°C for 20 min, Figure. 6. 1(b), leads to the formation of truncated octahedron NPs, with a characteristic hexagonal footprint and (111) interfacial facets. At this temperature, NP sintering and the consequent widening of the NP height distribution is observed (3.9 ± 0.9 nm), but a much wider NP diameter distribution, as can be seen in (b) and the line profiles included in (c). Nevertheless, after the former treatment, the NP shape observed for the majority of the Pd NPs is similar, regardless of their size.

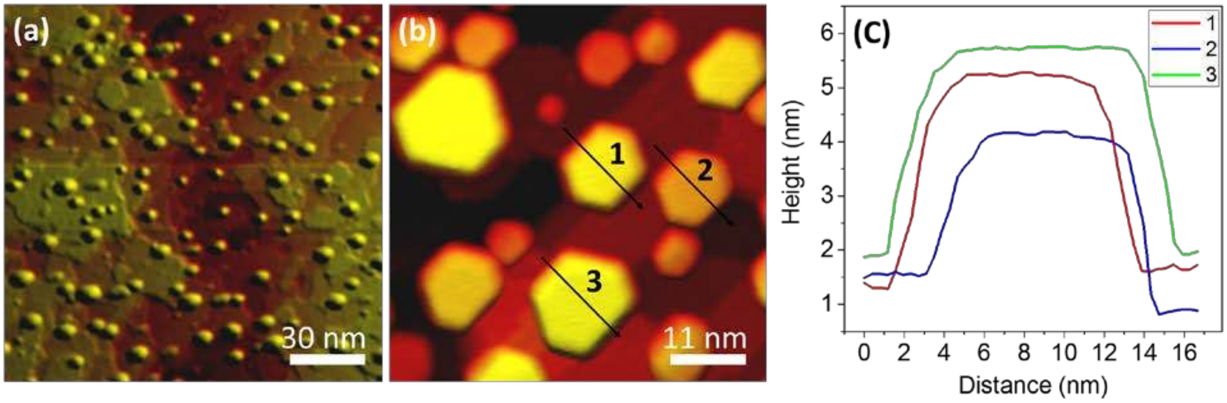

Figure 6. 1(a,b) STM images of micellar Pd NPs supported on TiO_2(110) acquired at 25°C after polymer removal and subsequent *in situ* (UHV) annealing at (a) 900°C for 5 hours, and (b) 1100°C for 20 min. (c) Representative line profiles of the NPs marked in (b).

STM data from similarly prepared Pt NPs acquired at 25°C after annealing at 1100°C are included in Figure. 6. 2. A relatively narrow NP height distribution (2.9 ± 0.6 nm) was observed after such high temperature treatment. NP height histograms of a Pd sample obtained after annealing at 900°C and 1100°C and of a Pt NP sample after annealing at 1100°C are also shown in Figure. 6. 3.

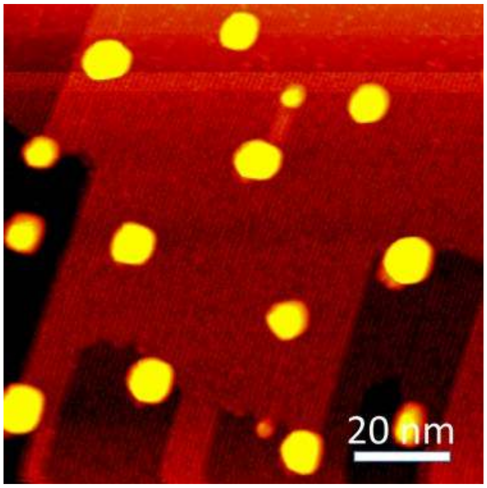

Figure 6. 2. 100×100 nm STM image of micellar Pt NPs supported on TiO_2 (110).

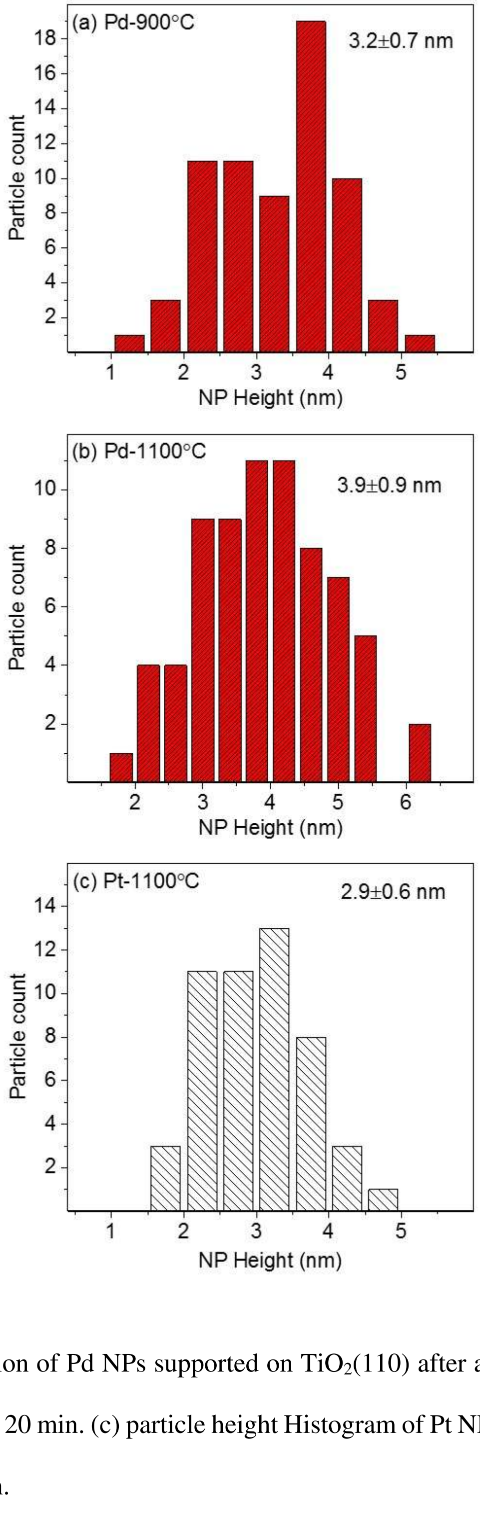

Figure 6. 3. Particle height distribution of Pd NPs supported on $TiO_2(110)$ after annealing at (a) 900°C for 5 hours , and (b) after annealing at 1100°C for 20 min. (c) particle height Histogram of Pt NPs supported on $TiO_2(110)$ acquired after annealing at 1100°C for 20 min.

Figure 6. 4. shows high resolution STM images of individual Pd (a,b) and Pt (e,f) NPs. The lengths of the edges of the top facet and the NP height measured by STM have been used as input in a MATLAB code to obtain the reconstructed model shape. In STM the lateral dimensions of a NP are overestimated due to tip convolution effects, Figure 6.5. For deconvolution of the tip effect, our approach was to determine the NP shape based on the data obtained from the top most point of the NPs, which includes the NP height, and the lengths of the sides of the top facet (L_1 and L_2), Figure 6.4(a). All possible configurations were explored through a MATLAB code, assuming that the NP height equals h_{111}+h_{int} in Figure. 6. 6, and assuming the same surface energy for similar facet orientations [(111),$(1\bar{1}1)$,$(11\bar{1})$,etc.]. Following this method, our analysis lead to a unique NP model that matches the height and the lengths of the top facet of each NP.

Interestingly, all NPs have one edge aligned with the TiO_2(100)-[001] orientation. Although in contrast with the case of Pd, three different shape categories were observed for the Pt NPs, in this study we have used only truncated octahedron Pt shapes for direct comparison with the Pd NPs, which were found to only display the latter mentioned shape.[35]

The Wulff-Kaischew theorem describes the shape of supported NPs, stating that for any facet orientation (klm) at the free surface, the ratio of the surface energy (γ_{klm}) to the distance of that facet from the NP center (h_{klm}) is constant: γ_{klm}/h_{klm}= C, Figure. 6. 6. For our Pt and Pd NPs, the only featured facet orientations are (100) and (111), which have the lowest surface energies. After obtaining the reconstructed model shape for all NPs from STM measurement, the average surface energy ratio $\frac{\gamma_{100}}{\gamma_{111}} = \frac{h_{100}}{h_{111}}$ extracted for all Pd NPs by using the Wulff- Kaischew theorem was 1.12 ± 0.07, which is in good agreement with theoretical results (1.13) by Methfessel et al.[179] The same calculation for the Pt NPs/TiO_2(110)[35] lead to an average $\gamma_{100}/\gamma_{111}$ of 1.2 ± 0.1, which is slightly higher than that of the Pd NPs, but in agreement with the theoretical value of 1.2 described by Iddir et al.[108]

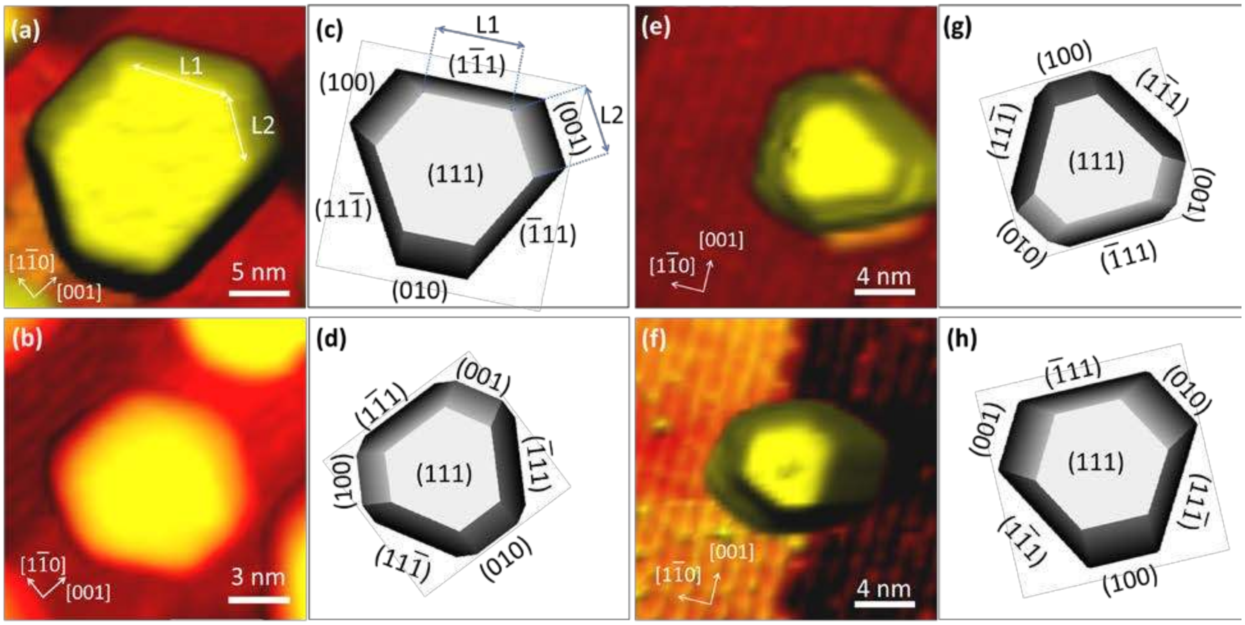

Figure 6. 4. STM images of Pd (a,b) and Pt (e,f) NPs supported on $TiO_2(110)$ acquired *in situ* at 25°C after annealing at 1100°C for 20 min. Schematic models of the Pd (c,d) and Pt NPs (g,h) are also shown (top views).

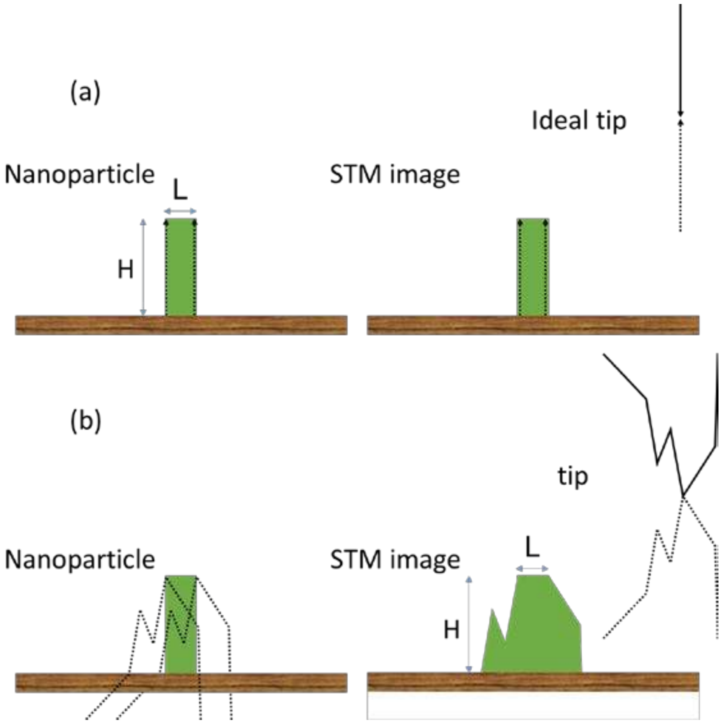

Figure 6. 5. Schematic illustrating tip convolution effects in STM.

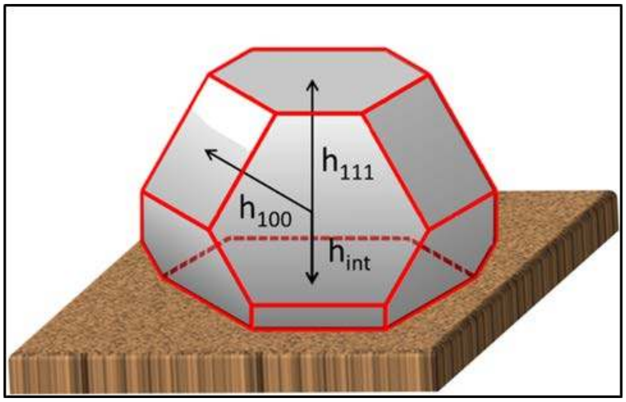

Figure 6. 6. Schematic model of a supported truncated octahedron NP with a (111) facet interfacial plane.

The Pt/TiO_2 and Pd/TiO_2 systems are however known to show strong metal-support interactions (SMSI) that could lead to NP encapsulation by the support,[122, 123, 139] and a modification of the surface energy ratio ($\gamma_{100}/\gamma_{111}$). Nevertheless, due to the good agreement between our measured surface energy ratios and the theoretically predicted values, combined with additional compositional information extracted from XPS measurements (Figure. 6. 7), we can conclude that the possibility of encapsulation is unlikely under our experimental conditions. This might be due to the following reasons: (i) the oxygen plasma pre-treatment conducted on our NPs, leading to NP oxidation, might contribute to the minimization of the encapsulation, at least within the 600°C-850°C temperature range, before PtO_x and PdO_x species on the NPs are fully reduced;[5, 157, 180-184] (ii) the oxidized state of the TiO_2 surface after the O_2-plasma treatment might hinder/slow down the encapsulation. For instance, Fu et al. [111] did not observe encapsulation of Pd NPs on non-reduced TiO_2, while it was evident on a reduced support surface. Because of our oxidative sample pre-treatment before annealing, following Fu's findings, low or no drastic encapsulation is expected and therefore won't be considered in the following discussion.[111]

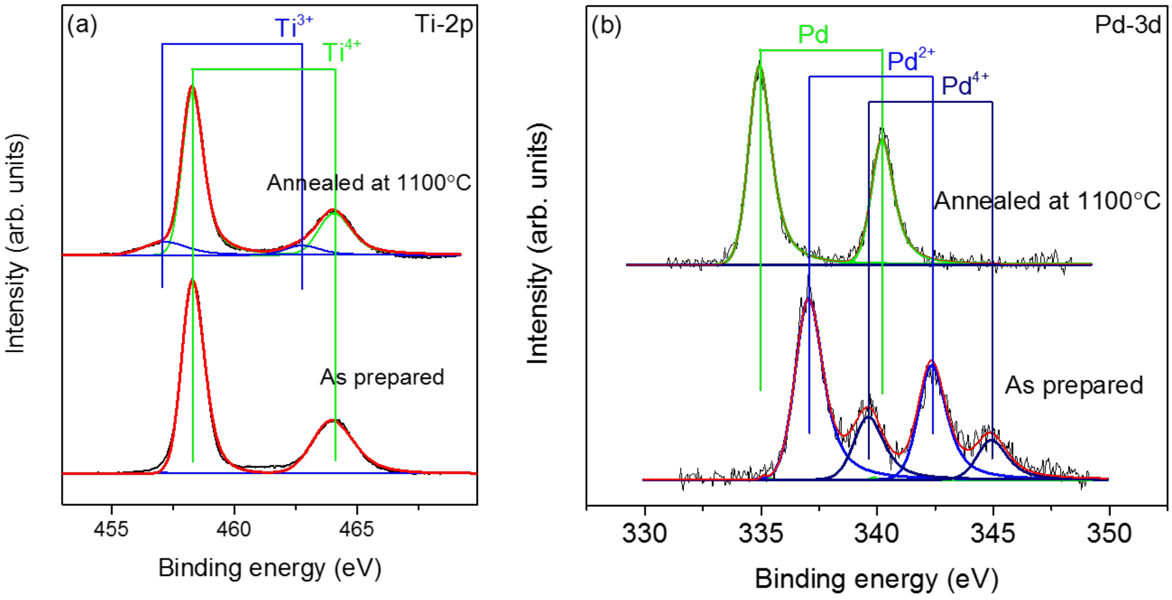

Figure 6. 7. XPS spectra of the (a) Ti-2p and (b) Pd-3d core level region of Pd NP/TiO_2(110) acquired at 25°C on the as-prepared sample (O_2-plasma treated) and the same sample after annealing at 1100°C in UHV. The Ti-2p region has been fitted with two doublets corresponding to Ti^{3+} ($2p_{3/2}$, 457.2 eV) and Ti^{4+} ($2p_{3/2}$, 458.3 eV). The presence of Ti^{3+}

in the sample after the thermal treatment is due to the increase in oxygen vacancies on the surface. The Pd-3d region has been fitted by three doublets corresponding to Pd metallic ($3d_{5/2}$, 335 eV), Pd^{2+} ($3d_{5/2}$, 337 eV) and Pd^{4+} ($3d_{5/2}$, 339.6 eV). After annealing at 1100°C, just metallic Pd has been observed, which rules out the formation of Pd-Ti after annealing in UHV.

6.3.1. NP-support adhesion energy

The Wulff- Kaischew theorem describes the most thermodynamically stable shape for supported NPs:

$$\frac{E_{adh}}{\gamma_{\mathrm{hkl}}} = \frac{h_{hkl} - h_{\mathrm{int}}}{h_{hkl}} \tag{6.1}$$

, where h_{hkl} is the distance of the (*hkl*) top facet, and h_{int} is the distance of the interfacial facet from the center of the NP, Figure. 6. 6.

The adhesion energy, E_{adh}, is defined as the energy per unit area needed to detach the NP from the support. The adhesion energy was calculated for all individual NPs based on their geometry obtained using a MATLAB code and using the theoretical surface energies of γ_{111}(Pd) = 1.64 J/m^2,[179] and γ_{111}(Pt) = 1.58 J/m^2.[108] For our Pt and Pd NPs supported on TiO_2(110), a linear decrease in the adhesion energy was obtained with increasing NP height, Figure. 6. 8(a). A similar trend has been reported for wet-impregnated Pd NPs (2-20 nm) on MgO nanocrystalline powders. To understand this trend we need to have in mind that there are two possibilities for the NP to accommodate the mismatch with the underlying support: (i) exact registry with the support at the interface that results in NP lattice distortion due to mismatch, and (ii) interfacial lattice dislocations. In the former case the lattice distortion propagates and dissipates through the NP bulk but in the latter case the interfacial dislocations might become favorable in spite of their large energy penalty due to the associated decreased lattice strain in upper layers.

To gain additional knowledge on these phenomena we can consider the ratio of elastic energy to dislocation energy. The elastic energy (E_ε) is the energy associated with the elastic strain (ε) induced by the substrate parallel to the NP/support interface. For a NP grown on a mismatched support, equation (2) describes the ratio of the elastic energy, E_ε to the dislocation energy, E_d:

$$\frac{E_\varepsilon}{\mathrm{E_d}} = 4\pi(1+\nu)(1+\frac{G}{G_s})\frac{\int_0^h \varepsilon(z)^2 dz}{b^2[\ln(\frac{R}{b})+1]} \tag{6.2}$$

,where G and G_s are the metal and substrate shear modulus, respectively, h and R are the NP height and lateral size of the NP, b is the Burgers vector, and ν is the Poisson ratio of the metal.[185] In contrast to the case of thin films, the strain in the NP lattice might also be released laterally, and might vary as a function of the distance from the support, *z* (eq. 2).[186]

For small NPs (small h), lattice distortions that propagate throughout the entire NP height have a lower energy than interfacial dislocations.[112, 187] However, since the lattice distortion energy increases with increasing NP size, the E_z/E_d ratio in eq. (2) increases with NP height and therefore, there will be an onset size for which adding lattice dislocations at the NP-support interface would lower the total energy. Since each dislocation lowers the strain in all upper layers, larger NPs would minimize their energy by having a larger number of dislocations at the NP-support interface (e.g. smaller Burgers vector, b). In addition, a larger number of dislocations at the interface translates into a lower adhesion energy with the support. Consequently, a larger NP with a larger number of dislocations is expected to have lower adhesion energy.

Another finding of our study is the fact that Pt NPs have lower adhesion energy than Pd NPs with a similar size, Figure. 6. 8(a). One of the parameters that should be considered in this respect is the metal oxide formation energy.[145, 188] As Campbell and co-workers demonstrated,[145] the oxide formation energy reflects the strength of the bond that a metal atom can make to oxygen on the support, which in many cases correlates to the NP-support adhesion energy. However, in our study, the higher oxide formation energy of Pt as compared to Pd suggests a higher adhesion energy for Pt, in contrast to our experimental observations.

However, from eq. (2), the prefactor $(1+G/G_s)$ shows that as the NP shear modulus G increases, the E_ε/E_d ratio also increases. Such higher energy cost for lattice distortion as compared to lattice dislocation favors the formation of the dislocation at the interface, and also leads to a larger number of dislocations and consequently lower adhesion energy for similarly sized NPs. The higher shear modulus of Pt (61 GPa) as compared to Pd (44 GPa) leads to a higher number of dislocations. The latter explains the lower adhesion energy of Pt NPs as compared to Pd NPs. Therefore, it appears that in our case the lattice misfit, and not the oxide formation energy, is the dominant factor affecting the adhesion of the NPs to the support.

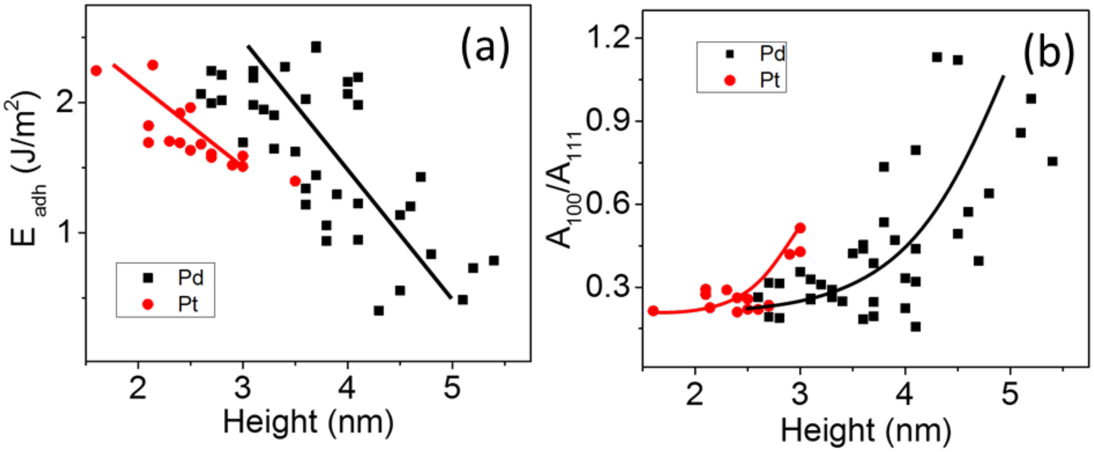

Figure 6. 8. (a) NP-support adhesion energy as a function of the NP height obtained from the Wulff- Kaischew theorem based on STM data. The insets in (a) display the shapes of the NPs experimentally observed. (b) Ratio of (100) to (111) facet areas for Pd and Pt NPs extracted from STM data. The black and red lines are guides for the eye.

It is worth mentioning that the experimental data reported previously,[145, 189, 190] are not in contrast with our data, since they compared much smaller Pt NPs (1-5 nm) with bigger Pd NPs (10-15 nm) supported on MgO. As discussed earlier, since a lower adhesion energy is expected for bigger NPs, large Pd NPs may in fact show lower adhesion energy as compared to Pt NPs. In addition, considering the distinct mismatch values and the chemical composition of different supports, a direct comparison cannot be made for NPs deposited on different supports.[189, 190]

Figure 6. 8(b) displays the ratio of the facet areas (A_{100}/A_{111}) and its increase with increasing NP height. This behavior could be understood by noticing Figure. 6. 8(a) inset, illustrating that NPs with smaller heights are flatter as a result of a higher adhesion energy and therefore, they are characterized by smaller (100) side facets[102] and a smaller A_{100}/A_{111} surface ratio as compared to larger 3D NPs. This observation provides us with the ability to design NPs with a particular facet area ratio by adjusting their size, which is desirable for the optimization of structure sensitive catalytic processes.[13, 170] At the same time, control might also be achieved on the relative content

of perimeter atoms at the NP/support interface, which is another key parameter affecting catalytic reactions since such atoms are in a number of cases the most chemically active sites.[191-194]

6.4. Conclusion

The present study provides insight into key parameters that need to be considered in the design of stable nanoscale catalysts with higher tolerance against sintering and structure change, namely, the combination of NP support and NP size.

Nanoparticle-support interactions were investigated using shape-controlled thermodynamically stable Pd and Pt NPs prepared via inverse micelle encapsulation and supported on TiO_2 (110) as model systems. The adhesion energy of the NPs to the support was obtained by using reconstructed models of the NPs extracted from STM data. The importance of the NP size in determining the NP-support adhesion energy and thermal stability of the NPs was highlighted. In particular, for Pd (2.5-5 nm) and Pt (1.5-3.5 nm) NPs, the NP/support adhesion energy was found to decrease with increasing NP height, which was explained by a larger number of dislocations at the interface for the larger NPs.

Differences were observed between the Pt and Pd NP systems, namely, for a given NP shape, Pt NPs displayed lower adhesion energy than Pd NPs, which was attributed to the higher elastic energy of Pt leading to a lower transition size from the lattice distortion to the interface dislocation regimes with increasing NP size.

Overall, our study features a path for tuning the NP morphology by taking advantage of the size dependency of NP-support interactions.

CHAPTER 7: SHAPE-SELECTED BIMETALLIC NANOPARTICLE ELECTROCATALYSTS: EVOLUTION OF THEIR ATOMIC-SCALE STRUCTURE, CHEMICAL COMPOSITION, AND ELECTROCHEMICAL REACTIVITY UNDER VARIOUS CHEMICAL ENVIRONMENTS

7.1. Introduction

Metal alloy particles of nanometer dimensions typically show different surface catalytic reactivity as compared to their bulk alloy form. Since the surface-to-volume ratio increases with decreasing nanoparticle (NP) size, characteristics such as the surface atomic composition and geometrical distribution, alongside with their imperfections (defects), become increasingly relevant at controlling the catalytic behavior of individual metal NPs. This is the origin of size- and shape-dependent reactivities of metal NP catalysts[195-198]. While the exploration of NP size effects in catalysis has a long history[199-204], our understanding of the role of the NP shape in heterogeneous catalysis and electrocatalysis is still in its infancy[12, 205-212]. New wet-chemical colloidal synthesis methods have significantly improved our ability to control the size and shape of metal and oxide NPs[20, 211, 213, 214].

Other than the particles' geometry, the surface atomic composition of alloy NPs largely affects their catalytic behavior. Although the surface composition is initially determined by molecular processes taking place during the NP synthesis, it is a dynamic parameter. In fact, the surface composition of small NPs is highly sensitive to external stimuli, such as temperature or surface active components in gas- or liquid-phase environments during heterogeneous catalytic and electrocatalytic processes, respectively. In gas-phase thermal catalysis as well as electrochemical catalysis, surface adsorption and reaction can induce surface restructuring[214, 215] or selective surface segregation of an alloy component[216-226] Owing to the presence of the segregated component, partially segregated surfaces may display bifunctional catalytic enhancement effects resulting in a new and unexpected catalytic behavior compared to the original surface. Along these lines, the catalytic activity of bimetallic surfaces could be turned on and off by suitable consecutive exposure to segregation-inducing environments.

Several previous experimental and theoretical studies have investigated temperature-[227-236] and adsorbate-driven [237-240] segregation process in Pt-Ni systems, including the effect of such segregation in their catalytic reactivity[227, 229, 241-243]. In general, segregation phenomena in bimetallic systems can be understood based on the surface energies and atomic radius of the two metals, with the element having a larger atomic radius and a lower surface energy segregating towards the free surface. In the case of platinum and nickel, although platinum has a slightly higher surface energy than Ni (2.475 J/m^2 vs. 2.45 J/m^2)[244], due to the much larger atomic radius of Pt (1.39 Å) as compared to Ni (1.24 Å), the segregation of platinum toward the surface is expected, as it was reported for annealing studies in vacuum[227-239] and in H_2 environments[239]. However, for this material system there is experimental[229, 230, 239, 245] and theoretical[227, 232, 234, 239, 242] evidence that Pt segregation would only result in the formation of the so called “Pt skin” or “sandwich structure”, and not in a phase-separated core-shell structure. The Pt skin refers to a configuration in which the outermost layer is Pt-rich, while the second layer is Ni- rich. Remarkably, although adsorbates could change the segregation properties of the Pt-Ni system, the segregation phenomena appear to be limited to the top-most surface layers. For example, while some calculations did not predict any segregation due to chemisorbed oxygen[240], others showed the formation of a Ni skin with the outermost layer enriched by Ni and the second layer by Pt.[239] In contrast, in cases where oxides might be readily formed, this behavior might be drastically modified, since oxygen might then not only be present at the surface or top-most subsurface region, but also in the bulk of the NPs. In particular, the formation of nickel oxide could contribute to the segregation of Ni to the NP surface, as discussed for various nickel alloys.[237]

In this contribution we investigate the evolution of the structure, composition, and catalytic reactivity of shape-selected octahedral Pt-Ni bimetallic NPs in response to various thermal, gas-phase, and electrochemical environments. We follow the changes of the near-surface composition of the PtNi(111) facets after exposure to oxygen and hydrogen gas environments using XPS and contrast those to surface compositional transformations during electrochemical potential cycling pretreatments in alkaline and acidic environments. Acidic electrochemical environments dissolve Ni species from the surface leaving behind a Pt enriched interface. Oxygen and hydroxide (alkaline) environments promote the surface segregation of Ni(II) oxide species, which, owing to their oxophilicity and resulting affinity to water activation, show a significant promotion of the electrochemical CO oxidation and the electrocatalytic hydrogen evolution. A bifunctional synergetic effect between surface Pt atoms adjacent to Ni oxide domains is proposed.

7.2. Experimental

7.2.1. Catalyst synthesis

Commercial Vulcan XC 72R supported Pt NPs with a 15 % loading by weight with a BET value of 151 m^2/g and mean size of about 5 nm was used as benchmark and standard catalyst[246-248] for CO electrooxidation and hydrogen evolution. The catalyst was employed as received from the group of Prof. Strasser at the Technical University Of Berlin.

The same group synthesized the same group of spherical PtNi NPs. For this purpose 0.3 mmol of $Ni(ac)_2/4H_2O$, 0.4 mmol of 1,2-tetradecandiol, 0.6 mL of oleic acid, and 0.6 mL of oleylamine were added into 40 mL of dioctylether in a three-neck flask. The solution temperature was then increased to 200 °C in an oil bath during 40 min. Subsequently, 0.3 mmol $Pt(acac)_2$ dissolved in 2 mL dichlorobenzene was injected into the reaction flask via a syringe. This solution was held at 200 °C for 1 h and then cooled down to room temperature (RT). After that, ethanol was added to precipitate the NPs, which were then collected after centrifugation (8000 rpm, 10 min). The NPs were further washed in ethanol and then redispersed in hexane. The latter solution was then mixed with Vulcan XC carbon by a ultrasonic treatment. To remove the residual surfactants, the obtained catalysts were heated at 180 °C in air for 1 h and further annealed at 400 °C in H_2 (4 vol% in Ar) for 4 h. [See Ref. [249] for further details]

To synthesize octahedral PtNi NPs, 4 mM $Pt(acac)_2$ and 10 mM $Ni(acac)_2$ were mixed together in 100 mL DMF under ultrasonic treatment. The resulting homogeneous solution was transferred to a glass-lined stainless-steel autoclave and heated from RT to 120ºC within 10 min. The temperature was held during 42 h. Before washing the particles, the carbon support was added to the solution under ultrasonic treatment. Finally, the oct-PtNi/C was washed with ethanol/water several times. [See Ref. [249] for further details]

For the XPS study, three identical PtNi samples containing octahedral NPs were prepared in the TU Berlin using the same NP solution. The NPs were drop-coated on atomically clean pyrolytic graphite (HOPG) substrates after sonicating the original NP solution for 10 minutes and subsequently annealed in O_2, H_2 and vacuum.

A catalyst ink was prepared at the TU Berlin by mixing the as-prepared catalyst powder in 5 ml of an aqueous and Isopropanol solution containing 5 wt% Nafion and ultrasonicated for 15 min. A 10 µl aliquot was dispensed onto the rotating disk electrode (RDE) resulting in a Pt loading of about 7µg/cm^2 for s-PtNi/C, 8 µg/cm^2 for oct-PtNi/C, and 9 µg/cm^2 for Pt/C, respectively. Finally, the as-prepared RDE catalyst film was dried at 50 ^{o}C for 15 min.

7.2.2. Catalyst characterization

Transmission electron microscopy (TEM) and energy dispersive X-ray spectroscopy (EDX) measurements and electron energy loss spectrometry (EELS) experiment were performed at the TU Berlin. For the EELS line profile measurements, both Ni-$L_{2,3}$ and Pt-$M_{4,5}$ edges spectra were collected across individual NPs. The relative intensities of the Ni-$L_{2,3}$ and Pt-$M_{4,5}$ edges were normalized with respect to their elemental scattering cross sections so that the intensity ratio can be related to the atomic ratio along the electron beam.

The morphology and dispersion of the PtNi NPs supported on HOPG was monitored via AFM. On these samples, thermal treatments in different environments were conducted in a high pressure (HP) cell (SPECS GmbH) that allows annealing up to 800°C and pressures up to 20 bar. The HP cell was evacuated after each thermal treatment and the samples were directly transferred to the attached UHV system without exposure to air. XPS data were acquired *in situ* in a UHV chamber equipped with a monochromatic x-ray source (Al-kα, 1486.6 eV, 350 W) and an hemispherical electron analyzer (Phoibos 100, SPECS GmbH). For the XPS study, three identical PtNi samples containing octahedral NPs were annealed in 1 bar O_2, 1 bar H_2, and vacuum environments within the HP cell for 20 min. The temperature ramp was set to 1°C/sec. All XPS spectra were measured at RT. The high resolution XPS data were acquired using a pass energy, E_{pass}, of 18 eV. The XPS spectra were analyzed using the CASA XPS software.[250] All spectra were aligned using the C-1s peak from the graphite support at 284.3 eV as reference. The Ni/Pt atomic ratios were obtained from the area under the Ni-2p and Pt-4f peaks after normalization by the corresponding atomic sensitivity factors of 26.08 and 14.99, respectively.[250]

All electrochemical measurements were carried by the collaborator group of the TU Berlin in a conventional three electrode cell, employing a Pt gauze as counter electrode and a commercial reversible hydrogen electrode (RHE). All potentials here are referenced to this reference electrode. Pt/C, s-PtNi/C and oct-PtNi/C catalysts were cycled between 0.06 and 0.6 V_{RHE} at 100mV/s in deaereated 0.1 M KOH alkaline or 0.1 M $HClO_4$ acidic solutions. Catalysts that underwent 1 and 20 cycles in alkaline are denoted as “1-alkaline” and “20-alkaline”, respectively. s-PtNi/C and oct-PtNi/C catalysts that were cycled 100 times in 0.1 M $HClO_4$ under otherwise identical conditions were denoted “100-acid”, see Ref [249].

The electrochemically pretreated Pt/C, s-PtNi/C and oct-PtNi/C catalysts were also tested for their electrooxidation (stripping) of adsorbed CO at saturation coverage [249].

After the electrochemical pretreatments at the TU Berlin, the RDE was transferred into an electrochemical cell containing a H_2-saturated 0.1 M KOH (pH 13) solution. In each experiment, the electrode was immersed in the solution at +0.05 V. Then, the HER polarization curves were recorded between -0.2 V and +0.05 V versus RHE at the scan rate of 1mV/s. The HER activities were normalized to the catalytically active real surface area (ECSA), which was evaluated by the

CO stripping. All electrochemical measurements discussed here were carried out by our collaborator within Prof. Strasser group at the TU Berlin.

7.3. Results and Discussion

7.3.1. Structural and morphological characterization (TEM, AFM)

As described in the experimental section, octahedral Pt-Ni bimetallic NPs with a bulk Pt:Ni ratio of 1:1 were prepared be the Strasser group (TU Berlin) using wet-chemical methods (solvothermal process at elevated pressures),[251] with DMF serving as solvent, surfactant and reducing agent[20, 252]. The spherical NPs were prepared using an ambient pressure hot-injection technique[253] at 200°C involving a high-boiling point solvent, surfactants and reducing agents as separate components [254].

Figure 7.1 (a,b) shows TEM and HAADF STEM micrographs of as-prepared unsupported octahedral PtNi (oct-PtNi) NPs. The particles exhibited a narrow size distribution with a mean diameter of about 9 nm. EELS data[20] suggested that the main axes, the edges, and vertices of the octahedra are enriched in Pt (see bright contrast corner in Figure. 7. 1(b)), while the facet centers are enriched in Ni, with Ni oxide likely being in the top-most layer. Figure 7.1(c,d) shows TEM HAADF STEM images of the unsupported and carbon-supported spherical PtNi (s-PtNi) NPs. Particle sizes were narrowly distributed around a mean of about 6 nm. EELS intensity line scans for Pt and Ni, Figure. 7. 1(d) acquired for selected individual NPs showed that the catalyst consisted of a single face-centered-cubic bimetallic alloy phase with a fairly homogeneous distribution of Pt and Ni atoms at the atomic scale. Pt to Ni intensity ratios across an individual NP are close to 1, which is consistent with the PtNi bulk composition. The particle center appears to be slightly enriched in Ni, indicating the formation of Ni-rich alloy seeds during the reduction process.

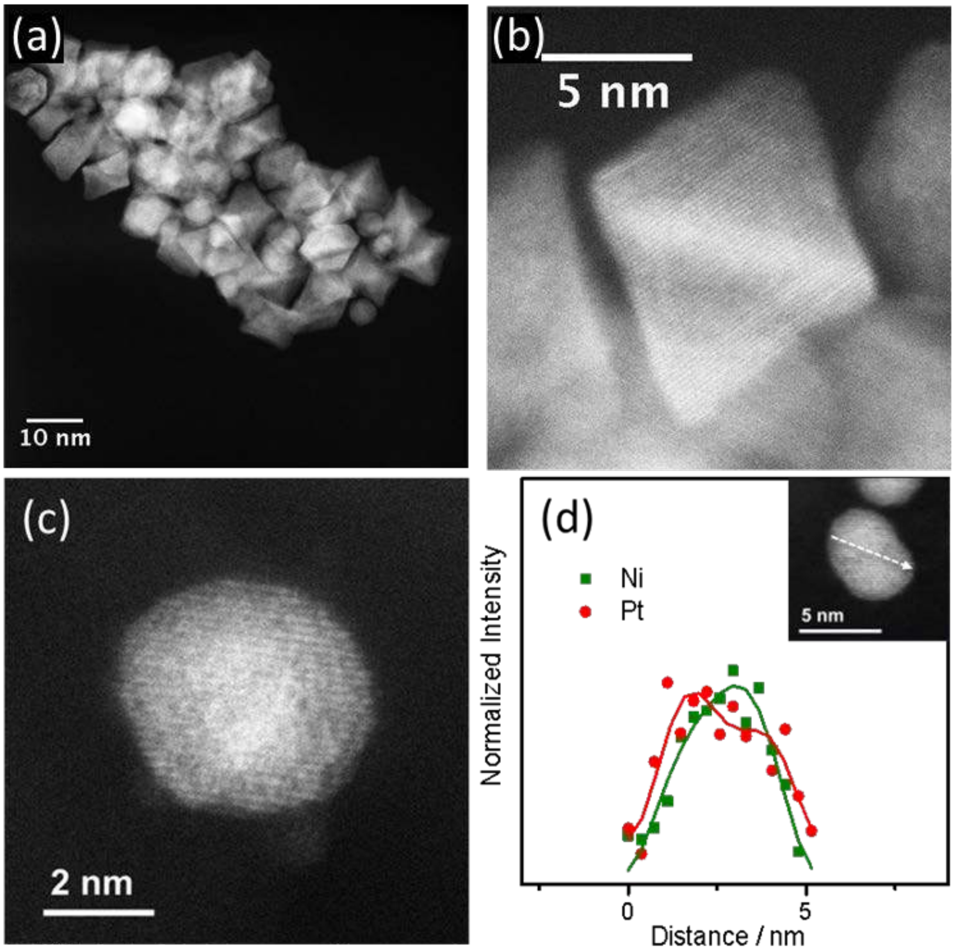

Figure 7. 1. (a) HAADF STEM image of oct-PtNi NPs; (b) HAADF STEM image of a single octahedral PtNi NP(c) HAADF-TEM image of an individual PtNi NP, (d) STEM EELS line scan (along the arrow in the inset) of a single PtNi NP showing the spatial distribution of Ni and Pt.[Images taken from Ref [249]]

Figure 7. 2 shows an AFM image of the as prepared $Pt_{50}Ni_{50}$/HOPG sample. The average NP height obtained is 3.7 ± 0.8 nm. The atomic steps of the HOPG surface can be observed, and NP decoration of step edges is evident.

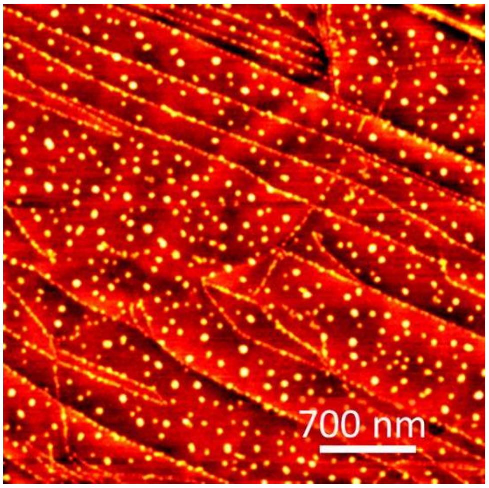

Figure 7. 2. AFM image of an as-prepared PtNi NP sample acquired at RT.

7.3.2. Evolution of surface composition under chemically reactive gas and liquid environments

Gas-phase pretreatments

Figure 7. 3 shows XPS data from the Pt-4f and Ni-2p core level regions of one of the as-prepared samples together with spectra acquired on identical samples after *in situ* thermal treatments at 300°C for 40 minutes in different environments, namely in UHV, in 1 bar of O_2, and in 1 bar of H_2. Higher annealing temperatures were avoided due to concerns regarding possible NP shape transformations. However, Monte Carlo simulations of PtNi NPs annealed in vacuum at 330°C demonstrated no drastic change in the shape of octahedral NPs.[234]

The Pt-4f spectra in Figure. 7. 3(a) were fitted with three doublets ($4f_{7/2}$ and $4f_{5/2}$) corresponding to Pt^0, Pt^{2+} and Pt^{4+} with binding energies in agreement with those previously reported.[5] The Ni-2p core level region was fitted with two doublets corresponding to Ni and Ni^{2+} ($2p_{3/2}$ and $2p_{1/2}$) and third one accounting for satellite peaks.[255, 256]

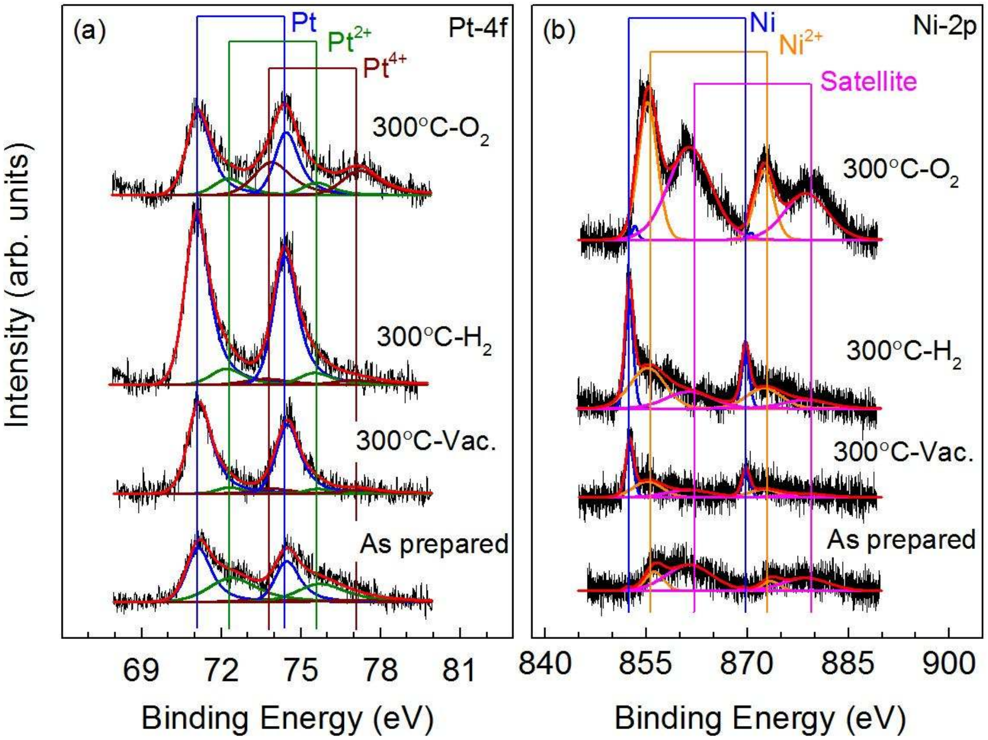

Figure 7. 3. XPS spectra from the (a) Pt-4f and (b) Ni-2p core level regions of PtNi NPs supported on HOPG acquired at RT before (as prepared) and after annealing in vacuum and in 1 bar of O_2 and H_2 at 300˚C for 40 min.

The content of the different Pt and Ni species as well as the Ni/Pt ratio after the different treatments is shown in Figure. 7. 4. The as prepared samples contain metallic and oxidic Pt species (PtO and PtO_2), while the Ni is mainly in the form of NiO. Upon annealing in vacuum or hydrogen, the partial reduction of both PtOx and NiOx species is evident from the increase in the content of the respective metallic components, Figure. 7. 3 and 7. 4. While Pt is completely reduced in H_2 at 300°C, a relatively large NiO content is still observed, as expected due to the higher affinity of nickel for oxygen as compared to platinum. Nevertheless, the most significant effect was observed upon annealing in oxygen, with not only the total oxidation of Ni, but also a drastic increase in the intensity of the Ni signal. On the other hand, for the Pt component, only an increase in the Pt^{4+}

content is detected, with metallic Pt species being still present. These results suggest that under those conditions, a Pt-rich NP core might be protected by a NiO shell.

Figure 7. 4(c) shows the Ni/Pt ratio for the as prepared sample as well as that obtained after annealing in different environments. The Ni/Pt ratio increases in all cases after the thermal treatments, with the $(Ni/Pt)_{O2} > (Ni/Pt)_{Vacuum} > (Ni/Pt)_{H2}$. As it was mentioned in the introduction, the Pt segregation induced by annealing in vacuum or H_2 environments would be hard to detect using XPS since it only affects the composition of the outermost layers of the NPs. The increase observed here is most likely due to initial presence of the oxide. To the best of our knowledge there is no theoretical study predicting the segregation behavior of Pt and Ni in the presence of such oxide species. However, our XPS measurements revealed that as long as the Ni oxide is present in the NPs, a shell of NiO and a core of Pt will form upon heating, regardless of the chemical environment. Interestingly, the final content of Ni at the NP surface appears to be proportional to the extent of the oxidation of the Ni component after a given treatment. This can be seen by comparing the Ni^{2+} contributions in Figure. 7. 4(b) and the Ni/Pt ratios in Figure. 7. 4(c) after the different treatments. For both parameters, the lowest content is observed after the thermal treatment in H_2, followed by the vacuum annealing, and the maximum after O_2 exposure at the same temperature (300˚C).

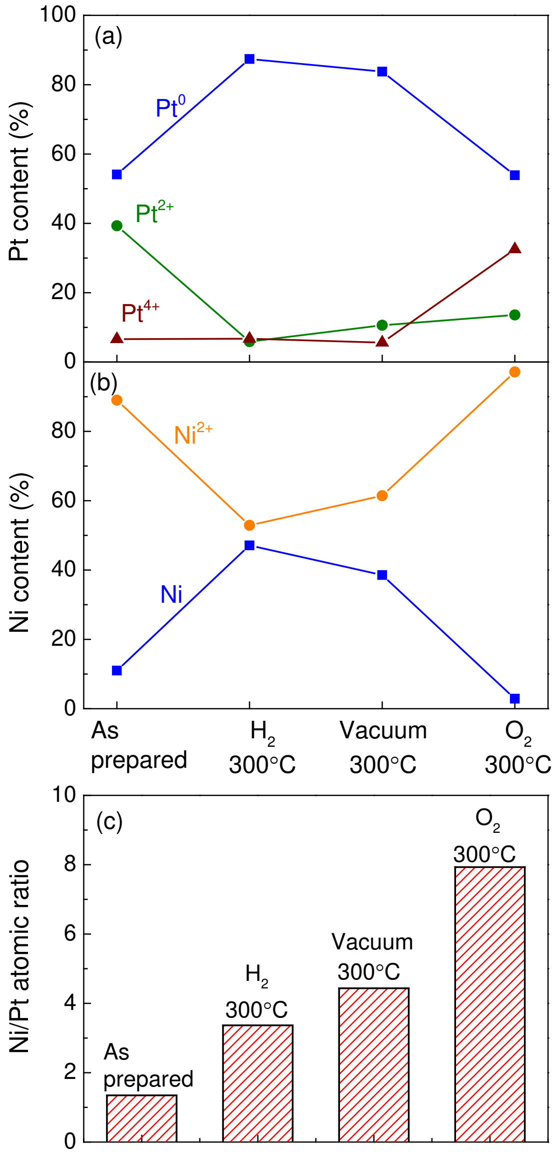

Figure 7. 4. Relative content of (a) Pt and (b) Ni species extracted from the XPS measurements. (c) Ni/Pt atomic ratio obtained for the as prepared sample and analogous fresh samples after the indicated sample treatments.

As was mentioned in the introduction, the formation of nickel oxide could contribute to the segregation of Ni to the NP surface. By reducing the NiO via annealing in vacuum or hydrogen environments, Ni can diffuse back into the Pt core and form a uniform Pt-Ni alloy. The onset temperature for Ni diffusion into Pt(111) single crystals and alloy formation has been experimentally reported to vary between 180°C- 380°C, depending on the Ni coverage (0.8-3ML).[236] Figure 7.5 displays a model of the distribution of Pt, Ni, PtOx and NiOx on the octahedral NPs after the different *in situ* thermal treatments.

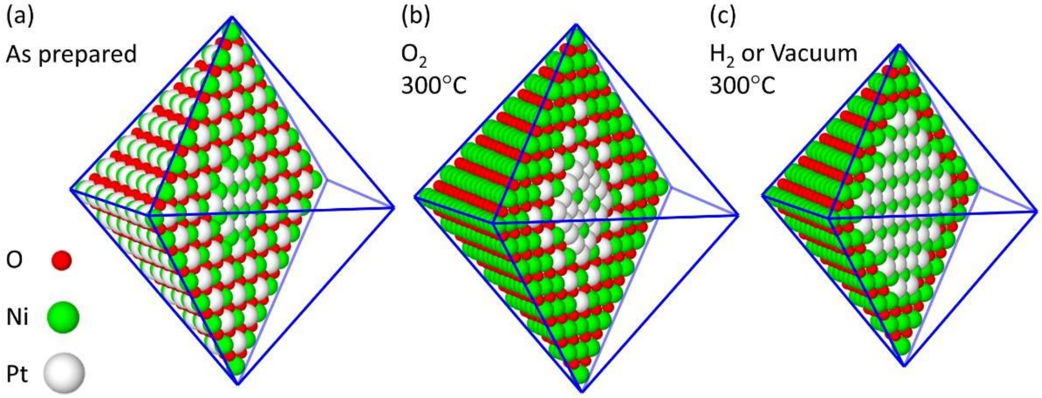

Figure 7. 5. Model describing the segregation phenomena observed via XPS for the octahedral PtNi NPs after annealing at 300˚C in different gaseous environments.

Electrochemical potential cycling pretreatments

Having explored the surface redox and segregation phenomena of oct-PtNi NPs in gas-phase chemical environments, our collaborator, the Strasser group at the TU Berlin performed a similar study in electrochemical environments and tested the effect of the changes in the surface structure and composition on the catalytic reactivity. To achieve that, they subjected samples containing carbon-supported octahedral (oct-PtNi), and spherical (s-PtNi), alloy NPs to three different potential cycling protocols, two in alkaline (0.1 m KOH) and one in acidic (0.1 m $HClO_4$) electrochemical environments. They chose a potential range from +0.05 to +0.6 V/RHE for each cycle such that the evolution of the surface composition would not be influenced by the formation of Pt oxides, while Ni and NiO surface species could form, segregate, or dissolve. The cycling pretreatments included: i) a single cycle in an alkaline solution representing a standard measurement close to the pristine state of the catalyst surface (1-alkaline), ii) 20 potential cycles in an alkaline solution, because this treatment yielded a stable cyclic voltammogram (not shown) and showed a maximum in catalytic HER performance (see below), and iii) 100 potential cycles in an acidic electrolyte, after which the cyclic voltammogram was stable with time and resembles in shape that of a pure Pt surface, indicating the complete loss of Ni or NiO from the top layer.

The effect of the pretreatments in the three electrochemical environments on the morphology and chemical composition of the oct-PtNi NPs was reported in Ref [249].

The TEM data from the TU Berlin evidenced that 20 cycles in the alkaline solution did not have a significant effect on the morphology or Z-contrast, except perhaps a slightly darkened contrast near the bottom vertex of the image. Darkened regions can be explained by reduced specimen thickness or enrichment in the lighter element at comparable thickness. Since the alkaline environment precludes the dissolution of either Pt or Ni, an enrichment in Ni or Ni oxides is a likely explanation. Clearly increased Z-contrast between the bright central octahedral edges and the opposite facets and vertex regions was also observed. Since acidic conditions are known to dissolve Ni and Ni hydroxide surface species, a thinning of the specimen by selective metal dissolution appears as a likely explanation for the changes in the Z-contrast. Also, along the <100> direction, the enhanced Z-contrast between the central octahedral frame and the (111) facet region is consistent with a reduced thickness of the facet region. To support the latter conclusion our collaborators in Berlin performed additional STEM and high resolution TEM studies on acid-leached oct-PtNi.[249] High resolution TEM images confirmed that the acid-cycled octahedra suffered from selective surface dissolution of Ni and Ni hydroxide species near the facet centers, resulting in a concave facet morphology.

In order to gain further insight into the surface and near-surface composition of the electrochemically-treated samples, our collaborator measured the octahedral and spherical PtNi NPs supported on flat adhesive graphite tabs after 1 and 20 cycles in the alkaline solution, and after 100 cycles in the acid solution via *ex situ* XPS. Figure 7. 6 shows Pt-4f and Ni-2p XPS data of oct-PtNi and s-PtNi NPs after the different electrochemical treatments. After one cycle from 0.05 V to 0.6 V and back to 0.05 V in an alkaline electrolyte, platinum is reduced to the metallic state, while Ni is partially oxidized in the s-PtNi NPs and completely oxidized in the oct-PtNi NPs, Figure. 7. 7 (a),(b). The initial Ni/Pt ratios in the electrochemical environment were significantly higher than those under UHV gas-phase conditions, suggesting the formation of a thick Ni-rich surface layer in the liquid environment. Additional potential cycling in the alkaline solution (20 and 100 cycles) lead to a slight decrease in the Ni/Pt ratio, signalizing a Pt-richer surface/near surface NP region, Figure. 7. 7(c). According to their Pourbaix behavior, Ni hydroxides cannot chemically dissolve under pH = 13 conditions. Thus, the Ni/Pt decrease observed either originated from an electrochemical surface segregation of Pt species, or else, from a partial surface Ni hydroxides reduction at the low electrode potential limit (0.05 V) and subsequent Ni inward diffusion and Pt-Ni alloy formation inside the NP core. The appearance of a small Pt^{2+} component in the XPS data of the octahedral NPs might correlate with the facile electrochemical oxidation of low-coordinated surface Pt atoms near the corners and edges of the octahedral NP surface. It should also be noted that these samples were all measured after transfer in air to the UHV XPS system, and therefore, it cannot be ruled out that a fraction of the oxidic Pt and Ni species observed at the NP surface could originate from the air exposure. Nevertheless, as mentioned before, PtOx species were not observed on the 1-alkaline oct-PtNi NP sample. Similar observations were made for the spherical PtNi NPs after identical treatments in the alkaline solution, Figure. 7. 7. However, a larger decrease in the Ni content at the NP surface was obtained for s-PtNi as compared to oct-PtNi after the first 20 cycles in the alkaline solution. Whether that is exclusively attributable to a shape effect or whether a size effect is co-involved remains speculative given our data. Subsurface Ni atoms may prefer to move away from the surface and alloy within the NP core during cycling; or else, Pt may be more mobile due to its lower average surface coordination and hence preferably surface segregate. Also, in contrast to the octahedral NPs, the dominant Pt component in the spherical NPs remained metallic Pt.

After 20 and 100 voltammetry cycles in the acidic solution, a strong decrease in the Ni/Pt ratio is observed, Figure. 7. 7(c). In light of the TEM measurements, such observation can be attributed to the selective surface Ni dissolution in the acid electrolytes. Interestingly, in this case platinum appears to be partially oxidized (Pt^{2+}), while nickel is partially reduced, Figure. 7. 7(a),(b). Here, the partial oxidation of Pt might be again related to the low Pt coordination or due to the removal of the protective Ni shell into the electrolyte during the acidic potential cycling.

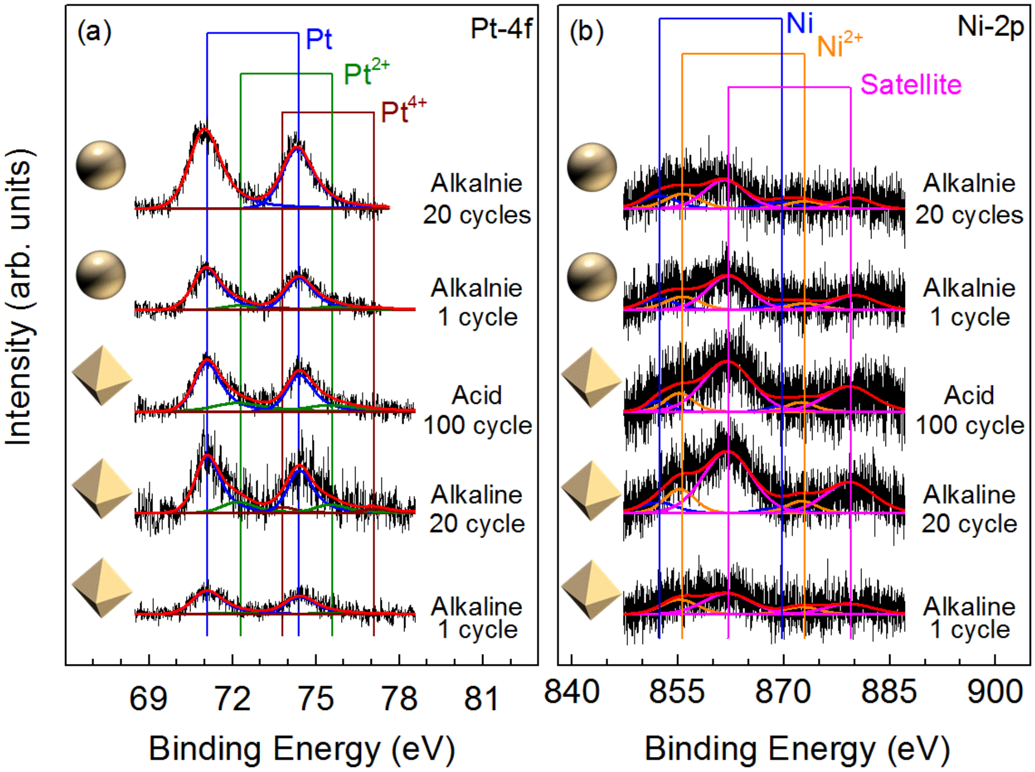

Figure 7. 6. XPS spectra from the (a) Pt-4f and (b) Ni-2p core level regions of octahedral and spherical PtNi NPs supported on a high surface area carbon black acquired after different voltammetry cycles in alkaline and acid solutions.

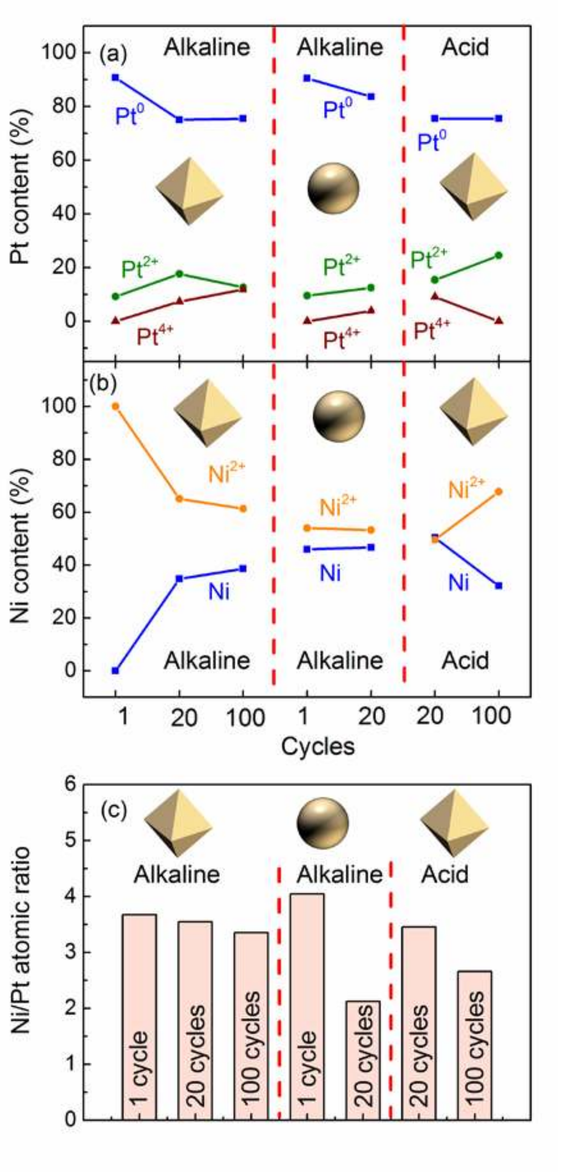

Figure 7. 7. Relative content of (a) Pt and (b) Ni species extracted from the XPS measurements in Figure. 10. (c) Ni/Pt atomic ratio obtained after a different number of voltammetry cycles in alkaline and acid solutions.

7.3.3. Electrocatalytic activity

Hydrogen evolution in alkaline conditions

The electrocatalytic reduction of water to molecular hydrogen (hydrogen evolution reaction, HER) in an alkaline electrolyte was chosen by our collaborator (Strasser group, TU Berlin) as a model reaction to test the impact of acid and alkaline surface pretreatments. This reaction is of great importance for neutral and alkaline water splitting for chemical energy storage applications. While alkaline water electrolysis is generally preferred based on catalyst cost, an efficient HER catalysts for alkaline media is missing. Pt is the best know HER electrocatalysts in acidic conditions, however, it displays severe overpotentials (efficiency losses) in alkaline solutions. Figure 7. 8 (a) presents the cyclic voltammetric behavior of the "1-alkaline" pretreated Pt/C, oct-PtNi/C, and s-PtNi/C catalysts in an alkaline base electrolyte over a wide potential range from 0.05 to 1.0 V in order to show the H_{upd} as well as the water activation / PtOH formation regions. The pure Pt NPs show sharper H_{upd} as well as PtOH features (0.3 V and 0.8 V), while the alloy NPs exhibit much broader potential waves in either region. In agreement with earlier studies on PtNi[257], the alloy NPs exhibit a reduced H_{upd} charge due to the reduced interaction of atomic hydrogen with Ni-containing surface and subsurface layers. The onset of water activation occurs fairly early, namely at around +0.5 V for both catalysts. No obvious difference can be detected between the spherical and the octahedral NPs. Figure 7. 8(b) presents the hydrogen evolution reactivity in the alkaline electrolyte (blue, green, red) of Pt/C after the acid and alkaline pretreatments, and compares those with the activity of the hydrogen evolution on Pt in acidic electrolytes. The cathodic shift of the alkaline HER curves evidences that Pt is a much better electrocatalyst in acid than in alkaline solutions. The HER reactivity of Pt in alkaline solutions appears largely independent of the surface pretreatment, Figure. 7. 8(b). In contrast to Pt, PtNi/C NPs showed a significantly improved HER behavior, approaching that of pure Pt in acidic conditions. We assume that the presence of Ni in the NPs is responsible for the general increase in the HER activity of the alloys. The pretreatments were found to induce noticeable differences in the HER activity. The "100-acid"-pretreated sample catalyzes the HER less efficiently as compared to the "20-alkaline" sample. The redistribution of surface Pt and Ni hydroxide species coupled with the emergence of lower, more favorable surface Ni/Pt ratios for HER could explain the additional activity gain of the "20-alkaline" catalyst. On the other hand, acid cycling associated with a strong depletion in Ni hydroxide on the NP surface could be responsible for the observed decrease in HER activity. As the data of spherical s-PtNi/C NPs in Figure. 7. 8(d) illustrate, the influence of the NP shape on the catalytic HER activity is relatively small.

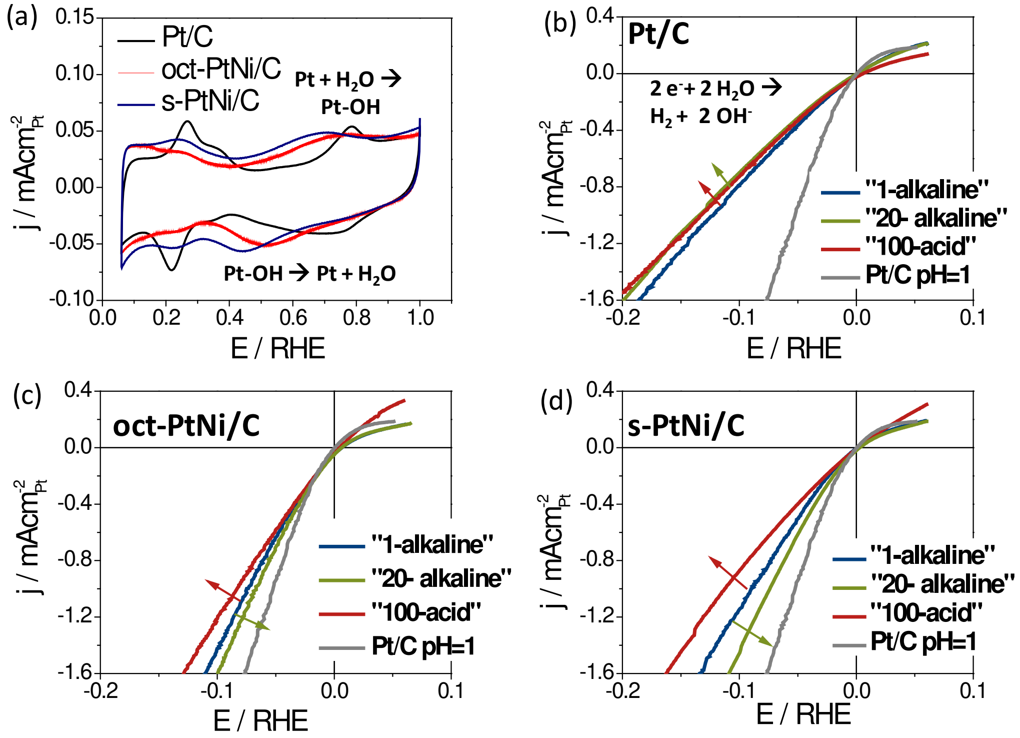

Figure 7. 8. (a) Cyclic voltammetry of spherical Pt/C, oct-PtNi/C, and s-PtNi/C NPs in 0.1 M KOH, (b) – (d) electrocatalytic HER activity in an alkaline 0.1 M KOH electrolyte (pH 13) of (b) Pt/C, (c) oct-PtNi/C, and (d) s-PtNi/C after pretreatments in alkaline and acid solutions.[Measurements carried out by the Strasser group at the TU Berlin and included in our joint publication, Ref [249]]

7.3.4. Bifunctional electrocatalysts through environment-induced segregation

The HER catalysis served as model systems to demonstrate the drastic effect that pretreatments in electrochemical environments can have on surface structure and composition as well as on catalytic activity. Figure 7. 9 illustrates our hypotheses, based on the TEM, XPS and reactivity results, as to the surface chemical transformation during the electrochemical measurements. After synthesis, the (111) surfaces of oct-PtNi/C NPs consisted of a mix of Pt surface atoms and surface $Ni(OH)_2$. After an initial alkaline pretreatment cycle (“1-alkaline”) the surface formed a thick Ni hydroxide-rich layer, while the low electrode potentials reduced surface Pt oxides to metallic Pt. Ni was likely present in its α-Ni hydroxide phase (green balls), which is the most stable Ni surface compound in the electrode potential range considered[258, 259]. Previous studies have shown that potential cycling can heal defects, and help remove low-coordinated adatoms analogous to thermal annealing in the gas phase[260]. Along these lines, the present cycling in alkaline caused surface compositional changes and geometric rearrangements in the surface to attain the energetically most favorable state of the alloy surface. The existence of hydroxide anions in the electrolyte generally favors the presence of Ni oxides in the top layer, ["20-alkaline" in Figure 7. 9]. However, XPS also evidenced that potential cycling reduced the surface Ni/Pt ratio. This could be due to either Pt surface segregation because of the Ni reduction, or to Ni inward diffusion and alloy formation in the NP core driven by the heat of alloying of Pt and Ni.

Cycling pretreatment in acid environments selectively leached a significant portion of the surface Ni hydroxide species from the surface and subsurface region of the octahedral catalysts[261], resulting in an essentially Ni-free surface enclosing a subsurface PtNi alloy core (core-shell structural arrangement). When tested in acid conditions, the subsurface Ni of the acid-leached PtNi NPs caused only a slight CO oxidation activity enhancement as evidenced by the 130 mV shift of the major oxidation peak. When tested in alkaline solutions, however, ("alkaline CO/HER electrolysis" in Figure. 7. 9) the hydroxide anions appeared to have caused a partial re-segregation of Ni species to the surface, evidenced by the emergence of the Ni-related CO oxidation peak around 0.5 V (marked "Ni"). The renewed presence of Ni surface species in the alkaline tested "100-acid" NPs was responsible for the activity enhancement in HER relative to pure Pt NPs.

Owing to their Ni hydroxide-rich surface, the alkaline-pretreated NPs showed a catalytic HER activity approaching that of pure Pt in acidic conditions. Interestingly, the effect of the NP shape on surface chemistry and electrocatalysis was smaller than anticipated, and appeared negligible as compared to the drastic compositional segregation effects.

The HER is probably the most intensely studied reaction in electrochemistry[262, 263]. Its mechanism in alkaline solution is treated as a combination of the Volmer reaction step (4) involving the dissociation of water to form a weakly adsorbed reactive H_{ad} intermediate, followed by either the Tafel recombination (5) or the Heyrovsky step (6) according to:

$$2\ H_2O + * + 2\ e^- \rightarrow 2\ H_{ad} + 2\ OH^- \qquad (7.1)$$

$$2\ H_{ad} \rightarrow H_2 + 2\ * \qquad (7.2)$$

$$H_{ad} + e^- + H_2O \rightarrow H_2 + OH^- + * \qquad (7.3)$$

The initial formation of the active adsorbed hydrogen (7.1) from a water molecule is generally considered a slow reaction step, making the activation of water a critical process to enhance the HER catalysis in alkaline solutions. The HER in acidic solutions, in contrast, involves the initial discharge of hydronium ions, which proceeds much faster associated with high HER activity. The oxophilicity and affinity to water adsorption of Ni-hydroxides has been well established in the past[257, 264-267]. Based on that, we attribute the increased catalytic HER activity of the segregated PtNi alloy NPs, in particular, of the alkaline-pretreated NPs, to the improved water dissociation at Ni hydroxide patches (clusters) on the NP surface as compared to Pt surface atoms (see inset B in Figure. 7. 9). Pt surface atoms adjacent to the Ni hydroxide accommodate the discharged reactive atomic hydrogen (H_{ad}) and subsequently catalyze reactions (7.2) and/or (7.3). Combined, the Pt/ $Ni(OH)_2$ system represents a bifunctional electrocatalyst with considerably enhanced HER activity. Furthermore, the study of the “100 acid” PtNi/C NPs demonstrated that efficient bifunctional Ni hydroxide cluster formation can originate from subsurface Ni species, and thus does not need to be carried out by deposition or coating of Ni clusters[257].

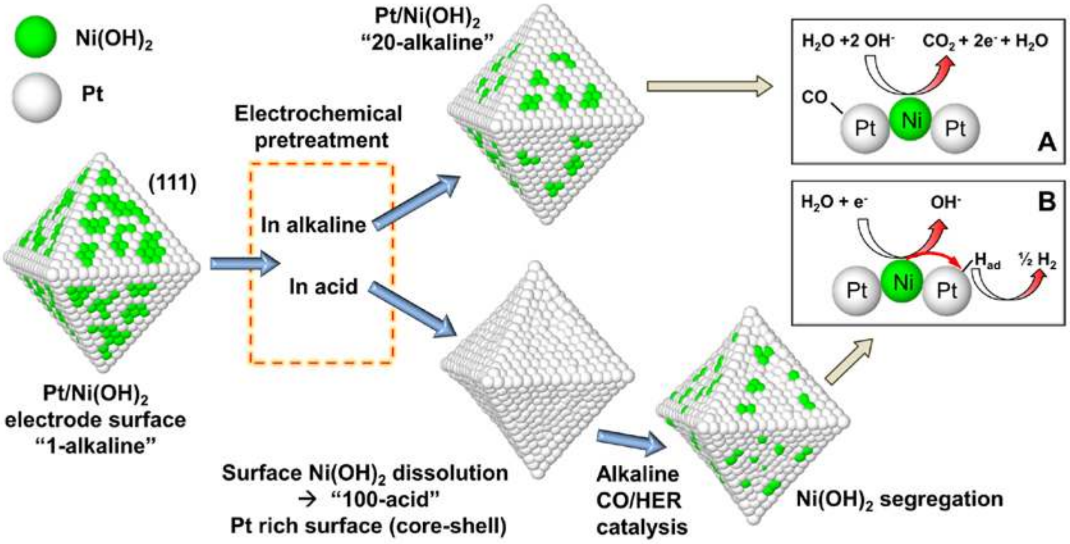

Figure 7. 9. Electrochemical surface dissolution/segregation processes in various electrochemical environments. CO oxidation and HER are enhanced due to bifunctional effects at Pt atoms adjacent to oxophilic Ni(OH)$_x$ islands.

7.4. Conclusions

Gas-phase chemical and liquid electrochemical environments can induce significant compositional and structural changes in solid alloy surfaces, especially those in the nm-size regime. Chemical and electrochemical environments form distinctly different types of interfaces to solids. For example, due to the absence or presence of an electrified double layer and mobile ions, distinctly different molecular interactions with surfaces are possible. However, our study demonstrates that gas-solid and liquid-solid interfaces also display commonalities, indicating certain unifying basic physico-chemical concepts.

Under various gaseous environments, octahedral PtNi NPs showed Ni/Pt ratios > 1 and followed the trend: $(Ni/Pt)_{O2}$ >$(Ni/Pt)_{Vacuum}$ >$(Ni/Pt)_{H2}$. Furthermore, the latter trend directly correlates with the relative Ni^{2+} content in our samples. Interestingly, the initial presence of NiOx species on the as-prepared samples played a pivotal role in the atomic segregation observed before the onset temperature for drastic NiOx reduction (i.e., below 300°C). In particular, when a large content of NiOx species was present on the as-prepared samples, preferential Ni segregation to the NP surface was observed, even in reducing environments.

In analogy to the oxygen gas-phase pretreatments, electrochemical hydroxide anions stabilized thick Ni hydroxide-rich surfaces during the initial potential cycle. Subsequent cycles established a surface with more balanced Pt:Ni hydroxide ratios with novel synergetic properties. Acidic electrochemical environments caused the selective removal of surface Ni species, a reactive pathway generally less common in gas-phase environments. The alkaline pretreated catalyst NPs showed significantly increased CO electrooxidation and electrocatalytic hydrogen evolution activity for which the water activation ability of surface-segregated Ni hydroxides is held responsible. Coupled with the formation of suitable adjacent Pt surface atomic ensembles, the Ni hydroxide islands represents the self-organized formation of efficient bifunctional catalysts.

We expect that similar electrochemical segregation phenomena could occur in other Pt bimetallic alloy NPs or surface reactions, especially where surface active electrolytes or reactants are involved. As an example, during the electrocatalytic reduction of molecular oxygen, the catalyst surface may transform under *operando* conditions and change its catalytic properties due to emerging synergistic bi- or multifunctionalities.

CHAPTER 8: LONG RANGE SEGREGATION PHENOMENA IN SHAPE-SELECTED BIMETALLIC NANOPARTICLES: CHEMICAL STATE EFFECTS

8.1. Introduction

Bimetallic catalysts have numerous advantages as compared to their monometallic counterparts, such as enhanced activity, selectivity, and durability.[268] For instance, when combined with secondary metals (M) such as Ni, Fe, Cu, Co or Ti, increased activities have been observed for Pt-based catalysts in oxygenate reforming reactions,[269-272] the oxygen reduction reaction (ORR),[20, 252, 273-276] hydrogenation reactions,[277, 278] CO oxidation,[220, 279, 280] and CH_4 reforming.[18, 281] In all of these applications, the manipulation of the geometrical and electronic properties of the resulting alloy, in particular, the Pt-Pt bond length (strain effects) and the position of the d-band center are considered to play a key role in the unusual properties displayed by the bimetallic systems.

A variety of methods have been employed for the synthesis of bimetallic nanoparticle (NP) catalysts, with special focus dedicated to improving their activity and stability under reaction conditions in different gaseous or liquid (electrochemical) environments.[167, 246, 252, 276, 282-285] Changes in their structure and surface composition, leaching and dissolution of a given element, as well as coarsening are the main factors responsible for the loss in the activity of these catalysts.[286-288] Decreased NP mobility and sintering has been achieved for Pt-based catalysts through alloying with Co, Fe and Ni.[286, 287, 289] Although dissolution of Pt-based catalysts in acidic environments is commonly described as a negative characteristic leading to a decrease in activity,[290, 291] in certain cases it was reported to result in improved catalytic performance *via* the increase of the surface roughness.[261, 292, 293]

Overall agreement exists on the importance of the structure of the bimetallic alloys. Segregation phenomena or alloy formation processes in bimetallic systems are determined by the interplay between the surface energy of each element, their atomic radius, and the chemical ordering energy [difference in energy between structures with (i) a periodic appearance of the two elements in the lattice and (ii) the completely disordered analog with randomly positioned elements].[294] In general, a higher ordering energy is expected to hinder segregation processes.[294] Based on the phase diagram of bulk PtNi alloys, $Pt_{0.5}Ni_{0.5}$ has a chemically disordered FCC structure above its order-disorder transition temperature, T_C^{Bulk} = 900 K, and a chemically ordered L_{10} phase below that temperature.[295] However, for nanoparticles T_C^{NP} might differ from T_C^{Bulk} depending on the NP size and shape.[234] The degree of chemical ordering of an alloyed NP is expected to drastically affect its segregation behavior. For instance, while in a chemically disordered system, the segregation process is a smooth function of the NP stoichiometry (Pt/Ni ratio), in an ordered system the segregation behavior could vary significantly with only slight changes in the stoichiometry, *e.g.* for $Pt_{0.50}Ni_{0.50}$, versus $Pt_{0.51}Ni_{0.49}$ and $Pt_{0.49}Ni_{0.51}$.[294] In addition, while a chemically-ordered structure may be thermodynamically favorable for an equiatomic composition at room temperature, depending on the NP growth kinetics, the chemical structure of bimetallic NPs could be initially disordered and remain disordered until it is treated at high temperature.[296-298] Usually, the presence of oxidized species or inhomogeneities in the initial elemental distribution of NPs leads to chemically disordered systems. Also, the phase diagram, the order-disorder transition temperature, and the atomic segregation behavior of clean bimetallic NPs is likely distinct from that of the corresponding oxidized or adsorbate-covered NPs.[234, 299]

Sandwich structures with thin Pt overlayers deposited on 3d-metal surfaces [Pt-3d-Pt(111)] have been proven to be more effective catalysts than pure Pt for low-temperature hydrogenation reactions,[277, 278, 300] while for oxygenate reforming processes, 3d-metal overlayers on Pt surfaces [3d-Pt-Pt(111)] displayed the greatest activity. [301, 302]In the realm of electrocatalysis, a (111) oriented Pt_3Ni surface, thermally segregated into a Pt skin structure was found to be the most active structure for the electrocatalytic reduction of molecular oxygen to water.[273] In contrast, the electrocatalytic oxidation of CO or small organic molecules is most efficiently catalyzed by Pt-Ru and Pt-Sn alloys.[303]

More importantly, the structure of the catalysts might change depending on the reaction conditions, making *in situ* and *operando* studies crucial for the understanding of structure-reactivity correlations in material systems prone to segregation. For example, by annealing a 3d metal-Pt-Pt(111) structure in vacuum, Pt was found to surface segregate, turning this material from an effective oxygenate reforming into a hydrogenation catalyst.[301, 304] On the other hand, 3d-metal-Pt-Pt structures were the most stable in oxygen environments. Surface segregation of Pt was observed experimentally for PtRu NPs in a H_2 environment[305] and theoretically predicted for Pt-M (Ni, Re, Mo) NPs.[234, 306] Annealing PtCo NPs treated in acid solutions also lead to Pt surface segregation and the formation of sandwich-Pt structures. [275]

The current study focuses on the *in situ* evolution of the structure and surface composition of shape-selected octahedral Pt-Ni NPs under different chemical environments (O_2, H_2, vacuum). This material system is of interest due to its use in a broad range of industrial catalysis applications. Owing to the exclusive exposure of (111)-oriented facets, it has been thought as an ideal electrocatalysts for the electroreduction of oxygen.[20, 178, 243, 249, 274, 303] Even though among all 3d-metals Ni has the highest energy barrier for segregation,[307] the presence of adsorbates can drastically promote Ni surface segregation. DFT calculations showed low potential for Ni surface segregation in H, S, Se or C environments due to their weak surface/subsurface bonding, while adsorbates such as O or N were found to promote segregation.[308] Reversible changes in the structure of (5-20 nm) Pt-Ni NPs prepared *via* deposition-precipitation were recently reported, with Ni-surface enrichment in oxygen and Pt-richer surfaces in H_2 after annealing at 300°C. [309] Our work describes the morphological stability and atomic segregation phenomena in size- and shape-selected octahedral Pt-Ni NPs supported on HOPG, with emphasis on the influence of pre-existing oxides on the segregation trends observed. The NP shape was resolved by TEM. *In situ* XPS and *ex situ* AFM were used to monitor the effect of diverse gaseous environments on the structure and surface composition of $Pt_{0.5}Ni_{0.5}$ alloy NPs. To demonstrate the effect of surface composition on catalytic reactivity, correlations were established for the electrocatalytic CO oxidation reaction on the three different pre-treatments in vacuum, hydrogen, and oxygen at 300-350°C. The results from catalytic CO stripping measurements were found to be fully consistent with the XPS-derived Ni surface segregation and PtNi alloying trends in the three environments.

8.2. Experimental

Octahedral Pt-Ni bimetallic NPs with a Pt:Ni ratio of 1:1 were prepared using wet-chemical methods (a solvothermal process at elevated pressure),[251] with Dimethylformamide (DMF) serving as solvent, surfactant, and reducing agent.[20, 178, 252] The as-prepared solution was five-fold diluted with isopropanol and drop-coated on HOPG substrates after 10 min of sonication. The dilution allowed a better dispersion and lack of agglomeration of the as-prepared NPs on the HOPG supports.

Transmission electron microscopy (TEM) images were obtained by a FEI TECNAI G2 20 S-TWIN transmission electron microscope with LaB6–cathode. The microscopy work was carried out with an accelerating voltage of 200 kV.

Thermal treatments in different environments were conducted in a high pressure (HP) reaction cell (SPECS GmbH). The HP cell was evacuated after each treatment and the samples transferred to the attached UHV system without exposure to air. The XPS measurements were acquired *in situ* using a monochromatic x-ray source (Al-kα, 1486.6 eV) operating at 350 W and a hemispherical electron analyzer. For the XPS study, three identical $Pt_{0.5}Ni_{0.5}$ NP samples were isochronally annealed in 1 bar O_2, 1 bar H_2, and vacuum environments for 20 min at temperatures ranging from RT to 650 °C. All XPS spectra were measured at RT after the respective heating cycles. The high resolution XPS data were acquired using a pass energy, E_{pass}, of 18 eV. The XPS spectra were analyzed using the CASA XPS software[250]. All spectra were aligned using the C-1s peak from the graphite support at 284.3 eV as reference.

In order to extract information about the changes in the sample morphology, size, and dispersion of the $Pt_{0.5}Ni_{0.5}$ NPs under the different environments, three identical $Pt_{0.5}Ni_{0.5}$ NP samples were *in situ* annealed in 1 bar O_2, 1 bar H_2, and UHV as described above. Subsequently, AFM measurements were acquired *ex situ* at room temperature in tapping mode.

Thermally-treated $Pt_{0.5}Ni_{0.5}$ NPs supported on HOPG were characterized with respect to their electrocatalytic oxidation of adsorbed CO monolayers during anodic potential scans ("CO stripping") in alkaline 0.1M KOH electrolytes. All electrochemical measurements in this thesis were carried out by the Strasser group at the TU Berlin This procedure has been routinely carried out to assess the CO oxidation activity of electrocatalysts or to determine the real surface area of a Pt electrocatalyst.[310-312] After bubbling the electrolyte with Ar at room temperature for 15 min to remove all traces of dissolved air, CO was bubbled for 15 min at an applied electrode potential of 0.05 V/RHE at which a stable saturated monolayer of adsorbed CO forms at the surface of the catalyst. Subsequently, under continued potential control at 0.05 V/RHE, dissolved CO was removed by bubbling Ar gas for another 15 min, such that only the adsorbed CO layer remained in the electrochemical system. Finally, the electrode potential was scanned at 50 mV/s from +0.05 to +1.0 V/RHE to record the CO electrooxidation. One additional potential cycle was conducted in order to record the value of the hydrogen underpotential deposition (H_{upd}) charge and to establish the electrochemical baseline of the $Pt_{0.5}Ni_{0.5}$ NP catalyst.

8.3. Results and Discussion

Figure 8. 1 shows a TEM image of ~9 nm $Pt_{0.5}Ni_{0.5}$ NPs in an as-prepared sample. The PtNi NPs show a narrow size distribution and a consistent octahedron shape.

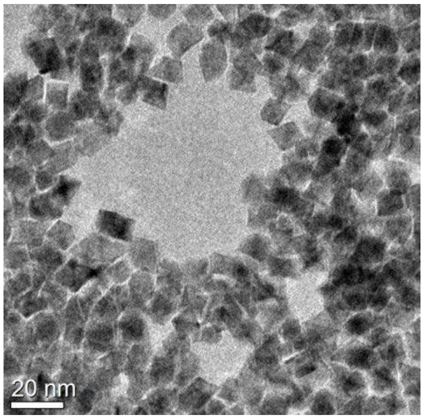

Figure 8. 1. High resolution TEM of octahedral PtNi NPs supported on commercial carbon (Vulcan XC-72).

Figure 8.2 displays *ex situ* AFM images of three identically prepared fresh octahedral PtNi NP/HOPG samples (a-c) together with images acquired RT after annealing at 150°C (d-f) and 250°C (g-i). The first column displays pictures acquired after annealing in vacuum, the second column after H_2, and the third column after O_2. Initially (fresh samples) the NPs are homogenously dispersed over the entire support surface. Annealing in vacuum leads to a progressive decrease of the average NP size without significant sintering, although a less homogenous coverage of the support surface by the NPs is observed. In contrast, identical treatments in H_2 and O_2 lead to enhanced NP mobility, and the preferential decoration of HOPG steps already at 150°C. Under oxygen, a lower density of NPs on HOPG terraces is observed at all temperatures as compared to hydrogen, suggesting enhanced atomic (Ostwald ripening) and/or NP (diffusion-coalescence) mobility. In addition, agglomeration of NPs is observed on certain support regions after the treatment in O_2, with other areas showing large uncoated voids. According to Ref. [313], in the case of pure Ni NPs, preferential bonding to oxidized and defect sites on HOPG was observed, which might explain the inhomogeneous NP dispersion on the support. Enhanced NP mobility was also seen under H_2 as compared to vacuum. Such facile movement is assigned to a weak binding of the $Pt_{0.5}Ni_{0.5}$ NPs to the HOPG support. Following related literature,[314-317] a very distinct behavior, *e.g.* lower atomic/NP mobility, might have been observed if these NPs would have been supported on an oxide substrate,[314, 315] where at low temperature and under oxidizing conditions a stronger oxidized metal NP/support is formed. On the weakly binding graphite, the exposure to either H_2 or O_2 seems to contribute to the de-stabilization of the NPs.

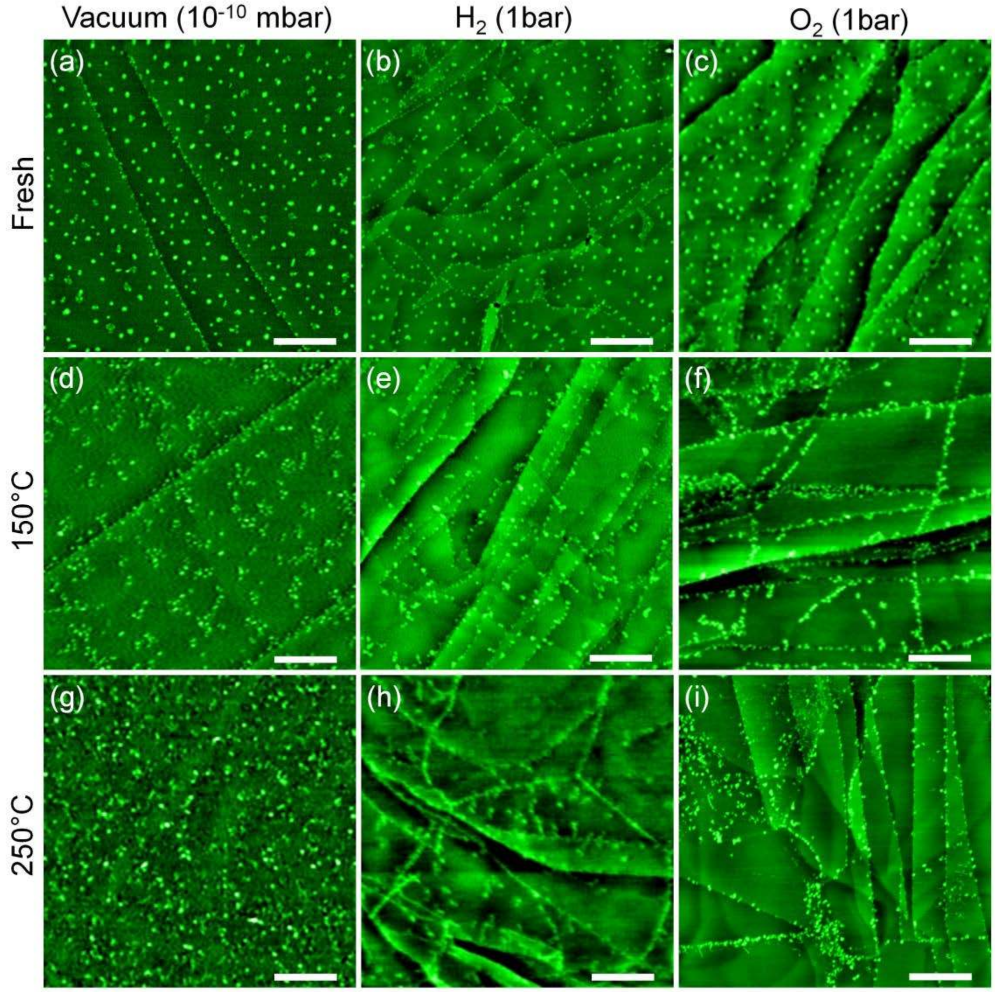

Figure 8. 2. AFM images of octahedral PtNi NPs supported on HOPG acquired at ex situ (air) at RT after the treatments indicated. Scale bars in all images are 400 nm.

XPS spectra from the Pt-4f (a-c) and Ni-2p (d-f) core level regions are shown in Figure. 8. 3 after annealing treatments in vacuum (a,d), 1 bar of H_2 (b,e) and 1 bar of O_2 (c,f). In agreement with literature references,[27, 318, 319] the Pt-4f XPS data were fitted with three doublets corresponding to metallic Pt ($4f_{7/2}$, 71.2 eV), Pt^{2+} ($4f_{7/2}$, 72.4 eV), and Pt^{4+} ($4f_{7/2}$, 73.7 eV). The Ni-2p region was also fitted with three double peaks assigned to metallic Ni ($2p_{3/2}$, 852.5 eV), Ni^{2+} ($2p_{3/2}$,855- 856.2

eV), and satellite features corresponding to the NiOx species (861, 878.2 eV).[255, 320, 321] The evolution of the oxidation state of the PtNi NPs is shown in Figure. 8. 4.

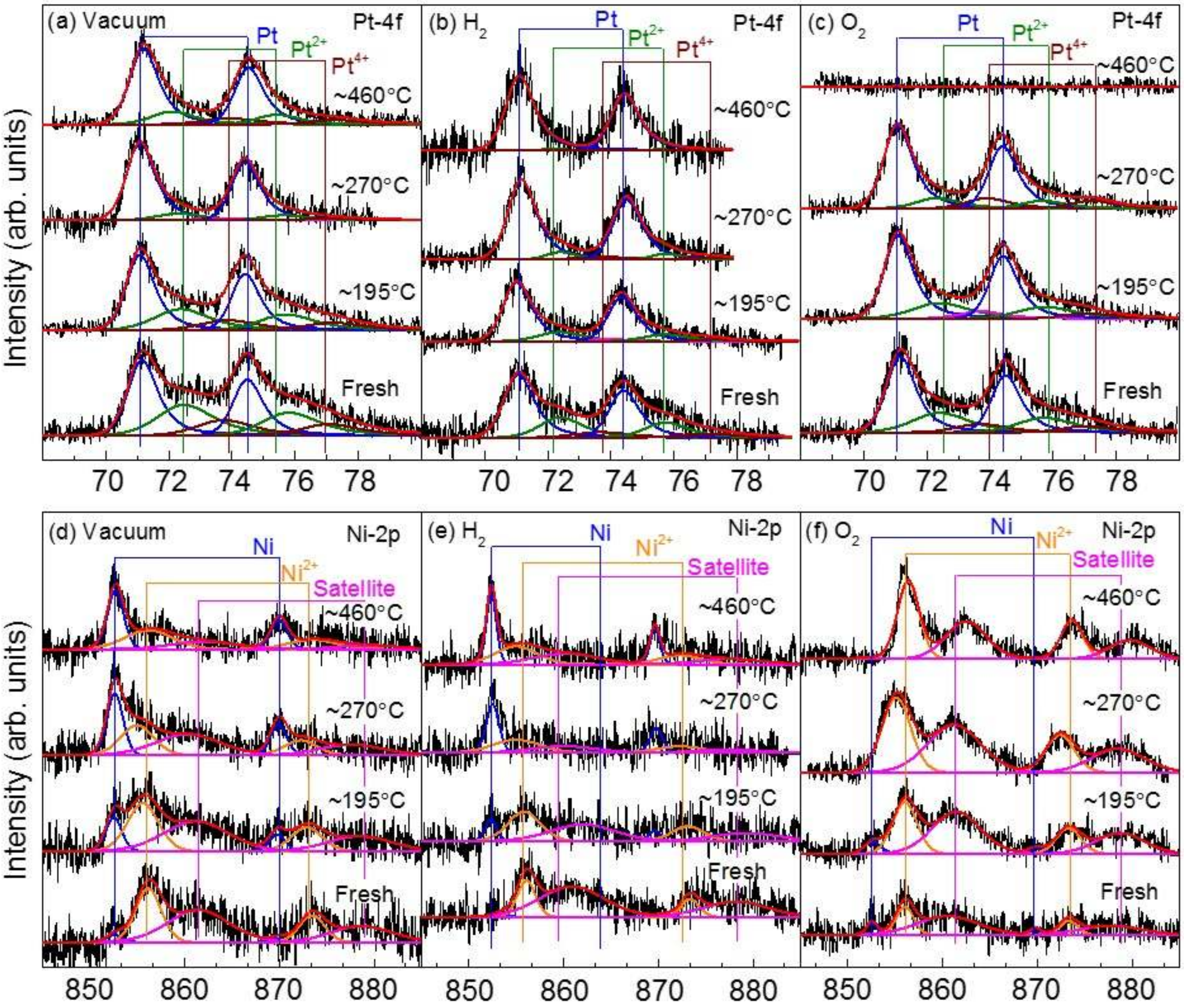

Figure 8.3. XPS spectra from the (a-c) Pt-4f and (d-f) Ni-2p core level regions of PtNi NPs supported on HOPG acquired at RT as prepared (fresh) and after annealing in vacuum and in 1 bar of O_2 and H_2 for 20 min at the indicated temperatures.

The *ex situ* prepared $Pt_{0.5}Ni_{0.5}$ NPs were initially composed of a significant fraction of Ni^{2+} species (NiO or NiOH, ~80-95 %), with Pt also partially oxidized [40-50 % Pt^{2+} and Pt^{4+} in the form of

PtO/PtO$_2$ or Pt(OH)$_{2x}$],[322, 323] Figure. 8. 4. Annealing in hydrogen up to 460°C only lead to the partial reduction of the Ni^{2+} species (~45 %), with significant Pt reduction above 270°C, but a small PtOx component still observed at 460°C. A faster reduction of the PtOx species in the 200-460°C temperature range was detected during the annealing in H$_2$ as compared to vacuum. Annealing in oxygen resulted in a progressive increase in the Ni^{2+} content, with partial decomposition of the Pt$^{\delta+}$ species up to 270°C, and the complete loss of the Pt signal at 460°C, Figure. 8. 3(c).

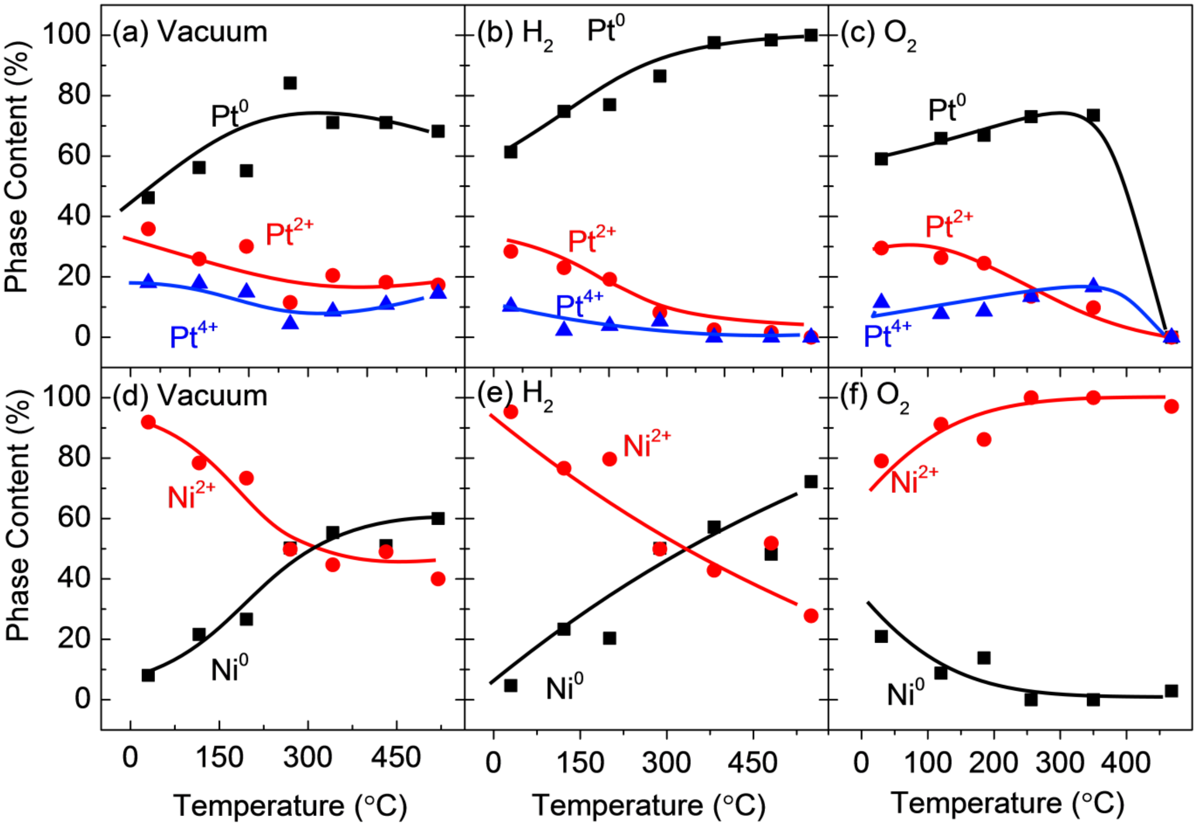

Figure 8. 4. Relative content of (a-c) Pt and (d-f) Ni species extracted from the analysis of XPS data acquired after annealing in vacuum (a,d), 1 bar of H$_2$ (b,e) and 1 bar of O$_2$ (c,f).

The Ni/Pt atomic ratio after the thermal treatment under the different gaseous atmospheres is shown in Figure. 8. 5.

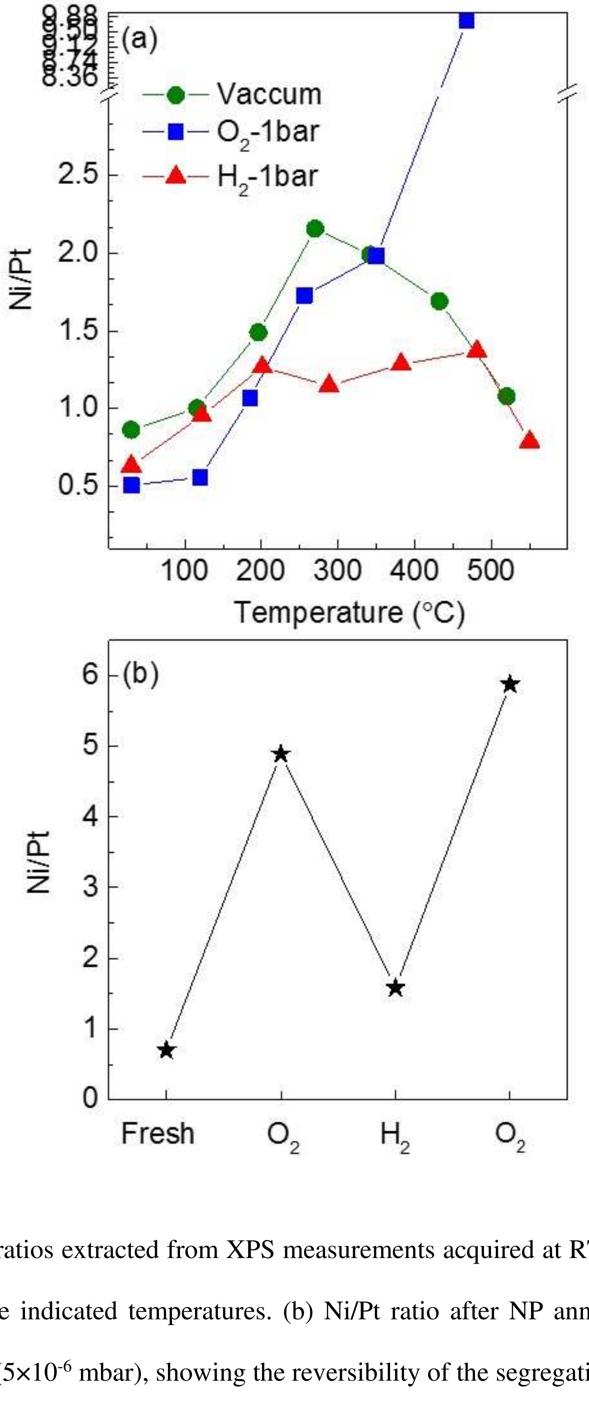

Figure 8. 5. (a) Ni/Pt atomic ratios extracted from XPS measurements acquired at RT after annealing in O_2 (1 bar), H_2 (1 bar), and vacuum at the indicated temperatures. (b) Ni/Pt ratio after NP annealing at 450°C in O_2 and H_2 environments at low pressure (5×10^{-6} mbar), showing the reversibility of the segregation/alloying process.

In the absence of adsorbates, due to the larger atomic radius of Pt and despite of its slightly higher surface energy (2.475 J/m^2) as compared to Ni (2.45 J/m^2),[324] Pt segregation to the NP surface is expected.[234, 294] Although it has been shown that the size, shape, and stoichiometry of the NPs affect their segregation behavior,[234, 325] consensus exists regarding the formation of Pt-rich overlayers on (111) and (100) surfaces in cases where segregation takes place.[234, 294, 326, 327] However, such segregation is limited only to the first few atomic layers at the surface, commonly resulting in the formation of a Pt skin or sandwich structure, in which the first atomic layer is Pt-rich and the second layer is Ni-rich. Such structure might be achieved through a short-range atomic exchange near the surface, with Pt atoms in the second layer switching places with their neighboring Ni atoms at the surface. However, the small changes in the Pt and Ni signals brought about by the formation of the Pt skin might not be detectable with common laboratory XPS systems (1486.6 eV X-rays in this case). This is due to the small contribution of the top-most surface layers considering the photoelectron inelastic mean free paths involved (~1.8 nm for Pt photoelectrons and ~1 nm for Ni). Here we should highlight that such short-range segregation should not be confused with the long-range segregation that would result in phase-separation or core-shell structure formation reported for other systems.[198, 261, 328] In most cases, long-range segregation phenomena occur for systems in which the two metals have a different crystalline structure, such as Pt-Ru with fcc and hcp structures, respectively, or Fe-Au with bcc and fcc structures, which is not the case for Pt-Ni (both fcc).

In the present study, an increase in the Ni/Pt ratio was observed for our samples in vacuum and in H_2 at low temperature (<270°C in vacuum and <200°C in H_2, remaining subsequently stable up to 460°C in H_2). This trend is assigned to the initial chemical state of the *ex situ* prepared NPs, which was characterized by the presence of oxygen at surface/subsurface regions. Due to the much higher affinity of Ni for oxygen as compared to Pt (NiOx formation energy of -2.54 eV per O versus PtO, PtO_2 formation energies of -0.41 eV and -0.63 eV per O),[329] Ni surface segregation is observed under reducing atmospheres until significant oxygen removal (oxide decomposition) is achieved, which was found to occur here above 270°C in vacuum and above 200°C in H_2.

In vacuum, a change in the Ni/Pt ratio is observed, with a drastic decrease above 270°C. The same phenomenon is not seen under hydrogen until 460°C, with the Ni/Pt ratio continuously increasing up to 200°C, and then remaining nearly constant from 200-460°C, until a drop in the Ni/Pt ratio is finally observed at 550°C. The strong reduction of the Ni/Pt ratio observed at high temperature is assigned to the interdiffusion of reduced Pt and Ni species and the formation of a homogenous PtNi alloy.

The Ni surface segregation taking place when oxygen is present on the NP surface is considered to proceed *via* the replacement of Pt atoms in surface PtOx species by Ni. Such trend explains our experimental results showing different temperature regimes for the changeover from Ni surface segregation to Pt-Ni interdiffusion in different environments (*i.e.* vacuum versus H_2), primarily depending on the temperature required for the full removal of PtO_x species, and secondarily by the continuous depletion of O from Ni-rich NP regions. The reduction of the PtO_x species at low temperature was found to stop the Ni outward segregation and at high temperature, the reduction of Ni oxide species results in Pt-Ni intermixing through alloy formation. The former arguments explain why the Ni/Pt ratio does not increase as much in H_2 as in vacuum due to the earlier reduction of the PtO_x species in H_2, which hinders the segregation of Ni. The later illustrates the lack of change of the Ni/Pt ratio between 200-460°C in H_2, since the more drastic Ni reduction, favoring the alloy formation, occurs at higher temperature (≥ 500°C).

When the samples are annealed in oxygen, the progressive segregation of Ni to the NP surface and the concomitant formation of NiO species was detected, with a drastic increase in the Ni/Pt ratio above 350°C, and the complete disappearance of the Pt signal in XPS at 460°C, Figure. 8. 3(a). The loss of the Pt signal could be attributed to (i) its inward segregation (towards the NP core), with the Pt XPS signal being suppressed by the presence of the overlaying Ni shell, or (ii) the loss of Pt in the form of volatile PtO_2 compounds. In order to corroborate the likelihood of the first scenario, the inelastic mean free path (IMFP) of Pt-4f photoelectrons in Ni (~1.9 nm) should be compared to the thickness of the NiO shell. For $Pt_{0.5}Ni_{0.5}$ NPs of our initial size, the IMFP is not expected to be much smaller than the NiOx shell thickness, and therefore, no substantial damping of the Pt XPS signal should have been observed, provided that no significant sintering takes place during the annealing treatment in oxygen at 460°C, as observed *via* AFM. The second scenario, namely, that involving the loss of Pt is more likely. Nevertheless, such possibility should also be cautiously considered, since the NiO shell formed under these conditions might serve to protect the Pt at the NP core. However, it is plausible that the Pt atoms have enough mobility at high temperature to reach the NP surface and desorb as PtO_2 after coming into contact with oxygen. The latter effect might explain the counterintuitive increase in the content of Pt^0 species with increasing temperature in oxygen, Figure. 8. 4(c), due to PtO_x removal from the NP surface.

Figure 8. 5(b) shows data obtained under O_2, H_2, and again O_2 at 450°C at a pressure of $5x10^{-6}$ mbar, revealing that the segregation-alloying process is reversible. However, the slight decrease in the Ni/Pt ratio observed after the second annealing cycle hints towards a similar Pt loss in O_2 as described above for a higher O_2 pressure treatment (1 bar) through its volatilization as PtO_2.

Figure 8. 6 schematically illustrates the atomic segregation trends extracted from our *in situ* XPS data. Figure 8. 6(a) shows the as prepared sample with a PtNi alloy in the core and Pt/Ni oxide species near the surface due to the exposure of the NPs to air after preparation. As was shown in our previous study,[330] the corners and edges of the NP are Pt-rich, while the facets are Ni-rich. This is a result of kinetic phenomena taking place during the NP synthesis. Annealing in vacuum up to ~300°C results in Ni atoms exchanging their positions with Pt atoms in oxide species (mainly at and near the NP surface), leading to the formation of a Ni oxide shell and a Pt rich core. Both, Ni and Pt species get partially reduced within this temperature range, Figure. 8. 6(b). Annealing in vacuum at higher temperatures (*e.g* 500°C), results in the reduction of Ni and the consequent interdiffusion of Pt and Ni atoms, leading to the formation of a uniform PtNi alloy, Figure. 8. 6(c). The shape of the NPs is not expected to remain stable at these high temperatures and therefore, the NPs are shown here with a truncated octahedron shape. In the case of the annealing in hydrogen, the reduction of Pt oxides occurs much earlier and therefore, the Ni-Pt exchange is not as extensive as when the samples are annealed in vacuum, Figure. 8. 6(d), as indicated by the lack of significant change in the Ni/Pt ratio within the 200-400°C temperature range. At high temperature, the alloy formation in H_2 is similar to that observed in vacuum, with the exception of a more extensive $Ni^{\delta+}$ and $Pt^{\delta+}$ reduction, Figure. 8. 6(e). Annealing in oxygen brings the Ni out towards the NP surface, resulting in a completely oxidized NiO shell, in contrast to the cases of annealing in vacuum and H_2, Figure. 8. 6(f). At last, annealing in O_2 at high temperature (460°C) was found to result in the partial or total loss of Pt *via* the formation of volatile PtO_2, with the NPs mainly composed of NiO species, Figure. 8. 6(g). It should also be considered that our octahedral PtNi NPs are kinetically formed, and thus they do not represent the most thermodynamically stable shape. Therefore, at moderate temperatures (*e.g.* 500°C in the schematic of Figure. 8. 6), the loss of the octahedral

shape is expected. Although cubo-octahedral PtNi NPs were shown to have a slightly lower energy (0.003 eV per atom) than NPs with octahedral shape[234], any conclusion on what shape should be experimentally observed should be considered with caution. Due to the presence of adsorbates or surface/subsurface oxides under common experimental conditions, the reconstruction on (100) facets, which is the main reason for the cuboctahedron shape to be the more thermodynamically favorable, is expected to be lifted.[234] Additionally, it should be noted that none of the NPs in our study are completely reduced even after treatment at the highest temperature shown (460°C), and therefore, any prediction of their shape should include their oxidation state as well. Thus, the final shape of a NP may vary after treatment in different environments depending on its oxidation state as well as on adsorbate-induced modifications of its surface energy.

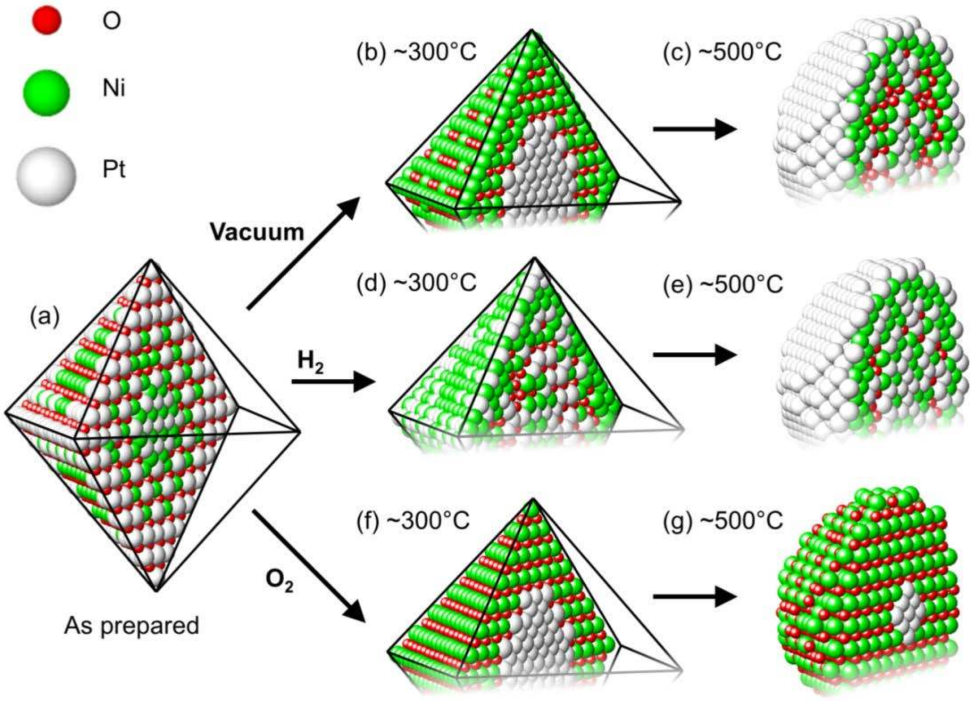

Figure 8. 6. Schematic models describing the segregation of Pt and Ni atoms in octahedral $Pt_{0.5}Ni_{0.5}$ NPs (a) as-prepared, and after annealing from 25°C to 500°C in the following environments: (b,c) vacuum (10^{-10} mbar), (d,e) H_2 (1 bar), (f,g) O_2 (1 bar).

The surface composition of a catalyst generally affects its catalytic reactivity. To demonstrate this for thermally treated $Pt_{0.5}Ni_{0.5}$ octahedral NPs, the electrocatalytic CO oxidation reaction was chosen. Catalyzed by the surface of the shaped Pt-Ni NPs, the electrochemical CO oxidation reaction involves the activation of water to surface OH followed by its reaction with adsorbed CO to CO_2. The reaction process proceeds according to:

$$H_2O + * \rightarrow OH_{ad} + H^+ + e^- \tag{8.1}$$

$$CO_{ad} + OH_{ad} \rightarrow CO_2 + H^+ + e^- + 2\,* \tag{8.2}$$

, where * denotes an active surface site for water activation. Earlier CO stripping studies on PtNi NPs showed that there exist two types of water activation sites[249]: (i) surface Ni oxide sites that act as highly active water activation promoter sites, shifting the CO stripping peak towards a more cathodic electrode potentials between 0.3 – 0.6 V/ RHE. (This potential range is shaded in Figure. 8. 7). (ii) Pt surface sites which may as well serve as water activation sites, however, these sites promote such process at more anodic potentials, and as a result of this, they yield anodic CO stripping charge in the potential range of 0.6 – 1.0 V/RHE, Figure 8. 7.

CO electrooxidation (CO stripping) was carried out using a single anodic voltammetric potential sweep between 0.05 V and 1.0 V/ RHE, Figure. 8. 7. The first CO stripping cycle (red in Figure. 8. 7) was followed by a second baseline voltammetric cycle (black in Figure. 8. 7). The total charge of the difference between the black and red voltammograms corresponds to the amount of electro-oxdized (and typically to the amount of initially adsorbed) surface CO. The recorded instantaneous Faradaic currents correspond to the CO oxidation reaction rate, while the CO oxidation peak potentials bear (often non trivial) relationships to CO and water chemisorption. Figure 8. 7 displays the CO stripping voltammetry of one of the (a) vacuum-treated (350°C), a (c) hydrogen- treated (300°C), and (c) an oxygen-treated (350°C) $Pt_{0.5}Ni_{0.5}$ NP catalyst sample. It is evident that the peak profiles of the three differently-treated samples show characteristic differences. It is plausible that, given the otherwise identical experimental conditions, the observed differences in the CO oxidation profiles are linked to their different surface compositions after the distinct thermal pre-treatments underwent before the electrochemical measurements. To corroborate this hypothesis, we recall the earlier findings mentioned above regarding the CO stripping potentials and the presence of Ni oxide surface species.[249] CO oxidation charges, Q, were analyzed for the potential region associated with the presence of surface Ni oxides. The vacuum-annealed sample showed a

Q value of 100 μC, while the H_2-treated and O_2-treated samples showed charges of 88 μC and 160 μC, respectively. These values clearly suggest that the oxygen-treated NPs oxidize CO to a large extent under the promotion of surface Ni oxide species. The H_2-treated NPs, in contrast, appears to show the least Ni oxide promotion, associated with the most metallic surface Pt character, while the vacuum-treated NPs show an intermediate behavior. These conclusions are fully commensurate with the surface compositional discussion above based on XPS results and offer a consistent composition-activity relationship.

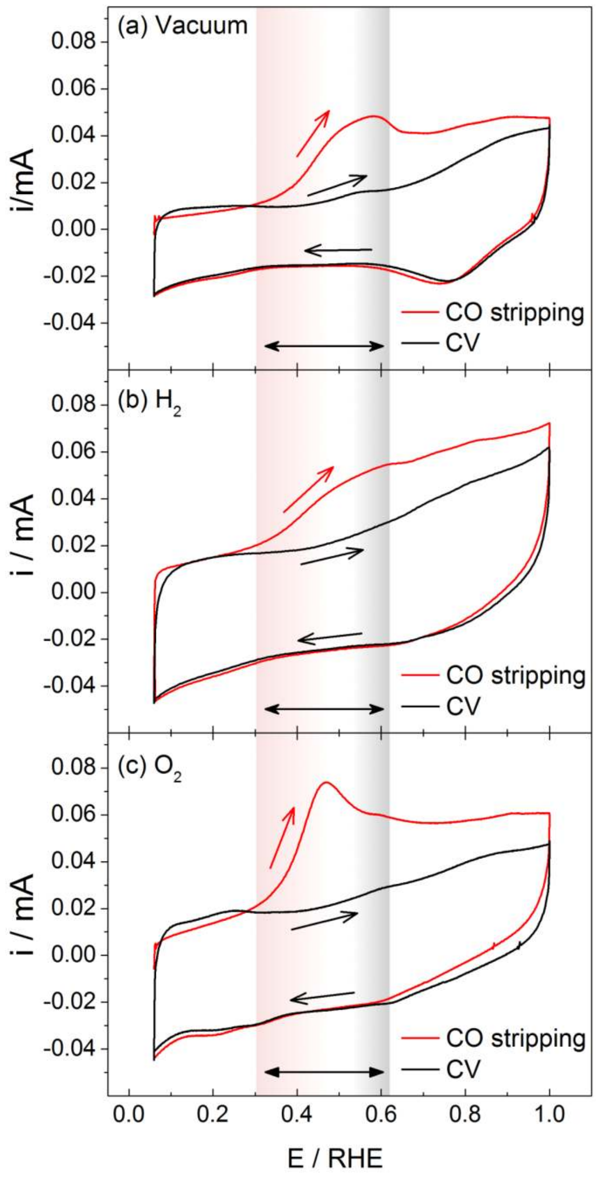

Figure 8. 7. CO monolayer stripping voltammetry of octahedral $Pt_{0.5}Ni_{0.5}$ NPs after treatments under reactive gases and ultrahigh vacuum. The first stripping cycle in shown in red, the second baseline voltammetric cycle in black, and scan directions are indicated by arrows. (a) 350°C in vacuum, (b) 300°C in H_2, and (c), 350°C in O_2. Conditions: CO adsorption at 0.06 V/ RHE, 50 mV/s, 0.1M KOH. The shaded potential range (0.3 – 0.58 V/RHE) indicates where CO stripping occurs by NiO_x-promoted water activation (eq. 8.1 and Ref.[249])[Data acquired by Strasser group at TU berlin].

8.4. Conclusion

Size- and shape-selected octahedral NPs supported on HOPG have used as model system to study atomic segregation phenomena in $Pt_{0.5}Ni_{0.5}$ NP catalyst under different gaseous environments (1 bar H_2, 1 bar O_2 and vacuum). Because of the presence of oxygen species on the *ex situ*-prepared fresh samples and the high oxygen affinity of Ni, Ni segregation to the NP surface was observed in all environments at low temperature (T<200-270°C). Such result is explained in terms of a place exchange replacement process of Pt in surface PtOx species by Ni. In vacuum, Ni surface segregation continued up to 270°C, above which the segregation of Pt to the NP surface was observed. In H_2, Ni segregation (an increase in the Ni/Pt ratio) ceased as early as 200°C, possibly attributable to the earlier reduction of surface oxide species under H_2 exposure. Subsequently, the Ni/Pt ratio remains nearly constant in H_2 between 200-460°C, above which Pt-surface enrichment was detected. It is reasonable to assume that the formation of the stable PtNi alloy is responsible for the compositional plateau. Thermal treatments in oxygen lead to a drastic Ni surface segregation and the formation of NiO species. Under such environment, a NP configuration with a thick NiO shell and a small PtNi alloy core was inferred, with Pt being lost as PtO_2 at/above 460°C.

CO electrooxidation was used as a model reaction to demonstrate how the surface composition affects the catalytic reactivity of the shaped Pt Ni NPs after pre-treatment in different gaseous atmospheres within the 300-350°C temperature range. Being a sensitive diagnostic tool for Ni oxide surface species, CO stripping voltammetry confirmed the predominant presence of Ni oxides in the O_2-treated NPs, a largely Pt metallic character of the H_2-treated NPs, and the intermediate state of the vacuum-annealed NPs.

Our study highlights the importance of the initial chemical state of the NPs, in particular, the presence of oxygen, on the subsequent NP structural and chemical stability and atomic segregation trends. Furthermore, it illustrates how different adsorbates, commonly present in catalyst break-in pre-treatments under *operando* conditions, can affect the composition of their surface and near-surface regions, and therefore, also their reactivity.

CHAPTER 9: CARBON MONOXIDE-INDUCED STABILITY AND ATOMIC SEGREGATION PHENOMENA IN SHAPE-SELECTED OCTAHEDRAL PtNi NANOPARTICLES

9.1. Introduction

Bimetallic NP catalysts have been extensively investigated in the past,[331-335] due to the many advantages they could offer as compared to their monometallic counterparts. Different factors such as synergetic effects between elements, a change in the electronic structure, and strain effects have been held responsible for their high efficiency and tunable catalytic performance.[286, 334, 336, 337] Two of the most widely used metals in gaseous and liquid phase catalytic reactions are Pt and Ni. In addition, a bimetallic combination of such metals as an alloy or core-shell structure has also been shown to display superior catalytic performance for reactions such as ethanol reforming,[270] methane and methanol reforming with CO and CO_2,[218, 281, 338, 339] oxygen reduction reactions (ORR),[20, 252, 276, 334, 340] CO oxidation,[20, 242, 341-345] and methanol electro-oxidation.[337, 346, 347]

The spatial atomic distribution in bimetallic catalysts plays a pivotal role in their electronic properties, in particular, in the shift of the d-band center, which is known to affect the binding energy of reactants to the NP surface.[336, 348, 349] Therefore, understanding the structure and chemical composition of bimetallic NPs is of outmost importance for the rational design of highly efficient bimetallic catalysts. For example, Gauthier *et al.* observed higher binding energy of CO on Pt atoms in the PtCo(111) system by increasing the number of nearest neighbor Co atoms, and explained this behavior through a shift in the d-band center towards the Fermi level.[350] Such shift was also held responsible for the higher activity of Ni-Pt-Pt(111) as compared to Pt-Ni-Pt(111) for the reforming of oxygenates.[351-353] In contrast, for hydrogenation reactions, a d-band center further away from the Fermi level was reported to lead to higher hydrogenation activity.[354-356]

Strain effects are also important in understanding the behavior of bimetallic catalysts. For example, lower binding energy of oxygen to $Pt_{(shell)}Ni_{(core)}$ as compared to Pt(111) was shown and assigned to the compression of the Pt lattice in the former structure. Nevertheless, by increasing the Ni concentration on the NP surface, an increase in the binding energy of O_2 has been reported.[357] In contrast, in the same PtNi bimetallic system, the binding energy of CO was reported to first decrease with increasing Ni concentration, but was found to increase again for very large Ni surface contents upon segregation.[358, 359]

Although the initial atomic distribution of the different metallic components in bimetallic nanocatalysts is of importance, structural changes during catalyst operation conditions are key to understanding the catalyst reactivity. The surface energy, atomic size, chemical ordering energy, composition, size of the NPs, and the adsorption enthalpy of adsorbates are all key factors affecting the segregation and structure of nanoscale catalysts.[216, 226, 249, 294, 339, 343, 350, 360-368] The present work addresses the role of adsorbates such as CO on the structural and chemical stability of shape-selected octahedral PtNi NPs at different temperatures.

Carbon monoxide is one of most commonly used and produced molecules in catalytic reactions. Therefore, understanding CO-induced structural changes in nanoscale catalysts is valuable for designing catalysts with higher stability, yield, and selectivity. Mayrhofer *et al.* have reported CO-induced segregation of Pt atoms to the surface of Pt_xCo_y alloys through both, gas-phase annealing and electrochemical CO potential cycling in CO saturated electrolyte, and explained this behavior based on the higher adsorption enthalpy of CO on Pt as compared to Co.[216] Tenny *et al.* observed Pt segregation to the surface of bimetallic PtAu NPs upon CO exposure at room temperature.[369] The surface composition of Ni/Cu(100) was studied during the hydrogenation of CO_2, and Cu segregation to the surface was observed. However, by adding CO to the reactant stream, such segregation was hindered due to the higher binding energy of CO to Ni as compared to Cu.[218, 339, 361] A dissimilar trend was observed in the case of Co/Cu(100) because of the lower binding energy of CO to Co as compared to Ni.[218, 339, 370] Additionally, Ni surface segregation in Ni_xCu_{1-x} alloys in the presence of CO and O_2 was predicted theoretically.[361] An increase in the surface concentration of Ru was theoretically predicted after exposing Pt/Ru(0001) samples to 1 bar of CO.[364] Surface segregation of Pd and Cu in AuPd(100) single crystals and CuPt near-surface alloys was observed in the presence of CO.[360, 371, 372] Interestingly, a negative segregation energy for Ni atoms dissolved in Pt was predicted in the presence of CO, which leads to a preference of Ni to stay in the interior of bimetallic NiPt NPs.[361]

Because of the importance of the PtNi system as a bimetallic catalyst and CO as a reactant, we present here an investigation of the stability and atomic segregation phenomena in size- and shape-controlled PtNi NPs supported on HOPG supports in the presence of CO. The *ex situ* NP preparation method and initially oxidized nature of the as-prepared NPs make this study of relevance for industrial applications. Since the segregation phenomena also depend on the crystal orientation, [373, 374] in order to reduce the complexity of the multiple parameters simultaneously affecting segregation phenomena at the nanoscale, we have prepared octahedral NPs with just (111) facets.

The NP surface composition and their coarsening behavior were examined using XPS and AFM. The shape of the as-prepared NPs was resolved using TEM.

9.2. Experimental

Octahedral $Pt_{0.5}Ni_{0.5}$ bimetallic NPs were prepared at the TU Berlin (Strasser group) *via* a solvothermal process at elevated pressure, with dimethylformamide (DMF) serving as solvent, surfactant, and reducing agent.[252, 330, 375] The as-prepared NP solution was 5-fold diluted with isopropanol and drop-coated on HOPG substrates after 10 min of sonication.

In order to extract information about the chemical state and surface composition of the NPs, XPS measurements were acquired using a monochromatic X-ray source (Al Kα, 1486.6 eV) operating at 350 W and a hemispherical electron analyzer. Three initially identical $Pt_{50}Ni_{50}$ samples were prepared. One of the samples (S1) was stepwise annealed in vacuum ($\sim 1\times10^{-10}$ mbar) from 25°C to 700°C for 20 min at each temperature in 100°C intervals. A second sample (S2), was exposed to 1 bar CO for 10 min at room temperature (prior to each annealing step), and subsequently stepwise annealed in vacuum under the same conditions as S1. For sample S2, after annealing in vacuum at a given temperature, XPS spectra were taken before (S2-Before) and after CO dosing at 25°C (S2). Sample exposure to CO was conducted in a high pressure (HP) reaction cell (SPECS GmbH). For the third sample (S3), after annealing in 1-bar CO in a HP reaction cell, XPS spectra were taken. After each exposure, the HP cell was evacuated to $\sim 1\times10^{-8}$ mbar and the sample transferred *in situ* directly to the XPS analysis chamber without exposure to air. All XPS spectra were aligned using the graphite C-1s peak at 284.3 eV as a reference.

TEM images were obtained with a FEI TECNAI G2 20 S-TWIN TEM operating at an accelerating voltage of 200 kV. To investigate NP mobility and coarsening after different thermal and chemical treatments, AFM images were acquired *ex situ* at RT in tapping mode. The AFM study was conducted on three identical $Pt_{50}Ni_{50}$ samples. Two of them were treated as described before for the XPS study (S1 and S2) with 50°C temperature increment, and a third sample (S3) was annealed in 1 bar of CO from 50°C to 200°C in 50°C intervals. A summary of the different treatments is shown in Figure 9. 1.

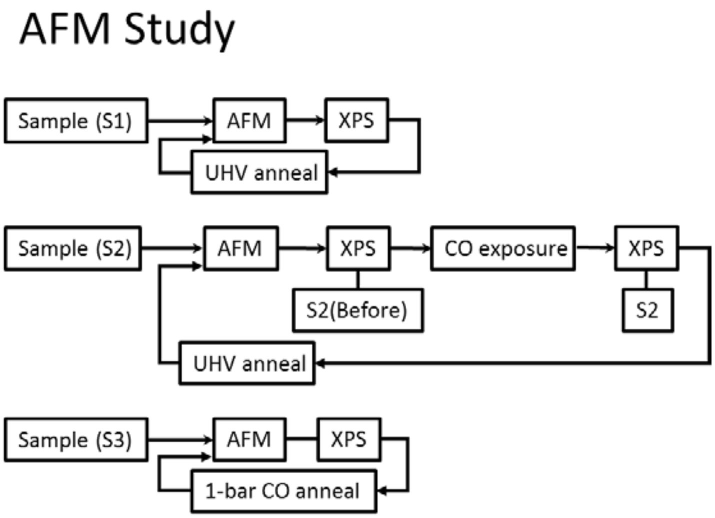

Figure 9. 1. Overview of the different treatments underwent by the Pt$_{0.5}$Ni$_{0.5}$ NPs.

9.3. Results and Discussion

Figure 9. 2 shows a TEM image of our octahedral Pt$_{50}$Ni$_{50}$ NPs. The NPs are ~9.0 ± 1.1 nm in diameter and have a narrow size distribution.[375]

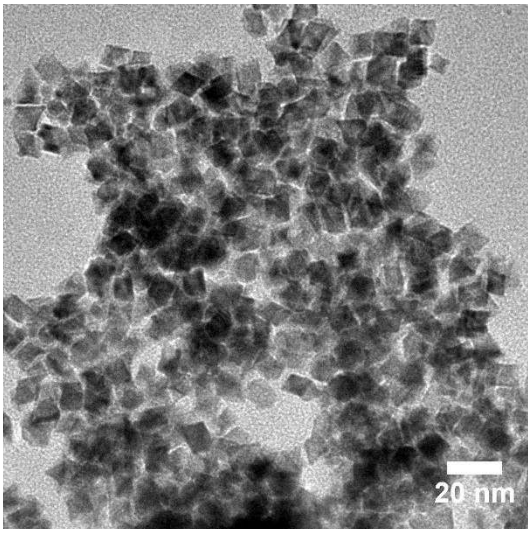

Figure 9. 2. TEM image of octahedral $Pt_{0.5}Ni_{0.5}$ NPs.

Ex situ AFM images of three initially identical $Pt_{50}Ni_{50}$ NP samples acquired at 25°C are displayed in Figure 9.2. Images (a-d) correspond to sample S1 and were acquired after annealing in vacuum for 20 min at the indicated temperatures. Images (e-h) were obtained from sample S2 after *in situ* exposure to 1 bar of CO at 25°C followed by sample annealing during 20 min in vacuum at the indicated temperatures, and (i-l) after annealing in 1 bar of CO for 10 min at the given temperatures. In the as prepared samples the NPs are homogenously dispersed over the entire substrate surface. In all samples, the decoration of the HOPG step edges by the NPs at moderate temperature indicates their high mobility on the support surface.

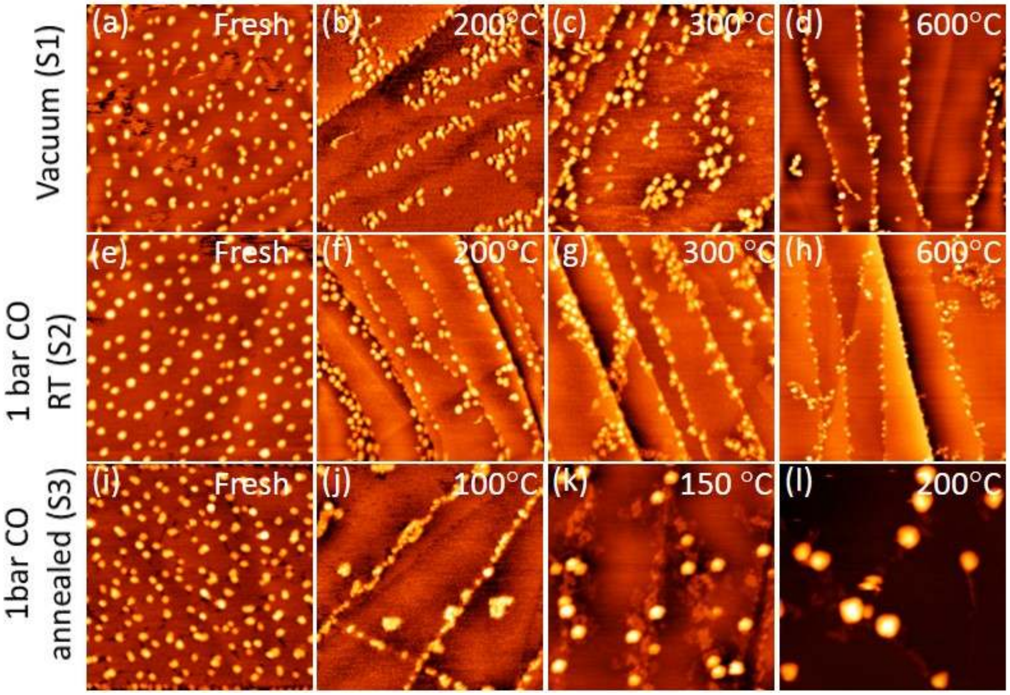

Figure 9. 3. AFM images of octahedral $Pt_{0.5}Ni_{0.5}$ NPs supported on HOPG acquired *ex situ* (air) at 25 °C after annealing in UHV (top row), after dosing 1 bar of CO at 25°C and subsequent annealing in UHV (middle row), and after annealing in 1 bar of CO (bottom row). All images display a 1×1 μm sample region.

The average NP size as a function of temperature is shown in Figure 9.4. A minimum of ~ 150 NPs has been considered for each data point. In order to better compare the evolution of the size of the CO-exposed and vacuum-treated samples, the NP sizes are normalized by the initial (as-prepared) average size. The progressive decrease in the NP height of ~15% observed after CO dosing and subsequent annealing in vacuum (S2) could be explained by the reduction of the initially oxidized NPs and removal of oxygen from the NPs structure, which is corroborated by the XPS data shown in the next section. In contrast, vacuum annealing without any CO pre-exposure (S1) lead to a slight decrease (~15 %) in NP height at moderate temperature (<200 °C), while significant coarsening (~45% increase in height) was seen after annealing above 250°C. On the other hand, when the NPs were annealed in 1 bar of CO (S3), drastic coarsening (over twenty times the initial size) was found to take place even at moderate temperature (150°C-200°C). The high coarsening rate of the NPs in S3 may be explained based on the formation of $Ni(CO)_4$ species, their diffusion on the graphite surface, and subsequent decomposition. In particular, Shen *et al* showed a high Ni carbonyl decomposition rate at temperatures above 130°C.[376, 377] Although nickel carbonyl formation might take place even at RT, the presence of NiO_x species on the NPs in S2 at temperatures below 100°C is expected to hinder such process and therefore, contrary to the case of sample S3, no low-temperature coarsening is expected for S2, which was only pre-exposed to CO at 25°C.

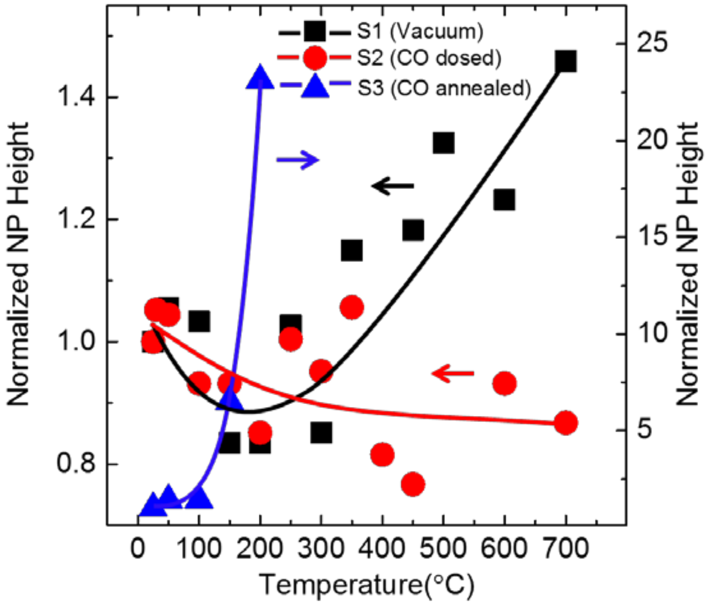

Figure 9. 4 Normalized height of $Pt_{0.5}Ni_{0.5}$ NPs after a thermal treatment in vacuum (squares, S1), after 1 bar CO dosing at 25°C followed by annealing in vacuum (circles, S2), and after annealing in 1 bar of CO (triangles, S3).

XPS spectra of Pt-4f (a-c) and Ni-2p (d-f) core level regions of samples S1, S2 and S3 are shown in Figure 9.5. As described above, two initially identical samples were prepared. Sample S1 was annealed in vacuum in the absence of any gas dosing and XPS spectra were acquired after each annealing step, Figure 9.5(a,d) (S1). Sample S2 was first annealed in vacuum and subsequently exposed to 1 bar CO at room temperature 4(b,e) (S2) after each annealing step. Sample S3 was annealed in the presence of 1-bar CO, and XPS spectra were acquired after each annealing step, Figure 9.5(c,f) (S3). The Pt-4f core-level region was deconvoluted by three doublets corresponding to metallic Pt ($4f_{7/2}$, 71.1 eV), Pt^{2+} ($4f_{7/2}$, 71.8 eV), and Pt^{4+} ($4f_{7/2}$, 73.4 eV).[318, 319, 378] The Ni-2p region was also fitted with two doublets assigned to metallic Ni ($2p_{3/2}$, 852.2 eV), Ni^{2+} ($2p_{3/2}$, 856.3 eV), and satellite Ni features (861-863.5 eV).[379-381] The Ni-2p region of sample S3 was also fitted with an additional doublet corresponding to Ni(CO)x species (Ni-$2p_{3/2}$, 854 eV).[382] It is worth mentioning that a binding energy increase of only ~0.2 eV is expected for Pt and Ni upon formation of the Ni-Pt alloy,[383] which is close to the limit of our experimental resolution for these kind of NP samples, where even in the metallic state for monometallic systems, positive binding energy shifts are observed due to initial and final state effects.

The phase content of the different metallic and oxidic Pt and Ni species extracted from the XPS spectra in Figure. 9.5 is displayed in Figure 9.6. The Ni atoms in the fresh samples are mostly oxidized (~98%), with Pt also partially oxidized (~40-50%). Annealing up to 700°C in UHV results in the partial reduction of Ni^{2+} (~50-55%) for samples S1 and S2. With increasing annealing temperature, a decrease in the PtO_2 and parallel increase in the PtO signal is observed, indicating the stepwise decomposition of the oxidized Pt species. Annealing in 1-bar CO also resulted in the partial reduction of the NPs, with ~10-15% PtOx and ~30% NiOx remaining at 700°C. Furthermore, the formation of nickel carbonyl species was also observed between 300°C and 500°C. It is worth mentioning that the reduction rate of PtO_x and NiO_x was not significantly affected by room temperature CO exposure. However, annealing in 1-bar CO (S3) led to a stronger decrease in the content of Ni^{2+} species, with ~30% at 700°C for S3 and ~50 % for S1 (vacuum annealed) at 700°C.

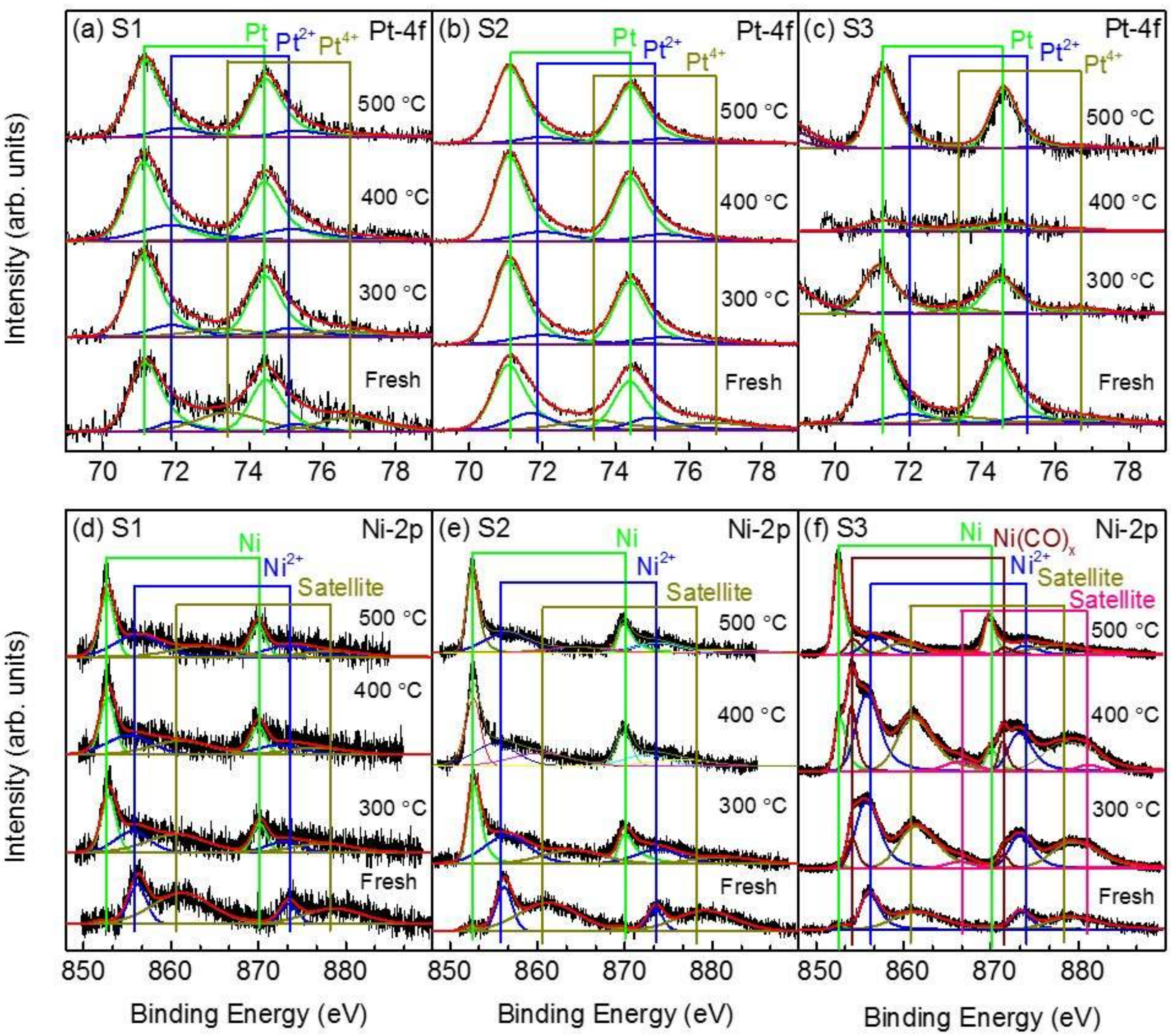

Figure 9. 5. XPS spectra from the (a-c) Pt-4f and (d-f) Ni-2p core level regions of $Pt_{0.5}Ni_{0.5}$ NPs supported on HOPG acquired at 25°C as prepared (fresh) and after annealing in UHV (S1-Vacuum) (a,d), and after exposure to 1 bar CO at 25°C before each annealing treatment and subsequent annealing in UHV (b,e) (S2-CO dosed) and after annealing in 1-bar CO (c,f) (S3- CO Annealed).

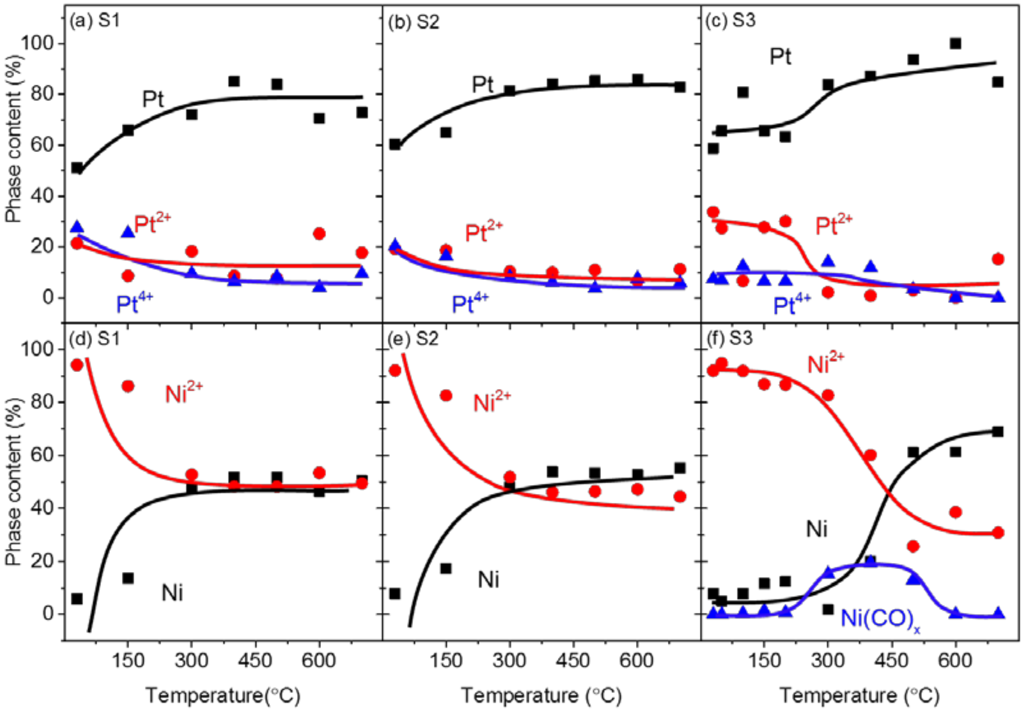

Figure 9. 6. Relative content of Pt (a,b) and Ni (c,d) species extracted from the analysis of XPS data acquired after annealing in UHV (S1-Vacuum) (a,d), and after exposure to 1 bar CO at room temperature and subsequent annealing in UHV (S2-CO dosed) (b,e) and after annealing in 1-bar CO (c,f) (S3- CO annealed).

In order to gain insight into atomic segregation phenomena, the Ni/Pt ratio was obtained from the XPS data, Figure 9.7. Two competitive causes are responsible for the atomic segregation trends observed: (i) the higher binding energy of CO to Pt as compared to Ni and larger size of the Pt atoms leading to Pt surface segregation, (ii) the larger oxygen affinity of Ni as compared to Pt (oxygen is initially present in the *ex situ* as prepared samples due to air exposure after preparation). An increase in the Ni to Pt atomic ratio was obtained for both, the vacuum annealed sample (S1) and the CO pre-exposed sample (S2) up to 300°C for S2, 400°C for S3, and 500°C for S1.[343] This phenomenon may be explained based on the initial presence of PtO_x species on the surface of the as prepared NPs and consequent surface segregation of Ni atoms and Pt-Ni exchange as a result of the higher oxygen affinity for Ni as compared to Pt. Between 300°C and 500°C, however, the Ni to Pt ratio in sample S2 did not change significantly, while it continued to increase when no CO had been dosed before annealing (S1). This is in agreement with earlier theoretical calculations predicting a negative heat of segregation for Ni atoms dissolved in Pt in the presence of CO. The latter favors that Ni stays subsurface, closer to the NP core. In other words, because of the higher chemisorption bond energy of CO on Pt (134 kJ/mol) as compared to Ni (126 kJ/mol), Ni segregation to the NP surface becomes thermodynamically unfavorable.[361] The lower coarsening rate observed for the CO pre-exposed sample (S2) as compared to the vacuum-annealed sample (S1), could be explained based on the distinct initial (pre-UHV annealing) atomic arrangement of Pt and Ni induced by the CO chemisorption. As was shown, the initial CO exposure leads to Pt segregation to the NP surface, which appears to contribute to the NP stabilization against low-temperature coarsening in vacuum. On the other hand, the drastic coarsening observed in sample S3 after annealing in 1-bar of CO is likely related to the formation of Ni-carbonyl species upon moderate temperature annealing. Such volatile species are likely highly mobile on the graphite surface and might contribute to the increase in the NP size *via* adsorbate-driven coarsening. It is plausible that $Ni(CO)_x$ species transfer from small to larger NPs, giving rise to coarsened NPs with Ni-rich overlayers.[376]

Further annealing at higher temperature (T>500 °C) causes the reduction of Ni species and back diffusion of Pt atoms and formation of a PtNi alloy. Since the desorption temperature of CO from Ni is less than 500°C, no difference between the CO-pre exposed and vacuum-annealed samples is expected at higher temperature (T>500°C).[384] It should be noted that the observation of a larger Pt concentration on the surface of the CO-pre-exposed NPs at all temperatures might explain the higher stability of the CO-exposed sample (S2) as compared to the vacuum-annealed sample (S1) observed *via* AFM. Since Pt has a higher melting temperature than Ni, the larger concentration of Pt on the surface might help to decrease the coarsening process. The contrary would be the case of S3(annealed in 1 bar of CO), where the higher content of Ni species on the NP surface, in particular, of Ni-carbonyl species, appears to favor low temperature coarsening.

In fact, a very drastic increase in the Ni/Pt ratio was observed below 400°C for the sample annealed in CO (S3), Figure. 9.7. Such trend is explained based on the higher affinity of Ni for oxygen, leading to Ni surface segregation as long as oxide species are available on the NPs surface, but also based on the decrease in the Pt signal expected due to the NP coarsening observed via AFM. Since Pt is in the NP core and Ni on the surface, a thicker Ni overlayer present on the coarsened NPs due to the inter-particle migration of Ni-carbonyl species and redeposition on the larger NPs is expected to lead to an apparent decrease of the Pt signal and increase of the Ni/Pt ratio. The Pt signal is later on at least partially recovered upon annealing at and above 500°C, indicating a reversible Pt surface segregation and the formation of a Pt-Ni alloy. It is worth mentioning that maximum Ni/Pt ratio was reached at 400°C for S3, while it happened at 500°C for S2, this difference could be explained based on higher reduction rate of PtOx and NiOx species on sample S3, since Ni surface segregation is expected to stop when oxygen is not available at the NP surface. The insets in Figure 9.7 display the atomic distribution of Pt, Ni and O within the NPs in their as-prepared state, as well as after annealing in vacuum at 500°C before (S1) and after exposure to 1 bar of CO at 25°C (S2) and after annealing in 1-bar CO (S3). Based on an earlier TEM study[330], the as-prepared was found to contain Pt-rich edges and corners while the facets and NP core are Ni-rich. In addition, because of the ex-situ preparation method, the NP is mostly oxidized. After annealing in vacuum at 500°C (S1) a higher concentration of Ni atoms is observed at the NP surface as a result of their atomic exchange with Pt oxide species on the surface. Furthermore, annealing at 500°C in UHV lead to the partial reduction of the NPs. In contrast, when the NP are pre-exposed to CO at 25°C before each annealing step up to 500°C (S2), a higher concentration of Pt on the NP surface is detected as a result of stronger bonding energy of CO to Pt as compared to Ni. It should be noted that the octahedron shape of our NP is a result of the kinetic preparation procedure and it is not the most stable shape. Therefore a change in the NP shape towards a spherical shape is expected at moderate temperature. Such shape change (octahedral to spherical) is already indicated in the model of S3, the sample annealed in 1 bar of CO, where significant coarsening was observed already at temperatures as low as 200°C (Figure. 9.3). Moreover, the presence of a Ni-rich overlayer (Ni-carbonyl) and Pt-rich core extracted from the analysis of our XPS data is also illustrated in the model.

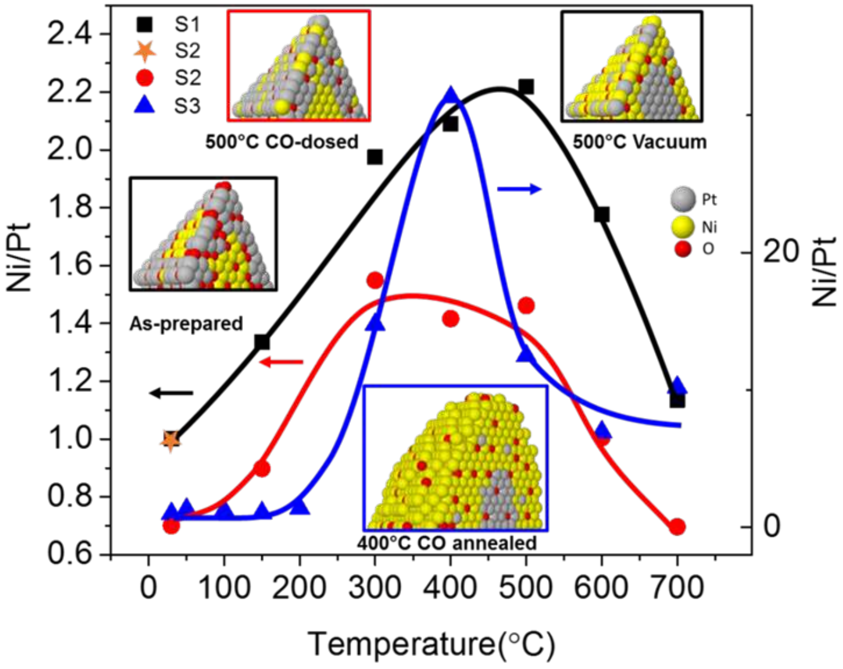

Figure 9. 7. Normalized Ni to Pt atomic ratios extracted from XPS measurements of $Pt_{0.5}Ni_{0.5}$ NPs in samples S1, S2 and S3 displayed after different annealing treatments and acquired at 25°C. The insets show models describing the segregation of Pt and Ni atoms in these NPs in their as-prepared state, and after annealing from 25°C to 500°C in

vacuum (S1), after pre-exposure to CO at 25°C and annealing at 500°C in vacuum (S2), and after annealing at 400°C in 1 bar of CO. The data point labeled as a star corresponds to S2 before CO exposure at 25°C and the rest of the data points labeled as circles for S2 were acquired after pre-exposure to CO at 25°C and subsequent annealing at the temperatures indicated.

9.4. Conclusion

In this study, the effect of CO pre-exposure on thermally-induced atomic segregation trends and consequent effect on the stability of PtNi NPs was explored. Size- and shape-controlled $Pt_{0.5}Ni_{0.5}$ NPs supported on HOPG were used to investigate atomic segregation phenomenon in the presence of carbon monoxide. For samples annealed in vacuum, an enhanced stability against particle coarsening was observed if the samples were pre-exposed to CO at 25°C before each thermal treatment in vacuum (S2). This could be attributed to the higher concentration of Pt atoms on the NP surface due to Pt surface segregation as was evidenced by XPS measurements. In contrast, when the samples were annealed in CO, drastic coarsening was detected at moderate temperatures (<250 °C). In all cases, significant NP mobility and the decoration of step edges of the HOPG support was seen.

Complex and distinctly different segregation patterns were observed for samples annealed in vacuum in the absence and presence of a CO-pretreatment at 25°C. At moderate annealing temperatures in vacuum (<300 °C), the segregation of Ni atoms to the NP surface was observed for all, the pristine (S1), the CO-pre-exposed (S2), and 1-bar CO annealed (S3) samples. This segregation trend is explained by the presence of oxygen species on the NP surface of the as prepared samples and the higher affinity of Ni to oxygen. Between 300°C and 500°C, Ni surface segregation continued to occur for the pristine vacuum-annealed sample (S1), while it ceased for the 25°C CO-exposed sample (S2). This is likely assigned to the negative heat of segregation of Ni dissolved in Pt and the preference of Ni to stay subsurface in the presence of CO. A drastic increase in the Ni/Pt ratio was observed when the sample was annealed at 400°C in the presence of 1-bar CO. This is explained based on a combination of the formation of a thick Ni-rich overlayer via the migration of volatile Ni(CO)x species from small to larger NPs as well as due to NP coarsening leading to a suppression of the Pt signal within the core of the larger NPs. After annealing at 500°C, strong interdiffusion, and Pt-Ni alloy formation are detected for all samples *via* the strong decrease in the Ni to Pt ratio measured.

Since the composition of the NP surface plays a pivotal role in the stability and reactivity of bimetallic nanoparticles, our findings are expected to be valuable for the optimization of the performance of nanocatalysts for reactions involving a CO environment.

CHAPTER 10: SUMMARY

In summary, this dissertation describes results that are of crucial importance in order to gain fundamental understanding on the parameters affecting catalytic activity and selectivity. Such knowledge is expected to be beneficial for the design of the next generation of nanocatalysts. Two synthesis methods have been used for the fabrication of NPs, namely inverse micelle encapsulation for single metal NPs and the surfactant-free solvothermal synthesis of PtNi bimetallic NPs. A number of experimental techniques including AFM, XPS, STM, TEM and XAFS were used to obtain the information about the morphology, composition and chemical state of the supported NPs.

The effect of the oxidation state of Pt NPs supported on γ-Al_2O_3 on their reactivity and selectivity toward methanol partial and total oxidation was investigated. Reactivity tests revealed higher activity and lower onset reaction temperature for the pre-oxidized catalysts as compared to the pre-reduced catalysts. XANES and EXAFS measurements show that in both, pre-reduced and pre-oxidized catalysts, the catalysts are substantially oxidized under reaction conditions at 25 °C and become only partially reduced when the temperature is raised to 50 °C.

STM data were used to obtain information about the thermodynamically stable shapes of Pt and Pd NPs supported on $TiO_2(110)$. The majority of Pd NPs was found to adopt a truncated octahedron shape with a (111) interfacial facet after annealing in UHV at 1100 °C, while Pt NPs were found to adopt three type of shapes. The alignment of the NP's edges with the TiO_2 (110)-[001] atomic rows provide evidence for the epitaxial relation of the NPs with the support. The NP-support adhesion energy was calculated based on the STM data for Pt and Pd NPs. The adhesion energy was found to decrease with increasing NP height. Furthermore Pt NPs were found to have lower adhesion energy as compared to Pd NPs.

The evolution of the surface composition and the structure of shape-selected octahedron PtNi NPs was investigated under gaseous and electrochemical environments. In a gaseous environment the NPs were exposed to 1-bar of O_2, H_2 and CO. Regardless of the specific gaseous atmosphere, annealing in the gaseous environment at low temperature (T<200 °C) lead to the segregation of Ni atoms to the surface due to the presence of oxygen species in the *ex situ* prepared as prepared samples. In vacuum, Ni segregation continues up to 270 °C, while in H_2 the Ni segregation ceases as early as 200 °C. The difference between H_2 and vacuum is attributed to the earlier reduction of surface oxides under H_2 exposure. Annealing at temperatures higher than 460°C leads to the formation of a PtNi alloy and a decrease in the Ni to Pt ratio on the surface. The thermal treatment in oxygen lead to the continuous segregation of Ni atoms to the surface and the formation of thick NiO shell with a small PtNi alloy at the core of the NP.

AFM was used to study the stability and morphology of PtNi NPs in vacuum and under 1 bar of CO. Exposing the sample to 1 bar CO at room temperature leads to the higher resistance of the NPs against sintering under vacuum annealing, while annealing under 1 bar CO lead to a significant coarsening which is most likely due to formation of $Ni(CO)_4$ and their enhanced mobility on the TiO_2 support surface. XPS measurements revealed Ni surface segregation upon annealing in vacuum at low temperature (T<300 °C). Interestingly, between 300 °C to 500 °C for the sample pre-exposed to CO the Ni segregation to the surface is hindered due to the higher bonding energy of CO to Pt as compared to Ni. Annealing in 1-bar CO resulted in Ni surface segregation up to 400 °C until oxygen species were available on the surface while above 500 °C, the diffusion of Pt atoms to the surface and formation of Ni-Pt alloy is observed.

The evolution of the structure and composition of similar octahedral PtNi NPs under acidic and alkalotic electrolyte was investigated using TEM and HAADF-STEM. Electrochemical cycling in acidic electrolytes leads to the dissolution of Ni species from the NP surface, leading to a Pt-skeleton structure with a thick Pt shell and Pt-Ni core. On the other hand, electrochemical cycling under active oxygenates leads to a Nickel oxide surface.

In conclusion, this thesis describes how fundamental understanding on structure, chemical state, composition and reactivity correlations can be established based on a synergistic combination of state-of-the-art synthesis methods and experimental techniques.

CHAPTER 11: OUTLOOK AND CHALLENGES

The results from this dissertation may open some new areas of research where further additional experimental and theoretical challenges will need to be solved. One such challenge is to develop synthesis methods to have better control of the size and shape of NPs. Also further development of *in situ* and *operando* techniques is needed for the better understanding of the structural and chemical evolution of nanocatalysts under reaction conditions. In terms of theoretical calculations, due to the complexity of nanocatalyst systems, theoretical studies will need to be further expanded from those constrained to systems that might not be good models for industrial applications to more realistic ones. This can be implemented by modelling larger clusters and by meaningfully incorporating the support and its own complexity, as for example vacancy defects, or hydroxylation commonly present in real world catalytic applications.

As was shown in this thesis, for certain applications, oxidized surfaces and not metallic ones might be more active for a given catalytic process and therefore, another current challenge is the controlled synthesis of well-defined oxides in thin films and NPs and the precise characterization of their structure, stability and chemical state evolution *in situ* and under *operando* reaction conditions. Further theoretical investigation is needed to understand the kinetic of the reaction on the oxidized NPs and thin films and also to find which oxide structure and oxidation state would display the highest activity for a particular reaction. The way that lattice oxygen or other oxygen species on the surface would contribute to the reactions (i.e. in Mars-van-Krevelen processes) is another challenge that needs to be addressed.

To better understand NP/support interactions, synthesizing stable and well defined size- and shape-selected NPs will be needed in order to isolate the effect of support from other parameters.

Experimentally, further advancement is needed in developing *in situ* and *operando* techniques for investigating and quantifying the support effect and its evolution under harsh reaction conditions. For example, bulk averaging techniques could be complemented by local measurements to understand spatial variations in the sample morphology, NP structure and composition, giving a complete picture of the active catalyst. Critical will be to develop techniques that can specifically probe the cluster-support interface underneath a particle to gain further insight into phenomena such as strain and charge transfer effects, or to resolve bonds between the NP atoms and support atoms and distinguish these from NP-adsorbate bonds. Also, monitoring the evolution of the structure of the support-nanoparticle interface such as the creation of oxygen vacancies, the crystalline structure of the interface and possible formation of interfacial alloys are other challenges that will need new or more sensitive *operando* and *in situ* techniques to be resolved.

In terms of theory, advancements in computational methods are needed to model larger, complex, and disordered systems. Currently, computational cost might constrain studies to smaller cluster sizes and thin slab support models of only a few atomic layers, which may not be representative of the active catalyst. In addition, when periodic boundary conditions are used in *ab inito* methods to model clusters, interactions with other supercells must also be considered. Developing higher throughput theoretical techniques with the ability to consider the support as a bulk system, or to include realistic defect concentrations in the support, as well as allowing the investigation of larger cluster/support systems is a necessity which, in combination with experimental techniques, can provide insight to the most active sites of catalysts.

In the case of multi-metallic nanocatalyst, understanding the mechanism of segregation phenomena under reaction condition is another challenge that will require further future attention. Furthermore, the interaction of the support with multi-metallic alloyed nanoparticles also requires additional attention due to their extended industrial applications. The support and its interaction with the different metals may play an important role in alloying or segregation within these NPs, particularly in different reactive environmental conditions. Beyond the creation of compositionally and structurally well-defined nanostructures, these support-enhanced active sites must be accurately resolved. In terms of theory, predicting the mechanism of reactions on bimetallic nanocatalysts and the interaction of molecules with multi-metallic nanoparticles is another challenge. Also the ability to simulate the evolution of the nanocatalyst and the segregation phenomena at high temperature and under gaseous or liquid environment is another necessity to be addressed.

Finally, I hope that this thesis could be used to stimulate further experimental and theoretical studies, which should go hand in hand in order to be able to gain a complete picture of the mechanisms underlying the unusual activity and selectivity of nanoparticle catalysts as well as in order to be able to ultimately design the new generation of active nanocatalysts.

LIST OF REFERENCES

1. Roldan Cuenya, B.; Behafarid, F., Nanocatalysis: size- and shape-dependent chemisorption and catalytic reactivity. *Surf. Sci. Rep.* **2015,** *70*, 135-187.

2. Reske, R.; Mistry, H.; Behafarid, F.; Roldan Cuenya, B.; Strasser, P., Particle Size Effects in the Catalytic Electroreduction of CO_2 on Cu Nanoparticles. *J. Am. Chem. Soc.* **2014,** *136*, 6978-6986.

3. Bondzie, V. A.; Parker, S. C.; Campbell, C. T., Oxygen adsorption on well-defined gold particles on TiO_2 (110). *J. Vac. Sci. Technol. A* **1999,** *17*, 1717.

4. Shaikhutdinov, S. K.; Meyer, R.; Naschitzki, M.; Baumer, M.; Freund, H. J., Size and support effects for CO adsorption on gold model catalysts. *Catal. Lett.* **2003,** *86*, 211-219.

5. Ono, L. K.; Croy, J. R.; Heinrich, H.; Roldan Cuenya, B., Oxygen Chemisorption, Formation, and Thermal Stability of Pt Oxides on Pt Nanoparticles Supported on SiO_2/Si(001): Size Effects. *J. Phys. Chem. C* **2011,** *115*, 16856-16866.

6. Ono, L. K.; Roldan-Cuenya, B., Effect of interparticle interaction on the low temperature oxidation of CO over size-selected Au nanocatalysts supported on ultrathin TiC films. *Catal. Lett.* **2007,** *113*, 86-94.

7. Peter, M.; Flores Camacho, J. M.; Adamovski, S.; Ono, L. K.; Dostert, K.-H.; O'Brien, C. P.; Roldan Cuenya, B.; Schauermann, S.; Freund, H.-J., Trends in the Binding Strength of Surface Species on Nanoparticles: How Does the Adsorption Energy Scale with the Particle Size? *Angew. Chem. Int. Ed.* **2013,** *52*, 5175-5179.

8. Ahmadi, M.; Behafarid, F.; Holse, C.; Nielsen, J. H.; Roldan Cuenya, B., Shape-Selection of Thermodynamically Stabilized Colloidal Pd and Pt Nanoparticles Controlled via Support Effects. *J. Phys. Chem. C* **2015,** *119*, 29178-29185.

9. Wang, C.; Daimon, H.; Lee, Y.; Kim, J.; Sun, S., Synthesis of Monodisperse Pt Nanocubes and Their Enhanced Catalysis for Oxygen Reduction. *J. Am. Chem. Soc.* **2007,** *129*, 6974-6975.

10. Xu, Z.-N.; Sun, J.; Lin, C.-S.; Jiang, X.-M.; Chen, Q.-S.; Peng, S.-Y.; Wang, M.-S.; Guo, G.-C., High-Performance and Long-Lived Pd Nanocatalyst Directed by Shape Effect for CO Oxidative Coupling to Dimethyl Oxalate. *ACS Catalysis* **2013,** *3*, 118-122.

11. Tian, N.; Zhou, Z. Y.; Sun, S. G.; Ding, Y.; Wang, Z. L., Synthesis of Tetrahexahedral Platinum Nanocrystals with High-Index Facets and High Electro-Oxidation Activity. *Science* **2007,** *316*, 732-735.

12. Mostafa, S.; Behafarid, F.; Croy, J. R.; Ono, L. K.; Li, L.; Yang, J. C.; Frenkel, A. I.; Cuenya, B. R., Shape-Dependent Catalytic Properties of Pt Nanoparticles. *J. Am. Chem. Soc.* **2010,** *132*, 15714-15719.

13. Narayanan, R.; El-Sayed, M. A., Shape-Dependent Catalytic Activity of Platinum Nanoparticles in Colloidal Solution. *Nano. Lett.* **2004,** *4*, 1343-1348.

14. Behafarid, F.; Ono, L. K.; Mostafa, S.; Croy, J. R.; Shafai, G.; Hong, S.; Rahman, T. S.; Bare, S. R.; Roldan Cuenya, B., Electronic properties and charge transfer phenomena in Pt nanoparticles on γ-Al_2O_3: size, shape, support, and adsorbate effects. *Phys. Chem. Chem. Phys.* **2012,** *14*, 11766.

15. Wendt, S.; Knapp, M.; Over, H., The Role of Weakly Bound On-Top Oxygen in the Catalytic CO Oxidation Reaction over RuO_2(110). *J. Am. Chem. Soc.* **2004,** *126*, 1537-1541.

16. Over, H., Atomic-Scale Structure and Catalytic Reactivity of the RuO_2 (110) Surface. *Science* **2000,** *287*, 1474-1476.

17. Hansen, T. W.; Wagner, J. B.; Hansen, P. L.; Dahl, S.; Topsoe, H.; Jacobsen, C. J. H., Atomic-resolution in situ transmission electron microscopy of a promoter of a heterogeneous catalyst. *Science* **2001,** *294*, 1508-1510.

18. Besenbacher, F.; Chorkendorff, I.; Clausen, B. S.; Hammer, B.; Molenbroek, A. M.; Norskov, J. K.; Stensgaard, I., Design of a surface alloy catalyst for steam reforming. *Science* **1998,** *279*, 1913-1915.

19. Gan, L.; Heggen, M.; O'Malley, R.; Theobald, B.; Strasser, P., Understanding and Controlling Nanoporosity Formation for Improving the Stability of Bimetallic Fuel Cell Catalysts. *Nano. Lett.* **2013,** *13*, 1131-1138.

20. Cui, C.; Gan, L.; Li, H.-H.; Yu, S.-H.; Heggen, M.; Strasser, P., Octahedral PtNi Nanoparticle Catalysts: Exceptional Oxygen Reduction Activity by Tuning the Alloy Particle Surface Composition. *Nano. Lett.* **2012,** *12*, 5885-5889.

21. Ono, L. K.; Sudfeld, D.; Roldan Cuenya, B., In-situ gas-phase catalytic properties of TiC-supported size-selected gold nanoparticles synthesized by diblock copolymer encapsulation Surf. *Surf. Sci.* **2006,** *600*, 5041.

22. Naitabdi, A.; Roldan Cuenya, B., Local investigation of the electronic properties of size-selected Au nanoparticles by scanning tunneling spectroscopy. *Appl. Phys. Lett.* **2006,** *89*, 043101.

23. Ono, L. K.; Roldan Cuenya, B., Effect of interparticle interactions on the low temperature oxidation of CO over size-selected Au nanocatalysts supported on ultrathin TiC films. *Catal. Lett.* **2007,** *113*, 86.

24. Ono, L. K.; Roldan Cuenya, B., Formation and Thermal Stability of Au_2O_3 on Size-Selected Gold Nanoparticles: Size and Support Effects. *J. Phys. Chem. C* **2008,** *112*, 4676.

25. Ono, L. K.; Roldan Cuenya, B., Size Effects on the Desorption of O_2 from Au_2O_3/Au^0 Nanoparticles Supported on SiO_2: a TPD Study. *J. Phys. Chem. C* **2008,** *112*, 18543.

26. Naitabdi, A.; Roldan Cuenya, B., Formation, Thermal Stability and Surface Composition of Size-Selected AuFe Nanoparticles. *Appl. Phys. Lett.* **2007,** *91*, 113110.

27. Croy, J. R.; Mostafa, S.; Liu, J.; Sohn, Y.; Heinrich, H.; Roldan Cuenya, B., Support Dependence of MeOH Decomposition Over Size-Selected Pt Nanoparticles. *Catal. Lett.* **2007,** *119*, 209.

28. Croy, J. R.; Mostafa, S.; Liu, J.; Sohn, Y.; Roldan Cuenya, B., Size dependent study of MeOH decomposition over size-selected Pt nanoparticles synthesized via micelle encapsulation. *Catal. Lett.* **2007,** *118*, 1.

29. Croy, J. R.; Mostafa, S.; Hickman, L.; Heinrich, H.; Roldan Cuenya, B., Bimetallic Pt/Metal catalysts for the decomposition of methanol: Effect of secondary metal on the oxidation state, activity, and selectivity of Pt. *Appl. Catal. A* **2008,** *350*, 207.

30. Haruta, M., Size- and Support-Dependency in the Catalysis of Gold. *Catal. Today* **1997,** *36*, 153.

31. Viswanath, B.; Kundu, P.; HaIder, A.; Ravishankar, N., Mechanistic Aspects of Shape Selection and Symmetry Breaking during Nanostructure Growth by Wet Chemical Methods. *J. Phys. Chem. C* **2009,** *113*, 16866-16883.

32. Xia, Y.; Xiong, Y. J.; Lim, B.; Skrabalak, S. E., Shape-Controlled Synthesis of Metal Nanocrystals: Simple Chemistry Meets Complex Physics? *Angew. Chem. Int. Ed.* **2009,** *48*, 60-103.

33. Mostafa, S.; Behafarid, F.; Croy, J. R.; Ono, L. K.; Li, L.; Yang, J. C.; Frenkel, A. I.; Roldan Cuenya, B., Shape-dependent Catalytic Properties of Pt Nanoparticles. *J. Am. Chem. Soc.* **2010,** *132*, 15714-15719.

34. Roldan Cuenya, B.; Croy, J. R.; Mostafa, S.; Behafarid, F.; Wang, Q.; Frenkel, A. I., Solving the structure of size-selected Pt nanocatalysts synthesized by inverse micelle encapsulation. *J. Am. Chem. Soc.* **2010,** *132*, 8747.

35. Behafarid, F.; Roldan Cuenya, B., Nanoepitaxy Using Micellar Nanoparticles. *Nano Lett.* **2011**, *in press*.

36. Lefferts, L.; van Ommen, J. G.; Ross, J. R. H., The Oxidative Dehydrogenation of Methanol to Formaldehyde Over Silver Catalysts in Relation to the Oxygen-Silver Interaction. *Appl. Catal.* **1986,** *23*, 385-402.

37. Nagy, A.; Mestl, G., High temperature partial oxidation reactions over silver catalysts. *Appl. Catal. A* **1999,** *188*, 337-353.

38. Guerreiro, E. D.; Gorriz, O. F.; Larsen, G.; Arrúa, L. A., Cu/SiO_2 catalysts for methanol to methyl formate dehydrogenation: A comparative study using different preparation techniques. *Appl. Catal. A* **2000,** *204*, 33-48.

39. Wittstock, a.; Zielasek, V.; Biener, J.; Friend, C. M.; Bäumer, M., Nanoporous gold catalysts for selective gas-phase oxidative coupling of methanol at low temperature. *Science* **2010,** *327*, 319-322.

40. Spivey, J. J., Complete catalytic oxidation of volatile organics. *Ind. Eng. Chem. Res.* **1987,** *26*, 2165-2180.

41. Sharma, R. K.; Zhou, B.; Tong, S.; Chuane, K. T.; Tg, A., Catalytic Destruction of Volatile Organic Compounds Using Supported Platinum and Palladium Hydrophobic Catalysts. *Ind. Eng. Chem. Res.* **1995,** *34*, 4310-4317.

42. Gandhi, H. S.; Graham, G. W.; McCabe, R. W., Automotive exhaust catalysis. *J. Catal.* **2003,** *216*, 433-442.

43. Tatibouët, J. M., Methanol oxidation as a catalytic surface probe. *Appl. Catal. A* **1997,** *148*, 213-252.

44. Iwasita, T., Electrocatalysis of methanol oxidation. *Electrochim. Acta* **2002,** *47*, 3663-3674.

45. Lamy, C.; Lima, A.; LeRhun, V.; Delime, F.; Coutanceau, C.; Léger, J.-M., Recent advances in the development of direct alcohol fuel cells (DAFC). *J. Power Sources* **2002,** *105*.

46. Mallat, T.; Baiker, A., Oxidation of alcohols with molecular oxygen on solid catalysts. *Chem. Rev.* **2004,** *104*, 3037-3058.

47. Markusse, A. P.; Kuster, B. F. M.; Koningsberger, D.; Marin, G. B., Platinum deactivation: in situ EXAFS during aqueous alcohol oxidation reaction. *Catal. Lett.* **1998,** *55*, 141-145.

48. Nicoletti, J. W.; Whitesides, G. M., Liquid-Phase Oxidation of 2-Propanol to Acetone by Dioxygen Using Supported Platinum

Cataiysts. *J. Phys. Chem.* **1989,** *93*, 759.

49. Ackermann, M. D.; Pedersen, T. M.; Hendriksen, B. L. M.; Robach, O.; Bobaru, S. C.; Popa, I.; Quiros, C.; Kim, H.; Hammer, B.; Ferrer, S.; Frenken, J. W. M., Structure and Reactivity of Surface Oxides on Pt(110) during Catalytic CO Oxidation. *Phys. Rev. Lett.* **2005,** *95*, 255505.

50. Hendriksen, B. L. M.; Frenken, J. W. M., CO Oxidation on Pt(110): Scanning Tunneling Microscopy Inside a High-Pressure Flow Reactor. *Phys. Rev. Lett.* **2002,** *89*, 2-5.

51. Li, W.-X., Oxidation of platinum surfaces and

reaction with carbon monoxide. *J. Phys. Condens. Matt.* **2008,** *20*, 184022.

52. Mallens, E. P. J.; Hoebink, J. H. B. J.; Marin, G. B., An investigation of the reaction mechanisms for the partial oxidation of methane to synthesis gas over platinum. *Catal. Lett.* **1995,** *33*, 291.

53. Gao, F.; Wang, Y.; Cai, Y.; Goodman, D. W., CO Oxidation on Pt-Group Metals from Ultrahigh Vacuum to Near Atmospheric Pressures. 2. Palladium and Platinum. *J. Phys. Chem. C* **2009,** *113*, 174-181.

54. McClure, S. M.; Goodman, D. W., New insights into catalytic CO oxidation on Pt-group metals at elevated pressures. *Chem. Phys. Lett.* **2009,** *469*, 1-13.

55. Alayon, E. M. C.; Singh, J.; Nachtegaal, M.; Harfouche, M.; van Bokhoven, J. A., On highly active partially oxidized platinum in carbon monoxide oxidation over supported platinum catalysts. *J. Catal.* **2009,** *263*, 228-238.

56. Singh, J.; van Bokhoven, J. A., Structure of alumina supported platinum catalysts of different particle size during CO oxidation using in situ IR and HERFD XAS. *Catal. Today* **2010,** *155*, 199-205.

57. Croy, J. R.; Mostafa, S.; Heinrich, H.; Roldan Cuenya, B., Size-selected Pt Nanoparticles Synthesized via Micelle Encapsulation: Effect of Pretreatment and Oxidation State on the Activity for Methanol Decomposition and Oxidation. *Catal. Lett.* **2009,** *131*, 21-32.

58. Paredis, K.; Ono, L. K.; Behafarid, F.; Zhang, Z.; Yang, J. C.; Frenkel, A. I.; Roldan Cuenya, B., Evolution of the structure and chemical state of Pd nanoparticles during the in situ catalytic reduction of NO with H_2. *J. Am. Chem. Soc.* **2011,** *133*, 13455.

59. Singh, J.; Nachtegaal, M.; Alayon, E. M. C.; Stotzel, J.; van Bokhoven, J. A., Dynamic Structure Changes of a Heterogeneous Catalyst within a Reactor: Oscillations in CO Oxidation over a Supported Platinum Catalyst. *Chemcatchem* **2010,** *2*, 653-657.

60. Roldan Cuenya, B., Synthesis and catalytic properties of metal nanoparticles: Size, shape, support, composition, and oxidation state effects. *Thin Solid Films* **2010,** *518*, 3127-3150.

61. Matos, J.; Ono, L. K.; Behafarid, F.; Croy, J. R.; Mostafa, S.; DeLaRiva, A. T.; Datye, A. K.; Frenkel, A. I.; Roldan Cuenya, B., In situ coarsening study of inverse micelle prepared Pt nanoparticles supported on γ-Al_2O_3: pretreatment and environmental effects. *Phys. Chem. Chem. Phys.* **2012,** *14*, 11457-11467.

62. Ravel, B.; Newville, M., *J. Synchrotron Rad.* **2005,** *12*, 537.

63. Rehr, J. J.; Albers, R. C., Theoretical approaches to x-ray absorption fine structure. *Rev. Mod. Phys.* **2000,** *72*, 621-654.

64. Ankudinov, A. L.; Bouldin, C. E.; Rehr, J. J.; Sims, J.; Hung, H., Parallel calculation of electron multiple scattering using Lanczos algorithms. *Phys Rev B* **2002,** *65*, 104107

65. Croy, J. R.; Mostafa, S.; Liu, J.; Sohn, Y.-h.; Roldan Cuenya, B., Size Dependent Study of MeOH Decomposition Over Size-selected Pt Nanoparticles Synthesized via Micelle Encapsulation. *Catal. Lett.* **2007,** *118*, 1-7.

66. Kästle, G.; Boyen, H.-G.; Weigl, F.; Lengl, G.; Herzog, T.; Ziemann, P.; Riethmüller, S.; Mayer, O.; Hartmann, C.; Spatz, J. P.; Möller, M.; Ozawa, M.; Banhart, F.; Garnier, M. G.; Oelhafen, P., Micellar Nanoreactors—Preparation and Characterization of Hexagonally Ordered Arrays of Metallic Nanodots. *Adv. Func. Mater.* **2003,** *13*, 853-861.

67. Roldan Cuenya, B.; Baeck, S.-H.; Jaramillo, T. F.; McFarland, E. W., Size- and support-dependent electronic and catalytic properties of Au^0/Au^{3+} nanoparticles synthesized from block copolymer micelles. *J. Am. Chem. Soc.* **2003,** *125*, 12928-12934.

68. Damyanova, S.; Bueno, J. M. C., Effect of CeO_2 loading on the surface and catalytic behaviors of CeO_2-$Al2O_3$-supported Pt catalysts. *Appl. Catal. A:Gen* **2003,** *253*, 135-150.

69. Roldan Cuenya, B.; Croy, J. R.; Mostafa, S.; Behafarid, F.; Li, L.; Zhang, Z.; Yang, J. C.; Wang, Q.; Frenkel, A. I., Solving the structure of size-selected Pt nanocatalysts synthesized by inverse micelle encapsulation. *J. Am. Chem. Soc.* **2010,** *132*, 8747-8756.

70. Mansour, A. N.; Sayers, D. E.; Cook, J. W.; Short, D. R.; Shannon, R. D.; Katzer, J. R., X-ray Absorption Studies of Some Platinum Oxides. *J. Phys. Chem.* **1984,** *88*, 1778-1781.

71. Friebel, D.; Miller, D. J.; O'Grady, C. P.; Anniyev, T.; Bargar, J.; Bergmann, U.; Ogasawara, H.; Wikfeldt, K. T.; Pettersson, L. G. M.; Nilsson, A., In situ X-ray probing reveals fingerprints of surface platinum oxide. *Phys. Chem. Chem. Phys.* **2011,** *13*, 262-266.

72. Merte, L. R.; Behafarid, F.; Miller, D. J.; Friebel, D.; Cho, S.; Mbuga, F.; Sokaras, D.; Alonso-Mori, R.; Weng, T.-C.; Nordlund, D.; Nilsson, A.; Roldan Cuenya, B., Electrochemical oxidation of size-selected Pt nanoparticles studied using in situ high-energy-resolution x-ray absorption spectroscopy. *ACS Catal.* **2012,** *2*, 2371-2376.

73. Behafarid, F.; Ono, L. K.; Mostafa, S.; Croy, J. R.; Shafai, G.; Hong, S.; Rahman, T. S.; Bare, S.; Roldan Cuenya, B., Electronic properties and charge transfer phenomena in Pt Nanoparticles on γ-Al_2O_3: Size, Shape, Support, and Adsorbate Effects. *Phys. Chem. Chem. Phys.* **2012,** *14*, 11766-11779.

74. Lei, Y.; Jelic, J.; Nitsche, L. C.; Meyer, R.; Miller, J., Effect of Particle Size and Adsorbates on the L_3, L_2 and L_1 X-ray Absorption Near Edge Structure of Supported Pt Nanoparticles. *Top. Catal.* **2011,** *54*, 334-348.

75. Frenkel, A. I.; Yevick, A.; Cooper, C.; Vasic, R., Modeling the structure and composition of nanoparticles by extended X-ray absorption fine-structure spectroscopy. *Annu. Rev. Anal. Chem.* **2011,** *4*, 23-39.

76. Jentys, A., Estimation of mean size and shape of small metal particles by EXAFS. *Phys. Chem. Chem. Phys.* **1999,** *1*, 4059-4063.

77. Koningsberger, D. C.; Gates, B. C., Nature of the metal-support interface in supported metal catalysts: Results from X-ray absorption spectroscopy. *Catal. Lett.* **1992,** *14*, 271-277.

78. Vaarkamp, M.; Miller, J. T.; Modica, F. S.; Koningsberger, D. C., On the Relation between Particle Morphology, Structure of the Metal-Support Interface, and Catalytic Properties of Pt/γ-Al_2O_3. *J. Catal.* **1996,** *163*, 294-305.

79. Zhang, Y.; Toebes, M. L.; van der Eerden, A.; O'Grady, W. E.; de Jong, K. P.; Koningsberger, D. C., Metal Particle Size and Structure of the Metal−Support Interface of Carbon-Supported Platinum Catalysts as Determined with EXAFS Spectroscopy. *J. Phys. Chem. B* **2004,** *108*, 18509-18519.

80. Mager-Maury, C.; Bonnard, G.; Chizallet, C.; Sautet, P.; Raybaud, P., H_2-lnduced Reconstruction of Supported Pt Clusters: Metal-Support Interaction versus Surface Hydride. *Chemcatchem* **2012,** *3*, 200-207.

81. McCabe, R. W.; McCready, D. F., Kinetics and reaction pathways of methanol oxidation on platinum. *J. Phys. Chem.* **1986,** *90*, 1428-1435.

82. Safonova, O. V.; Tromp, M.; van Bokhoven, J. A.; de Groot, F. M. F.; Evans, J.; Glatzel, P., Identification of CO adsorption sites in supported Pt catalysts using high-energy-resolution fluorescence detection X-ray spectroscopy. *J. Phys. Chem. B* **2006,** *110*, 16162-16164.

83. Chantaravitoon, P.; Chavadej, S.; Schwank, J., Temperature-programmed desorption of methanol and oxidation of methanol on Pt–Sn/Al_2O_3 catalysts. *Chem. Eng. J.* **2004,** *97*, 161-171.

84. McCabe, R. W.; Mitchell, P. J., Exhaust-catalyst development for methanol-fueled vehicles::: 1. A comparative study of methanol oxidation over alumina-supported catalysts containing group 9, 10,. *Appl. Catal.* **1986,** *27*, 83-98.

85. Gentry, J.; Jones, A.; Walsh, T.; Sheffield, S., Kinetics of Methanol Oxidation Over Platinum Wire Catalysts. *J. Chem. Soc. Faraday Trans.* **1980,** *76*, 2084-2095.

86. Lichtenberger, J.; Lee, D.; Iglesia, E., Catalytic oxidation of methanol on Pd metal and oxide clusters at near-ambient temperatures. *Phys. Chem. Chem. Phys.* **2007,** *9*, 4902-6.

87. Brewer, T. F.; Abraham, M. A.; Silver, R. G., Mixture Effects and Methanol Oxidation Kinetics over a Palladium Monolith Catalyst. *Ind. Eng. Chem. Res.* **1994,** *33*, 526-533.

88. Chou, P.; Vannice, M. A., Calorimetric Heat of Adsorption Measurements on Palladium .3. Influence of Crystallite Size and Support on O_2 Adsorption. *J. Catal.* **1987,** *105*, 342-351.

89. Xu, Y.; Shelton, W. A.; Schneider, W. F., Effect of Particle Size on the Oxidizability of Platinum Clusters. *J. Phys. Chem. A* **2006,** *110*, 5839-5846.

90. Mars, P.; van Krevelen, D. W., Oxidations carried out by means of vanadium oxide catalysts. *Chem. Eng. Sci.* **1954,** *3*, 41-59.

91. Hendriksen, B. L. M.; Ackermann, M. D.; van Rijn, R.; Stoltz, D.; Popa, I.; Balmes, O.; Resta, A.; Wermeille, D.; Felici, R.; Ferrer, S.; Frenken, J. W. M., The role of steps in surface catalysis and reaction oscillations. *Nat. Chem.* **2010,** *2*, 730-734.

92. Endo, M.; Matsumoto, T.; Kubota, J.; Domen, K.; Hirose, C., Oxidation of methanol by molecularly adsorbed oxygen on Pt(111) under vacuum and ambient pressure conditions studied by infrared reflection absorption spectroscopy: identification of formate intermediate. *Surf. Sci.* **1999,** *441*, L931-L937.

93. Gong, X.-Q.; Liu, Z.-P.; Raval, R.; Hu, P., A Systematic Study of CO Oxidation on Metals and Metal Oxides: Density Functional Theory Calculations. *J. Am. Chem. Soc.* **2004,** *126*, 8-9.

94. Reuter, K.; Frenkel, D.; Scheffler, M., The Steady State of Heterogeneous Catalysis, Studied by First-Principles Statistical Mechanics. *Phys. Rev. Lett.* **2004,** *93*.

95. Lashina, E. A.; Slavinskaya, E. M.; Chumakova, N. A.; Stonkus, O. A.; Gulyaev, R. V.; Stadnichenko, A. I.; Chumakov, G. A.; Boronin, A. I.; Demidenko, G. V., Self-sustained oscillations in CO oxidation reaction on PdO/Al_2O_3 catalyst. *Chem. Eng. Sci.* **2012,** *83*, 149-158.

96. Jensen, R.; Andersen, T.; Nierhoff, A.; Pedersen, T.; Hansen, O.; Dahl, S.; Chorkendorff, I., Self-sustained carbon monoxide oxidation oscillations on size-selected platinum nanoparticles at atmospheric pressure. *Phys. Chem. Chem. Phys.* **2013,** *15*, 2698.

97. Schwartz, W. R.; Pfefferle, L. D., Combustion of Methane over Palladium-Based Catalysts: Support Interactions. *J. Phys. Chem. C* **2012,** *116*, 8571-8578.

98. Müller, C. A.; Maciejewski, M.; Koeppel, R. A.; Tschan, R.; Baiker, A., Role of Lattice Oxygen in the Combustion of Methane over PdO/ZrO_2: Combined Pulse TG/DTA and MS Study with ^{18}O-Labeled Catalyst. *J. Phys. Chem.* **1996,** *100*, 20006-20014.

99. Seriani, N.; Pompe, W.; Ciacchi, L. C., Catalytic oxidation activity of Pt_3O_4 surfaces and thin films. *J. Phys. Chem. B* **2006,** *110*, 14860-9.

100. Li, N.-H.; Sun, S.-G.; Chen, S.-P., Studies on the role of oxidation states of the platinum surface in electrocatalytic oxidation of small primary alcohols. *J. Electroanal. Chem.* **1997,** *430*, 57-67.

101. Hellman, A.; Resta, A.; Martin, N. M.; Gustafson, J.; Trinchero, A.; Carlsson, P. A.; Balmes, O.; Felici, R.; van Rijn, R.; Frenken, J. W. M.; Andersen, J. N.; Lundgren, E.; Grönbeck, H., The Active Phase of Palladium during Methane Oxidation. *J. Phys. Chem. Lett.* **2012,** *3*, 678-682.

102. Behrens, M.; Studt, F.; Kasatkin, I.; Kuhl, S.; Havecker, M.; Abild-Pedersen, F.; Zander, S.; Girgsdies, F.; Kurr, P.; Kniep, B. L.; Tovar, M.; Fischer, R. W.; Norskov, J. K.; Schlogl, R.,

The Active Site of Methanol Synthesis over Cu/ZnO/Al_2O_3 Industrial Catalysts. *Science* **2012,** *336*, 893-897.

103. Kaden, W. E.; Wu, T.; Kunkel, W. A.; Anderson, S. L., Electronic Structure Controls Reactivity of Size-Selected Pd Clusters Adsorbed on TiO_2 Surfaces. *Science* **2009,** *326*, 826-829.

104. Mostafa, S.; Behafarid, F.; Croy, J. R.; Ono, L. K.; Li, L.; Yang, J. C.; Frenkel, A. I.; Roldan Cuenya, B., Shape-dependent Catalytic Properties of Pt Nanoparticles. *J. Am. Chem. Soc.* **2010,** *132*, 15714-15719.

105. Silly, F.; Castell, M. R., Selecting the shape of supported metal nanocrystals: Pd huts, hexagons, or pyramids on $SrTiO_3$(001). *Phys. Rev. Lett.* **2005,** *94*.

106. Behafarid, F.; Ono, L. K.; Mostafa, S.; Croy, J. R.; Shafai, G.; Hong, S.; Rahman, T. S.; Bare, S. R.; Cuenya, B. R., Electronic properties and charge transfer phenomena in Pt nanoparticles on gamma-Al_2O_3: size, shape, support, and adsorbate effects. *Phys. Chem. Chem. Phys.* **2012,** *14*, 11766-11779.

107. Farmer, J. A.; Campbell, C. T., Ceria Maintains Smaller Metal Catalyst Particles by Strong Metal-Support Bonding. *Science* **2010,** *329*, 933-936.

108. Iddir, H.; Komanicky, V.; Ogut, S.; You, H.; Zapol, P., Shape of platinum nanoparticles supported on $SrTiO_3$: Experiment and theory. *J. Phys. Chem. C.* **2007,** *111*, 14782-14789.

109. Chapon, C.; Granjeaud, S.; Humbert, A.; Henry, C. R., Structure and morphology of nanometer-sized Pd clusters grown at high temperature on natural graphite single crystals. *Eur Phys J-Appl Phys* **2001,** *13*, 23-30.

110. Chow, T. S., Size-dependent adhesion of nanoparticles on rough substrates. *J Phys-Condens Mat* **2003,** *15*, L83-L87.

111. Fu, Q.; Wagner, T.; Olliges, S.; Carstanjen, H. D., Metal-oxide interfacial reactions: Encapsulation of Pd on TiO_2 (110). *J Phys Chem B* **2005,** *109*, 944-951.

112. Graoui, H.; Giorgio, S.; Henry, C. R., Effect of the interface structure on the high-temperature morphology of supported metal clusters. *Philos Mag B* **2001,** *81*, 1649-1658.

113. Campbell, C. T., The Energetics of Supported Metal Nanoparticles: Relationships to Sintering Rates and Catalytic Activity. *Acc. Chem. Res.* **2013,** *46*, 1712-1719.

114. Bogicevic, A.; Jennison, D. R., Variations in the nature of metal adsorption on ultrathin Al_2O_3 films. *Phys. Rev. Lett.* **1999,** *82*, 4050-4053.

115. Henry, C. R., Morphology of supported nanoparticles. *Prog Surf Sci* **2005,** *80*, 92-116.

116. Campbell, C. T.; Starr, D. E., Metal adsorption and adhesion energies on MgO(100). *J. Am. Chem. Soc.* **2002,** *124*, 9212-9218.

117. Renaud, G.; Lazzari, R.; Revenant, C.; Barbier, A.; Noblet, M.; Ulrich, O.; Leroy, F.; Jupille, J.; Borensztein, Y.; Henry, C. R.; Deville, J. P.; Scheurer, F.; Mane-Mane, J.; Fruchart, O., Real-time monitoring of growing nanoparticles. *Science* **2003,** *300*, 1416-1419.

118. Nolte, P.; Stierle, A.; Jin-Phillipp, N. Y.; Kasper, N.; Schulli, T. U.; Dosch, H., Shape changes of supported Rh nanoparticles during oxidation and reduction cycles. *Science* **2008,** *321*, 1654-1658.

119. Steinruck, H. P.; Pesty, F.; Zhang, L.; Madey, T. E., Ultrathin Films of Pt on $TiO_2(110)$ - Growth and Chemisorption-Induced Surfactant Effects. *Phys. Rev. B.* **1995,** *51*, 2427-2439.

120. Kaden, W. E.; Kunkel, W. A.; Kane, M. D.; Roberts, F. S.; Anderson, S. L., Size-Dependent Oxygen Activation Efficiency over $Pdn/TiO_2(110)$ for the CO Oxidation Reaction. *J. Am. Chem. Soc.* **2010,** *132*, 13097-13099.

121. Kaden, W. E.; Wu, T. P.; Kunkel, W. A.; Anderson, S. L., Electronic Structure Controls Reactivity of Size-Selected Pd Clusters Adsorbed on TiO_2 Surfaces. *Science* **2009,** *326*, 826-829.

122. Suzuki, T.; Souda, R., The encapsulation of Pd by the supporting $TiO_2(110)$ surface induced by strong metal-support interactions. *Surf. Sci.* **2000,** *448*, 33-39.

123. Qin, Z. H.; Lewandowski, M.; Sun, Y. N.; Shaikhutdinov, S.; Freund, H. J., Encapsulation of Pt nanoparticles as a result of strong metal-support interaction with Fe_3O_4 (111). *J. Phys. Chem. C.* **2008,** *112*, 10209-10213.

124. Ferrero, S.; Piednoir, A.; Henry, C. R., Atomic Scale Imaging by UHV-AFM of Nanosized Gold Particles on Mica. *Nano. Lett.* **2001,** *1*, 227-230.

125. Zhang, Z.; Li, L.; Yang, J. C., Adhesion of Pt Nanoparticles Supported on γ-Al_2O_3 Single Crystal. *J. Phys. Chem. C* **2013,** *117*, 21407-21412.

126. Enterkin, J. A.; Poeppelmeier, K. R.; Marks, L. D., Oriented Catalytic Platinum Nanoparticles on High Surface Area Strontium Titanate Nanocuboids. *Nano. Lett.* **2011,** *11*, 993-997.

127. Hansen, K. H.; Worren, T.; Stempel, S.; Laegsgaard, E.; Baumer, M.; Freund, H. J.; Besenbacher, F.; Stensgaard, I., Palladium nanocrystals on Al_2O_3: Structure and adhesion energy. *Phys. Rev. Lett.* **1999,** *83*, 4120-4123.

128. Sun, J.; Wu, C.; Silly, F.; Koós, A. A.; Dillon, F.; Grobert, N.; Castell, M. R., Controlled growth of Ni nanocrystals on $SrTiO_3$ and their application in the catalytic synthesis of carbon nanotubes. *Chem. Commun.* **2013,** *49*, 3748.

129. Dulub, O.; Hebenstreit, W.; Diebold, U., Imaging cluster surfaces with atomic resolution: The strong metal-support interaction state of Pt supported on $TiO_2(110)$. *Phys. Rev. Lett.* **2000,** *84*, 3646-3649.

130. Xu, C.; Lai, X.; Zajac, G. W.; Goodman, D. W., Scanning tunneling microscopy studies of the TiO_2(110) surface: Structure and the nucleation growth of Pd. *Phys. Rev. B.* **1997,** *56*, 13464-13482.

131. Bowker, M.; Stone, P.; Morrall, P.; Smith, R.; Bennett, R.; Perkins, N.; Kvon, R.; Pang, C.; Fourre, E.; Hall, M., Model catalyst studies of the strong metal-support interaction: Surface structure identified by STM on Pd nanoparticles on TiO_2(110). *J. Catal.* **2005,** *234*, 172-181.

132. Hansen, K. H.; Sljivancanin, Z.; Laegsgaard, E.; Besenbacher, F.; Stensgaard, I., Adsorption of O_2 and NO on Pd nanocrystals supported on Al_2O_3/NiAl(110): overlayer and edge structures. *Surf. Sci.* **2002,** *505*, 25-38.

133. Lawler, J. F.; Schad, R.; Jordan, S.; vanKempen, H., Structure of epitaxial Fe films on MgO(100). *J Magn Magn Mater* **1997,** *165*, 224-226.

134. Lopez-Salido, I.; Lim, D. C.; Dietsche, R.; Bertram, N.; Kim, Y. D., Electronic and Geometric Properties of Au Nanoparticles on Highly Ordered Pyrolytic Graphite (HOPG) Studied Using X-ray Photoelectron Spectroscopy (XPS) and Scanning Tunneling Microscopy (STM). *J. Phys. Chem. B* **2006,** *110*, 1128-1136.

135. Silly, F.; Castell, M. R., Growth of Ag icosahedral nanocrystals on a $SrTiO_3$(001) support. *Appl. Phys. Lett.* **2005,** *87*.

136. Silly, F.; Castell, M. R., Temperature-Dependent Stability of Supported Five-Fold Twinned Copper Nanocrystals. *ACS Nano* **2009,** *3*, 901-906.

137. Koslowski, B.; Notz, R.; Ziemann, P., Epitaxial growth of iridium on strontium-titanate (001) studied by in situ scanning tunneling microscopy. *Surf. Sci.* **2002,** *496*, 153-159.

138. Bowker, M.; Stone, P.; Bennett, R.; Perkins, N., CO adsorption on a Pd/TiO_2(110) model catalyst. *Surf. Sci.* **2002,** *497*, 155-165.

139. Pesty, F.; Steinruck, H. P.; Madey, T. E., Thermal-Stability of Pt Films on TiO_2(110) - Evidence for Encapsulation. *Surf. Sci.* **1995,** *339*, 83-95.

140. Spatz, J. P.; Mossmer, S.; Hartmann, C.; Moller, M.; Herzog, T.; Krieger, M.; Boyen, H. G.; Ziemann, P.; Kabius, B., Ordered deposition of inorganic clusters from micellar block copolymer films. *Langmuir* **2000,** *16*, 407-415.

141. Behafarid, F.; Cuenya, B. R., Nano Pinstripes: TiO_2 Nanostripe Formation by Nanoparticle-Mediated Pinning of Step Edges. *J. Phys. Chem. Lett.* **2012,** *3*, 608-612.

142. Humbert, A.; Dayez, M.; Granjeaud, S.; Ricci, P.; Chapon, C.; Henry, C. R., Ultrahigh-Vacuum and Air Observations of Pd Clusters Grown on Clean Graphite. *J Vac Sci Technol B* **1991,** *9*, 804-805.

143. Diebold, U.; Ruzycki, N.; Herman, G. S.; Selloni, A., One step towards bridging the materials gap: surface studies of TiO_2 anatase. *Catal Today* **2003,** *85*, 93-100.

144. Iddir, H.; Disko, M. M.; Ogut, S.; Browning, N. D., Atomic scale characterization of the Pt/TiO_2 interface. *Micron* **2005,** *36*, 233-241.

145. Campbell, C. T.; Sellers, J. R. V., Anchored metal nanoparticles: Effects of support and size on their energy, sintering resistance and reactivity. *Farad. Discuss.* **2013,** *162*, 9-30.

146. Min, B. K.; Wallace, W. T.; Goodman, D. W., Synthesis of a Sinter-Resistant, Mixed-Oxide Support for Au Nanoclusters†. *J. Phys. Chem. B* **2004,** *108*, 14609-14615.

147. Yim, C. M.; Pang, C. L.; Hermoso, D. R.; Dover, C. M.; Muryn, C. A.; Maccherozzi, F.; Dhesi, S. S.; Pérez, R.; Thornton, G., Influence of support morphology on the bonding of molecules to nanoparticles. *Proc. Natl. Acad. Sci.* **2015,** *112*, 7903-7908.

148. Sanchez, A.; Abbet, S.; Heiz, U.; Schneider, W. D.; Häkkinen, H.; Barnett, R. N.; Landman, U., When Gold Is Not Noble: Nanoscale Gold Catalysts. *J. Phys. Chem. A.* **1999,** *103*, 9573-9578.

149. Prins, R., Hydrogen Spillover. Facts and Fiction. *Chem. Rev.* **2012,** *112*, 2714-2738.

150. Behafarid, F.; Ono, L. K.; Mostafa, S.; Croy, J. R.; Shafai, G.; Hong, S.; Rahman, T. S.; Bare, S. R.; Roldan Cuenya, B., Electronic properties and charge transfer phenomena in Pt nanoparticles on gamma-Al_2O_3: size, shape, support, and adsorbate effects. *Phys. Chem. Chem. Phys.* **2012,** *14*, 11766-11779.

151. Merte, L. R.; Ahmadi, M.; Behafarid, F.; Ono, L. K.; Lira, E.; Matos, J.; Li, L.; Yang, J. C.; Roldan Cuenya, B., Correlating Catalytic Methanol Oxidation with the Structure and Oxidation State of Size-Selected Pt Nanoparticles. *ACS Catal.* **2013,** *3*, 1460-1468.

152. Diebold, U., The surface science of titanium dioxide. *Surf Sci Rep* **2003,** *48*, 53-229.

153. Caballero, A.; Holgado, J. P.; Gonzalez-delaCruz, V. M.; Habas, S. E.; Herranz, T.; Salmeron, M., In situ spectroscopic detection of SMSI effect in a Ni/CeO_2 system: hydrogen-induced burial and dig out of metallic nickel. *Chem. Commun.* **2010,** *46*, 1097-1099.

154. Bruix, A.; Rodriguez, J. A.; Ramírez, P. J.; Senanayake, S. D.; Evans, J.; Park, J. B.; Stacchiola, D.; Liu, P.; Hrbek, J.; Illas, F., A New Type of Strong Metal–Support Interaction and the Production of H_2 through the Transformation of Water on $Pt/CeO_2(111)$ and $Pt/CeO_x/TiO_2(110)$ Catalysts. *J. Am. Chem. Soc.* **2012,** *134*, 8968-8974.

155. Belzunegui, J. P.; Sanz, J.; Rojo, J. M., Contribution of Physical Blocking and Electronic Effect to Establishment of Strong Metal Support Interaction in Rh/TiO_2 Catalysts. *J. Am. Chem. Soc.* **1992,** *114*, 6749-6754.

156. Pesty, F.; Steinrück, H.-P.; Madey, T. E., Thermal stability of Pt films on TiO_2(110): evidence for encapsulation. *Surf. Sci* **1995,** *339*, 83-95.

157. Sekizawa, K.; Widjaja, H.; Maeda, S.; Ozawa, Y.; Eguchi, K., Low temperature oxidation of methane over Pd catalyst supported on metal oxides. *Catal. Today* **2000,** *59*, 69-74.

158. Boyen, H. G.; Herzog, T.; Kästle, G.; Weigl, F.; Ziemann, P.; Spatz, J. P.; Möller, M.; Wahrenberg, R.; Garnier, M. G.; Oelhafen, P., X-ray photoelectron spectroscopy study on gold nanoparticles supported on diamond. *Phys. Rev. B.* **2002,** *65*.

159. Polli, A. D.; Wagner, T.; Gemming, T.; Ruhle, M., Growth of platinum on TiO_2- and SrO-terminated $SrTiO_3$(100). *Surf. Sci* **2000,** *448*, 279-289.

160. Bliem, R.; Pavelec, J.; Gamba, O.; McDermott, E.; Wang, Z.; Gerhold, S.; Wagner, M.; Osiecki, J.; Schulte, K.; Schmid, M.; Blaha, P.; Diebold, U.; Parkinson, G. S., Adsorption and incorporation of transition metals at the magnetite Fe_3O_4(001) surface. *Phys. Rev. B.* **2015,** *92*.

161. Kibsgaard, J.; Clausen, B. S.; Topsøe, H.; Lægsgaard, E.; Lauritsen, J. V.; Besenbacher, F., Scanning tunneling microscopy studies of TiO_2-supported hydrotreating catalysts: Anisotropic particle shapes by edge-specific MoS_2–support bonding. *J. Catal.* **2009,** *263*, 98-103.

162. Takakusagi, S.; Fukui, K.; Tero, R.; Nariyuki, F.; Iwasawa, Y., Self-limiting growth of pt nanoparticles from MeCpPtMe3 adsorbed on TiO_2(110) studied by scanning tunneling microscopy. *Phys. Rev. Lett.* **2003,** *91*.

163. Bennett, R. A.; Pang, C. L.; Perkins, N.; Smith, R. D.; Morrall, P.; Kvon, R. I.; Bowker, M., Surface structures in the SMSI state; Pd on (1 x 2) reconstructed TiO_2(110). *J. Phys. Chem. B* **2002,** *106*, 4688-4696.

164. Ouyang, G.; Liang, L. H.; Wang, C. X.; Yang, G. W., Size-dependent interface energy. *Appl. Phys. Lett.* **2006,** *88*.

165. Muller, P.; Kern, R., Equilibrium shape of epitaxially strained crystals (Volmer-Weber case). *J Cryst Growth* **1998,** *193*, 257-270.

166. Xia, Y.; Xiong, Y.; Lim, B.; Skrabalak, S. E., Shape-Controlled Synthesis of Metal Nanocrystals: Simple Chemistry Meets Complex Physics? *Angew. Chem. Int. Ed.* **2009,** *48*, 60-103.

167. Ahmadi, T. S.; Wang, Z. L.; Green, T. C.; Henglein, A.; ElSayed, M. A., Shape-controlled synthesis of colloidal platinum nanoparticles. *Science* **1996,** *272*, 1924-1926.

168. Yang, Y.; Matsubara, S.; Xiong, L.; Hayakawa, T.; Nogami, M., Solvothermal Synthesis of Multiple Shapes of Silver Nanoparticles and Their SERS Properties. *J. Phys. Chem. C* **2007,** *111*, 9095-9104.

169. Jin, M.; Zhang, H.; Xie, Z.; Xia, Y., Palladium nanocrystals enclosed by {100} and {111} facets in controlled proportions and their catalytic activities for formic acid oxidation. *Energy Environ. Sci.* **2012,** *5*, 6352-6357.

170. Chen, X. M.; Wu, G. H.; Chen, J. M.; Chen, X.; Xie, Z. X.; Wang, X. R., Synthesis of "Clean" and Well-Dispersive Pd Nanoparticles with Excellent Electrocatalytic Property on Graphene Oxide. *J. Am. Chem. Soc.* **2011,** *133*, 3693-3695.

171. Li, Y.; Boone, E.; El-Sayed, M. A., Size Effects of PVP−Pd Nanoparticles on the Catalytic Suzuki Reactions in Aqueous Solution. *Langmuir* **2002,** *18*, 4921-4925.

172. Mistry, H.; Behafarid, F.; Zhou, E.; Ono, L. K.; Zhang, L.; Cuenya, B. R., Shape-Dependent Catalytic Oxidation of 2-Butanol over Pt Nanoparticles Supported on gamma-Al2O3. *ACS Catal.* **2014,** *4*, 109-115.

173. Ma, R.; Semagina, N., Nanoparticle Shape Effect Study as an Efficient Tool to Reveal the Structure Sensitivity of Olefinic Alcohol Hydrogenation. *J. Phys. Chem. C* **2010,** *114*, 15417-15423.

174. Xu, R.; Wang, D.; Zhang, J.; Li, Y., Shape-Dependent Catalytic Activity of Silver Nanoparticles for the Oxidation of Styrene. *Chem. Asian. J* **2006,** ***1***, 888-893.

175. Mittendorfer, F.; Seriani, N.; Dubay, O.; Kresse, G., Morphology of mesoscopic Rh and Pd nanoparticles under oxidizing conditions. *Phys Rev B* **2007,** *76*.

176. Cuenya, B. R.; Behafarid, F., Nanocatalysis: size- and shape-dependent chemisorption and catalytic reactivity. *Surf. Sci. Rep.* **2015,** *70*, 135-187.

177. Roldan Cuenya, B., Metal Nanoparticle Catalysts Beginning to Shape-up. *Acc. Chem. Res.* **2013,** ***46***, 1682-1691.

178. Cui, C.; Gan, L.; Heggen, M.; Rudi, S.; Strasser, P., Compositional segregation in shaped Pt alloy nanoparticles and their structural behaviour during electrocatalysis. *Nat. Mater.* **2013,** *12*, 765-771.

179. Methfessel, M.; Hennig, D.; Scheffler, M., Trends of the Surface Relaxations, Surface Energies, and Work-Functions of the 4d Transition-Metals. *Phys Rev B* **1992,** *46*, 4816-4829.

180. Ozkan, U. S.; Kumthekar, M. W.; Karakas, G., Characterization and temperature-programmed studies over Pd/TiO_2 catalysts for NO reduction with methane. *Catal. Today* **1998,** *40*, 3-14.

181. Farrauto, R. J.; Hobson, M. C.; Kennelly, T.; Waterman, E. M., Catalytic Chemistry of Supported Palladium for Combustion of Methane. *Appl Catal a-Gen* **1992,** *81*, 227-237.

182. Putna, E. S.; Vohs, J. M.; Gorte, R. J., Oxygen desorption from alpha-Al_2O_3(0001) supported Rh, Pt and Pd particles. *Surf. Sci* **1997,** *391*, L1178-L1182.

183. Peuckert, M., Xps Study on Surface and Bulk Palladium Oxide, Its Thermal-Stability, and a Comparison with Other Noble-Metal Oxides. *J. Phys. Chem* **1985,** *89*, 2481-2486.

184. Milun, M.; Pervan, P.; Wandelt, K., Interaction of Oxygen with a Polycrystalline Palladium Surface over a Wide Temperature-Range. *Surf. Sci* **1989,** *218*, 363-388.

185. Matthews, J. W., *Epitaxial Growth*. london, 1975; Vol. 2, p 680.

186. Brovko, O. O.; Bazhanov, D. I.; Meyerheim, H. L.; Sander, D.; Stepanyuk, V. S.; Kirschner, J., Effect of mesoscopic misfit on growth, morphology, electronic properties and magnetism of nanostructures at metallic surfaces. *Surf. Sci. Rep.* **2014,** *69*, 159-195.

187. Matthews, J. W.; Jackson, D. C.; Chambers, A., *Thin Solid Films*. 1975; Vol. 26.

188. Baumer, M.; Freund, H. J., Metal deposits on well-ordered oxide films. *Prog. Surf. Sci* **1999,** *61*, 127-198.

189. Vitos, L.; Ruban, A. V.; Skriver, H. L.; Kollar, J., The surface energy of metals. *Surf. Sci* **1998,** *411*, 186-202.

190. Li, J. G., Wetting and Interfacial Bonding of Metals with Ionocovalent Oxides. *J. Am. Ceram. Soc* **1992,** *75*, 3118-3126.

191. Muller, P.; Kern, R., Equilibrium nano-shape change induced by epitaxial stress: effect of surface stress. *Appl. Surf. Sci.* **2000,** *164*, 68-71.

192. Haruta, M., Low-Temperature Oxidation of CO over Gold Supported on TiO_2, α-Fe_2O_3, and Co_3O_4. *J. Catal.* **1993,** *144*, 175-192.

193. Williams, W. D.; Shekhar, M.; Lee, W.-S.; Kispersky, V.; Delgass, W. N.; Ribeiro, F. H.; Kim, S. M.; Stach, E. A.; Miller, J. T.; Allard, L. F., Metallic Corner Atoms in Gold Clusters Supported on Rutile Are the Dominant Active Site during Water−Gas Shift Catalysis. *J. Am. Chem. Soc.* **2010,** *132*, 14018-14020.

194. Cargnello, M.; Doan-Nguyen, V. V. T.; Gordon, T. R.; Diaz, R. E.; Stach, E. A.; Gorte, R. J.; Fornasiero, P.; Murray, C. B., Control of Metal Nanocrystal Size Reveals Metal-Support Interface Role for Ceria Catalysts. *Science* **2013,** *341*, 771-773.

195. Fedlheim, D. L.; Foss, C. A., *Metal Nanoparticles: Synthesis Characterization & Applications* CRC - Taylor Francis Group: London, 2001.

196. Schmid, G., *Nanoparticles: From Theory to Applications*. Wiley-VCH: New York, 2004.

197. Astruc, D., *Nanoparticles and Catalysis*. Wiley-VCH: New York, 2007.

198. Oezaslan, M.; Heggen, M.; Strasser, P., Size-Dependent Morphology of Dealloyed Bimetallic Catalysts: Linking the Nano to the Macro Scale. *J. Am. Chem. Soc.* **2012,** *134*, 514-524.

199. Coq, B.; Figueras, F., Structure-activity relationships in catalysis by metals: some aspects of particle size, bimetallic and supports effects. *Coordination Chemistry Reviews* **1998,** *178*, 1753-1783.

200. Bond, G. C., The Origins of Particle-Size Effects in Heterogeneous Catalysis. *Surf. Sci.* **1985,** *156*, 966-981.

201. Arai, M., Particle size effect and structure sensitivity in catalysis by supported metal catalysts. *J. Chem. Eng. Jpn.* **1997,** *30*, 1123-1125.

202. Gentsch, H.; Guillen, N.; Hartel, V.; Kopp, M., Problem of Particle-Size Effect in Heterogeneous Catalysis. *Berichte Der Bunsen-Gesellschaft-Physical Chemistry Chemical Physics* **1973,** *77*, 1023-1023.

203. Mukerjee, S., Reviews of Applied Electrochemistry .23. Particle-Size and Structural Effects in Platinum Electrocatalysis. *Journal of Applied Electrochemistry* **1990,** *20*, 537-548.

204. Eppell, S.; Chottiner, G. S.; Scherson, D. A., Particle-Size Effects in Electrocatalysis - a Surface Science Approach. *Abstracts of Papers of the American Chemical Society* **1989,** *197*, 103-COLL.

205. Lee, I.; Morales, R.; Albiter, M. A.; Zaera, F., Synthesis of heterogeneous catalysts with well shaped platinum particles to control reaction selectivity. *Proceedings of the National Academy of Sciences of the United States of America* **2008,** *105*, 15241-15246.

206. Linic, S.; Christopher, P., Overcoming Limitation in the Design of Selective Solid Catalysts by Manipulating Shape and Size of Catalytic Particles: Epoxidation Reactions on Silver. *Chemcatchem* **2010,** *2*, 1061-1063.

207. Kundu, S.; Liang, H., Shape-selective formation and characterization of catalytically active iridium nanoparticles. *J. Colloid. Inter. Sci.* **2011,** *354*, 597-606.

208. Roldan Cuenya, B.; Frenkel, A. I.; Mostafa, S.; Behafarid, F.; Croy, J. R.; Ono, L. K.; Wang, Q., Anomalous lattice dynamics and thermal properties of supported size- and shape-selected Pt nanoparticles. *Phys Rev B* **2010,** *82*, 155450

209. Ono, L. K.; Sudfeld, D.; Roldan Cuenya, B., In situ gas-phase catalytic properties of TiC-supported size-selected gold nanoparticles synthesized by diblock copolymer encapsulation. *Surf. Sci.* **2006,** *600*, 5041-5050.

210. Koper, M. T. M., Structure sensitivity and nanoscale effects in electrocatalysis. *Nanoscale* **2011,** *3*, 2054-2073.

211. Coutanceau, C.; Urchaga, P.; Brimaud, S.; Baranton, S., Colloidal Syntheses of Shape- and Size-Controlled Pt Nanoparticles for Electrocatalysis. *Electrocatal.* **2012,** *3*, 75-87.

212. Chen, Q.-S.; Vidal-Iglesias, F. J.; Solla-Gullón, J.; Sun, S.-G.; Feliu, J. M., Role of surface defect sites: from Pt model surfaces to shape-controlled nanoparticles. *Chem. Sci.* **2012,** *3*, 136.

213. Cheong, S. S.; Watt, J. D.; Tilley, R. D., Shape control of platinum and palladium nanoparticles for catalysis. *Nanoscale* **2010,** *2*, 2045-2053.

214. Chen, M.; Wu, B. H.; Yang, J.; Zheng, N. F., Small Adsorbate-Assisted Shape Control of Pd and Pt Nanocrystals. *Advanced Materials* **2012,** *24*, 862-879.

215. Tao, F.; Grass, M. E.; Zhang, Y.; Butcher, D. R.; Renzas, J. R.; Liu, Z.; Chung, J. Y.; Mun, B. S.; Salmeron, M.; Somorjai, G., Reaction-Drivaen Restructuring of Rh-Pd and Pt-Pd Core-Shell Nanoparticles. *Science* **2008,** *322*, 932-934.

216. Mayrhofer, K. J. J.; Juhart, V.; Hartl, K.; Hanzlik, M.; Arenz, M., Adsorbate-Induced Surface Segregation for Core-Shell Nanocatalysts. *Angew. Chem. Int. Ed.* **2009,** *48*, 3529-3531.

217. Andersson, K. J.; Calle-Vallejo, F.; Rossmeisl, J.; Chorkendorff, L., Adsorption-Driven Surface Segregation of the Less Reactive Alloy Component. *J. Am. Chem. Soc.* **2009,** *131*, 2404-2407.

218. Nerlov, J.; Chorkendorff, I., Promotion through gas phase induced surface segregation: methanol synthesis from CO, CO2 and H-2 over Ni/Cu(100). *Catal. Lett.* **1998,** *54*, 171-176.

219. Nerlov, J.; Chorkendorff, I., Methanol synthesis from CO_2, CO, and H_2 over Cu(100) and Ni/Cu(100). *J. Catal.* **1999,** *181*, 271-279.

220. Mu, R. T.; Fu, Q. A.; Xu, H.; Zhang, H. I.; Huang, Y. Y.; Jiang, Z.; Zhang, S. O.; Tan, D. L.; Bao, X. H., Synergetic Effect of Surface and Subsurface Ni Species at Pt-Ni Bimetallic Catalysts for CO Oxidation. *J. Am. Chem. Soc.* **2011,** *133*, 1978-1986.

221. Mu, R. T.; Guo, X. G.; Fu, Q.; Bao, X. H., Oscillation of Surface Structure and Reactivity of PtNi Bimetallic Catalysts with Redox Treatments at Variable Temperatures. *J. Phys. Chem. C* **2011,** *115*, 20590-20595.

222. Liu, K.; Wang, A. Q.; Zhang, T., Recent Advances in Preferential Oxidation of CO Reaction over Platinum Group Metal Catalysts. *ACS Catal.* **2012,** *2*, 1165-1178.

223. Wang, D.; Xin, H. L.; Hovden, R.; Wang, H.; Yu, Y.; Muller, D. A.; DiSalvo, F. J.; Abruña, H. D., Structurally ordered intermetallic platinum–cobalt core–shell nanoparticles with enhanced activity and stability as oxygen reduction electrocatalysts. *Nature Mater.* **2012**.

224. Wanjala, B. N.; Luo, J.; Loukrakpam, R.; Fang, B.; Mott, D.; Njoki, P. N.; Engelhard, M.; Naslund, H. R.; Wu, J. K.; Wang, L.; Malis, O.; Zhong, C.-J., Nanoscale Alloying, Phase-Segregation, and Core−Shell Evolution of Gold−Platinum Nanoparticles and Their Electrocatalytic Effect on Oxygen Reduction Reaction. *Chem. Mater.* **2010,** *22*, 4282-4294.

225. Alayoglu, S.; Nilekar, A. U.; Mavrikakis, M.; Eichhorn, B., Ru–Pt core–shell nanoparticles for preferential oxidation of carbon monoxide in hydrogen. *Nature Mater.* **2008,** *7*, 333-338.

226. Tao, F.; Grass, M. E.; Zhang, Y.; Butcher, D. R.; Renzas, J. R.; Liu, Z.; Chung, J. Y.; Mun, B. S.; Salmeron, M.; Somorjai, G. A., Reaction-Driven Restructuring of Rh-Pd and Pt-Pd Core-Shell Nanoparticles. *Science* **2008,** *322*, 932-934.

227. Ma, Y.; Balbuena, P. B., Pt surface segregation in bimetallic Pt3M alloys: A density functional theory study. *Surf. Sci.* **2008,** *602*, 107-113.

228. Wang, G. F.; Van Hove, M. A.; Ross, P. N.; Baskes, M. I., Quantitative prediction of surface segregation in bimetallic Pt-M alloy nanoparticles (M = Ni, Re, Mo). *Prog Surf Sci* **2005,** *79*, 28-45.

229. Stamenković, V.; Schmidt, T. J.; Ross, P. N.; Marković, N. M., Surface segregation effects in electrocatalysis: kinetics of oxygen reduction reaction on polycrystalline Pt3Ni alloy surfaces. *J. Electroanal. Chem.* **2003,** *554-555*, 191-199.

230. Deckers, S.; Habraken, F.; van der Weg, W.; Denier van der Gon, A.; Pluis, B.; van der Veen, J.; Baudoing, R., Segregation at the Pt0.5Ni0.5(111) surface studied by medium-energy ion scattering. *Phys Rev B* **1990,** *42*, 3253-3259.

231. Eymery, J.; Joud, J. C., Surface segregation in binary Cu-Ni and Pt-Ni alloys using Monte Carlo simulation. *Surf. Sci.* **1990,** *231*, 419-426.

232. Najafabadi, R.; Srolovitz, D. J., Order-Disorder Transitions at and Segregation to (001) Ni-Pt Surfaces. *Surf. Sci.* **1993,** *286*, 104-115.

233. Ruban, A. V.; Skriver, H. L.; Norskov, J. K., Surface segregation energies in transition-metal alloys. *Phys Rev B* **1999,** *59*, 15990-16000.

234. Wang, G.; Van Hove, M. A.; Ross, P. N.; Baskes, M. I., Monte Carlo simulations of segregation in Pt-Ni catalyst nanoparticles. *J. Chem. Phys.* **2005,** *122*, 024706.

235. Nilekar, A. U.; Ruban, A. V.; Mavrikakis, M., Surface segregation energies in low-index open surfaces of bimetallic transition metal alloys. *Surf. Sci.* **2009,** *603*, 91-96.

236. Su, C. W.; Ho, H. Y.; Shern, C. S.; Chen, R. H., Structure evolution of Ni ultrathin films on Pt(111). *Surf. Sci.* **2002,** *499*, 103-108.

237. Mu, R.; Fu, Q.; Liu, H.; Tan, D.; Zhai, R.; Bao, X., Reversible surface structural changes in Pt-based bimetallic nanoparticles during oxidation and reduction cycles. *Appl. Surf. Sci.* **2009,** *255*, 7296-7301.

238. Jacob, T.; Merinov, B. V.; Goddard, W. A., Chemisorption of atomic oxygen on Pt(111) and Pt/Ni(111) surfaces. *Chem. Phys. Lett.* **2004,** *385*, 374-377.

239. Menning, C. A.; Chen, J. G., Regenerating Pt–3d–Pt model electrocatalysts through oxidation–reduction cycles monitored at atmospheric pressure. *J. Power Sources* **2010,** *195*, 3140-3144.

240. Ma, Y.; Balbuena, P. B., Surface segregation in bimetallic Pt3M (M=Fe, Co, Ni) alloys with adsorbed oxygen. *Surf. Sci.* **2009,** *603*, 349-353.

241. Kitchin, J. R.; Nørskov, J. K.; Barteau, M. A.; Chen, J. G., Modification of the surface electronic and chemical properties of Pt(111) by subsurface 3d transition metals. *J. Chem. Phys.* **2004,** *120*, 10240.

242. Stamenkovic, V. R.; Fowler, B.; Mun, B. S.; Wang, G.; Ross, P. N.; Lucas, C. A.; Markovic, N. M., Improved Oxygen Reduction Activity on $Pt_3Ni(111)$ via Increased Surface Site Availability. *Science* **2007,** *315*, 493-497.

243. Wu, Y.; Cai, S.; Wang, D.; He, W.; Li, Y., Syntheses of Water-Soluble Octahedral, Truncated Octahedral, and Cubic Pt–Ni Nanocrystals and Their Structure–Activity Study in Model Hydrogenation Reactions. *J. Am. Chem. Soc.* **2012,** *134*, 8975-8981.

244. Boer, F. R.; Boom, R.; Mattens, W.; Miedema, A.; Niessen, A., *Cohesion in metals: transition metal alloys, Vol. 1*. Elsevier Science Publishers B.V: 1988.

245. Stamenković, V.; Schmidt, T. J.; Ross, P. N.; Marković, N. M., Surface Composition Effects in Electrocatalysis: Kinetics of Oxygen Reduction on Well-Defined Pt3Ni and Pt3Co Alloy Surfaces. *J. Phys. Chem. B* **2002,** *106*, 11970-11979.

246. Hasche, F.; Oezaslan, M.; Strasser, P., Activity, Structure and Degradation of Dealloyed PtNi3 Nanoparticle Electrocatalyst for the Oxygen Reduction Reaction in PEMFC. *J. Electrochem. Soc.* **2012,** *159*, B25-B34.

247. Hasche, F.; Oezaslan, M.; Strasser, P., In Situ Observation of the Thermally Induced Growth of Platinum-Nanoparticle Catalysts Using High-Temperature X-ray Diffraction. *Chemphyschem* **2012,** *13*, 828-834.

248. Hasché, F.; Oezaslan, M.; Strasser, P., Activity, Stability, and Degradation Mechanisms of Dealloyed PtCu3 and PtCo3 Nanoparticle Fuel Cell Catalysts. *Chemcatchem* **2011,** *3*, 1805-1813.

249. Cui, C.; Ahmadi, M.; Behafarid, F.; Gan, L.; Neumann, M.; Heggen, M.; Roldan Cuenya, B.; Strasser, P., Shape-Selected Bimetallic Nanoparticle Electrocatalysts: Evolution of Their Atomic-Scale Structure, Chemical Composition, and Electrochemical Reactivity under Various Chemical Environments. *Farad. Discuss.* **2013**, 91-112.

250. http://www.casaxps.com.

251. Kwon, S. G.; Hyeon, T., Formation Mechanisms of Uniform Nanocrystals via Hot-Injection and Heat-Up Methods. *Small* **2011,** *7*, 2685-2702.

252. Carpenter, M. K.; Moylan, T. E.; Kukreja, R. S.; Atwan, M. H.; Tessema, M. M., Solvothermal Synthesis of Platinum Alloy Nanoparticles for Oxygen Reduction Electrocatalysis. *J. Am. Chem. Soc.* **2012,** *134*, 8535-8542.

253. Sun, S. H.; Murray, C. B.; Weller, D.; Folks, L.; Moser, A., Monodisperse FePt nanoparticles and ferromagnetic FePt nanocrystal superlattices. *Science* **2000,** *287*, 1989-1992.

254. Gan, L.; Heggen, M.; Rudi, S.; Strasser, P., Core–Shell Compositional Fine Structures of Dealloyed Pt_xNi_{1-x} Nanoparticles and Their Impact on Oxygen Reduction Catalysis. *Nano Lett.* **2012,** *12*, 5423-5430.

255. Grosvenor, A. P.; Biesinger, M. C.; Smart, R. S.; McIntyre, N. S., New interpretations of XPS spectra of nickel metal and oxides. *Surf. Sci.* **2006,** *600*, 1771-1779.

256. Biesinger, M. C.; Payne, B. P.; Lau, L. W. M.; Gerson, A.; Smart, R. S. C., X-ray photoelectron spectroscopic chemical state quantification of mixed nickel metal, oxide and hydroxide systems. *Surf. Interface Anal.* **2009,** *41*, 324-332.

257. Subbaraman, Enhancing Hydrogen Evolution Acivity in Water Splitting by tailoring Li-$Ni(OH)_2$-Pt interfaces. *Science* **2012,** *334*, 1256-1260.

258. Jayalakshmi, M.; Rao, M. M.; Kim, K. B., Effect of Particle Size on the Electrochemical Capacitance of alpha-$Ni(OH)_2$ in Alkali Solutions. *Int. J. Electrochem. Sci.* **2006,** *1*, 324-333.

259. Zach, M. P.; Penner, R. M., Nanocrystalline nickel nanoparticles. *Advanced Materials* **2000,** *12*, 878-883.

260. Strmcnik, D. S.; Tripkovic, D. V.; van der Vliet, D.; Chang, K. C.; Komanicky, V.; You, H.; Karapetrov, G.; Greeley, J.; Stamenkovic, V. R.; Markovic, N. M., Unique Activity of Platinum Adislands in the CO Electrooxidation Reaction. *J. Am. Chem. Soc.* **2008,** *130*, 15332-15339.

261. Gan, L.; Heggen, M.; Rudi, S.; Strasser, P., Core-shell Compositional Fine Structures of Dealloyed PtxNi1-x Nanoparticles and their Impact on Oxygen Reduction Catalysis. *Nano Lett.* **2012,** *12*, 5423−5430.

262. Gerischer, H., Über den Zusammenhang zwischen dem Mechanismus der elektrolytischen Wasserstoffabscheidung und der Adsorptionsenergie des atomaren Wasserstoffs an verschiedenen Metallen. *Z. Phys. Chem. Neue. Fol.* **1956,** *8*, 137-153.

263. Conway, B. E.; Bockris, J. O. M., Electrolytic Hydrogen Evolution Kinetics and Its Relation to the Electronic and Adsorptive Properties of the Metal. . *J. Chem. Phys.* **1957,** *26*, 532-541.

264. Han, Q.; Liu, K. R.; Chen, J. S.; Wei, X. J., Hydrogen evolution reaction on amorphous Ni-S-Co alloy in alkaline medium. *Int. J. Hydrogen Energy* **2003,** *28*, 1345-1352.

265. Han, Q.; Liu, K. R.; Chen, J. S.; Wei, X. J., A study on the electrodeposited Ni-S alloys as hydrogen evolution reaction cathodes. *Int. J. Hydrogen Energy* **2003,** *28*, 1207-1212.

266. Greeley, J.; Kibler, L.; El-Aziz, A. M.; Kolb, D. M.; Nørskov, J. K., Hydrogen Evolution Over Bimetallic Systems: Understanding the Trends. *Chemphyschem* **2006,** *7*, 1032-1035.

267. Birry, L.; Lasia, A., Studies of the hydrogen evolution reaction on Raney nickel-molybdenum electrodes. *Journal of Applied Electrochemistry* **2004,** *34*, 735-749.

268. Sinflet, J. H., Bimetallic Catalysts - Discoveries, Concepts and Applications. John Wiley & Sons: New York, 1983.

269. Croy, J. R.; Mostafa, S.; Hickman, L.; Heinrich, H.; Roldan Cuenya, B., Bimetallic Pt-Metal Catalysts for the Decomposition of Methanol: Effect of Secondary Metal on the Oxidation State, Activity, and Selectivity of Pt. *Appl. Catal., A* **2008,** *350*, 207-216.

270. Orucu, E.; Gokaliler, F.; Aksoylu, A. E.; Onsan, Z. I., Ethanol Steam Reforming for Hydrogen Production Over Bimetallic Pt-Ni/Al_2O_3. *Catal. Lett.* **2008,** *120*, 198-203.

271. Stottlemyer, A. L.; Ren, H.; Chen, J. G., Reactions of Methanol and Ethylene Glycol on Ni/Pt: Bridging the Materials Gap Between Single Crystal and Polycrystalline Bimetallic Surfaces. *Surf. Sci.* **2009,** *603*, 2630-2638.

272. Tanksale, A.; Beltramini, J. N.; Dumesic, J. A.; Lu, G. Q., Effect of Pt and Pd Promoter on Ni Supported Catalysts - A TPR/TPO/TPD and Microcalorimetry Study. *J. Catal.* **2008,** *258*, 366-377.

273. Stamenkovic, V.; Mun, B. S.; Mayrhofer, K. J. J.; Ross, P. N.; Markovic, N. M.; Rossmeisl, J.; Greeley, J.; Norskov, J. K., Changing the Activity of Electrocatalysts for Oxygen Reduction by Tuning the Surface Electronic Structure. *Angew. Chem. Int. Ed.* **2006,** *45*, 2897-2901.

274. Wu, J. B.; Zhang, J. L.; Peng, Z. M.; Yang, S. C.; Wagner, F. T.; Yang, H., Truncated Octahedral Pt_3Ni Oxygen Reduction Reaction Electrocatalysts. *J. Am. Chem. Soc.* **2010,** *132*, 4984-4985.

275. Chen, S.; Ferreira, P. J.; Sheng, W. C.; Yabuuchi, N.; Allard, L. F.; Shao-Horn, Y., Enhanced Activity for Oxygen Reduction Reaction on "Pt_3CO" Nanoparticles: Direct Evidence of Percolated and Sandwich-Segregation Structures. *J. Am. Chem. Soc.* **2008,** *130*, 13818-13819.

276. Choi, S.-I.; Xie, S.; Shao, M.; Odell, J. H.; Lu, N.; Peng, H.-C.; Protsailo, L.; Guerrero, S.; Park, J.; Xia, X.; Wang, J.; Kim, M. J.; Xia, Y., Synthesis and Characterization of 9 nm Pt–Ni Octahedra with a Record High Activity of 3.3 A/mgPtfor the Oxygen Reduction Reaction. *Nano Lett.* **2013**, 3420-3425.

277. Khan, N. A.; Zellner, M. B.; Chen, J. G., Cyclohexene as a Chemical Probe of the Low-Temperature Hydrogenation Activity of Pt/Ni(111) Bimetallic Surfaces. *Surf. Sci.* **2004,** *556*, 87-100.

278. Chen, J. G.; Qi, S. T.; Humbert, M. P.; Menning, C. A.; Zhu, Y. X., Rational Design of Low-Temperature Hydrogenation Catalysts: Theoretical Predictions and Experimental Verification. *Acta Phys. Chim. Sin.* **2010,** *26*, 869-876.

279. Su, H. Y.; Bao, X. H.; Li, W. X., Modulating the Reactivity of Ni-Containing Pt(111)-Skin Catalysts by Density Functional Theory Calculations. *J. Chem. Phys.* **2008,** *128*, 194701.

280. Komatsu, T.; Tamura, A., Pt_3Co and PtCu Intermetallic Compounds: Promising Catalysts for Preferential Oxidation of CO in Excess Hydrogen. *J. Catal.* **2008,** *258*, 306-314.

281. Li, B. T.; Kado, S.; Mukainakano, Y.; Miyazawa, T.; Miyao, T.; Naito, S.; Okumura, K.; Kunimori, K.; Tomishige, K., Surface Modification of Ni Catalysts with Trace Pt for Oxidative Steam Reforming of Methane. *J. Catal.* **2007,** *245*, 144-155.

282. Oezaslan, M.; Hasché, F.; Strasser, P., *In Situ* Observation of Bimetallic Alloy Nanoparticle Formation and Growth Using High-Temperature XRD. *Chem. Mater.* **2011,** *23*, 2159-2165.

283. Liu, Z.; Yu, C.; Rusakova, I.; Huang, D.; Strasser, P., Synthesis of Pt_3Co Alloy Nanocatalyst *via* Reverse Micelle for Oxygen Reduction Reaction in PEMFCs. *Top. Catal.* **2008,** *49*, 241-250.

284. Scott, R. W.; Datye, A. K.; Crooks, R. M., Bimetallic Palladium-Platinum Dendrimer-Encapsulated Catalysts. *J. Am. Chem. Soc.* **2003,** *123*, 3708-3709.

285. Liu, C.; Wu, X.; Klemmer, T.; Shukla, N.; Yang, X.; Weller, D., Polyol Process Synthesis of Monodispersed FePt Nanoparticles. *J. Phys. Chem. B* **2004,** *108*, 6121-6123.

286. Colon-Mercado, H. R.; Kim, H.; Popov, B. N., Durability Study Of Pt_3Ni_1 Catalysts as Cathode in PEM Fuel Cells. *Electrochem. Commun* **2004,** *6*, 795-799.

287. Wei, Z. D.; Guo, H. T.; Tang, Z. Y., Heat Treatment of Carbon-Based Powders Carrying Platinum Alloy Catalysts for Oxygen Reduction: Influence on Corrosion Resistance and Particle Size. *J. Power Sources* **1996,** *62*, 233-236.

288. Gasteiger, H. A.; Kocha, S. S.; Sompalli, B.; Wagner, F. T., Activity benchmarks and requirements for Pt, Pt-alloy, and non-Pt oxygen reduction catalysts for PEMFCs. *Appl. Catal., B* **2005,** *56*, 9-35.

289. Salgado, J. R. C.; Antolini, E.; Gonzalez, E. R., Structure and Activity of Carbon-Supported Pt-Co Electrocatalysts for Oxygen Reduction. *J Phys Chem B* **2004,** *108*, 17767-17774.

290. Ferreira, P. J.; la O', G. J.; Shao-Horn, Y.; Morgan, D.; Makharia, R.; Kocha, S.; Gasteiger, H. A., Instability of Pt/C Electrocatalysts in Proton Exchange Membrane Fuel Cells - A Mechanistic Investigation. *J. Electrochem. Soc.* **2005,** *152*, A2256-A2271.

291. Bindra, P.; Clouser, S. J.; Yeager, E., Platinum Dissolution in Concentrated Phosphoric-Acid. *J. Electrochem. Soc.* **1979,** *126*, 1631-1632.

292. Strasser, P., Dealloyed Core Shell Fuel Cell Electrocatalysts. *Rev. Chem. Eng.* **2009,** *25*, 255-295.

293. Yang, R. Z.; Strasser, P.; Toney, M. F., Dealloying of Cu_3Pt (111) Studied by Surface X-ray Scattering. *J. Phys. Chem. C.* **2011,** *115*, 9074-9080.

294. Pourovskii, L. V.; Ruban, A. V.; Johansson, B.; Abrikosov, I. A., Antisite-Defect-Induced Surface Segregation in Ordered NiPt Alloy. *Phys. Rev. Lett.* **2003,** *90*, 026105.

295. Dahmani, C. E.; Cadeville, M. C.; Sanchez, J. M.; Moranlopez, J. I., Ni-Pt Phase-Diagram - Experiment and Theory. *Phys. Rev. Lett.* **1985,** *55*, 1208-1211.

296. Oezaslan, M.; Hasché, F.; Strasser, P., *In-situ* High Temperature X-ray Diffraction Study of $PtCu_3$ Alloy Electrocatalyst for PEMFC. *Z. Anorg. Allg. Chem.* **2010,** *636*, 2111-2111.

297. Ghosh, T.; Leonard, B. M.; Zhou, Q.; DiSalvo, F. J., Pt Alloy and Intermetallic Phases with V, Cr, Mn, Ni, and Cu: Synthesis as Nanomaterials and Possible Applications As Fuel Cell Catalysts. *Chem. Mat.* **2010,** *22*, 2190-2202.

298. Wang, D.; Xin, H. L.; Hovden, R.; Wang, H.; Yu, Y.; Muller, D. A.; DiSalvo, F. J.; Abruña, H. D., Structurally Ordered Intermetallic Platinum–Cobalt Core–Shell Nanoparticles with Enhanced Activity and Stability as Oxygen Reduction Electrocatalysts. *Nat. Mater.* **2013,** *12*, 81-87.

299. Lozovoi, A. Y.; Alavi, A.; Finnis, M. W., Surface Stoichiometry and the Initial Oxidation of NiAl(110). *Phys. Rev. Lett.* **2000,** *85*, 610-613.

300. Khan, N. A.; Zellner, M. B.; Murillo, L. E.; Chen, J. G., A Comparison of Similarities and Differences in the Activities of Pt/Ni(111) and Ni/Pt(111) Surfaces. *Catal. Lett.* **2004,** *95*, 1-6.

301. Skoplyak, O.; Menning, C. A.; Barteau, M. A.; Chen, J. G., Reforming of Oxygenates for H_2 Production on 3d/Pt(111) Bimetallic Surfaces. *Top. Catal.* **2008,** *51*, 49-59.

302. Skoplyak, O.; Menning, C. A.; Barteau, M. A.; Chen, J. G., Experimental and Theoretical Study of Reactivity Trends for Methanol on Co/Pt(111) and Ni/Pt(111) Bimetallic Surfaces. *J. Chem. Phys.* **2007,** *127*, 114707.

303. Gasteiger, H. A.; Markovic, N. M., Just a Dream-or Future Reality? *Science* **2009,** *324*, 48-49.

304. Humbert, M. P.; Chen, J. G., Correlating Hydrogenation Activity with Binding Energies of Hydrogen and Cyclohexene on M/Pt(111) (M = Fe, Co, Ni, Cu) Bimetallic Surfaces. *J. Catal.* **2008,** *257*, 297-306.

305. Nashner, M. S.; Frenkel, A. I.; Somerville, D.; Hills, C. W.; Shapley, J. R.; Nuzzo, R. G., Core Shell Inversion During Nucleation and Growth of Bimetallic Pt/Ru Nanoparticles. *J. Am. Chem. Soc.* **1998,** *120*, 8093-8101.

306. Wang, G.; Vanhove, M.; Ross, P.; Baskes, M., Quantitative Prediction of Surface Segregation in Bimetallic Pt–M Alloy Nanoparticles (M=Ni,Re,Mo). *Prog Surf Sci* **2005**, 28-45.

307. Menning, C. A.; Chen, J. G., Thermodynamics and Kinetics of Oxygen-Induced Segregation of 3d Metals in Pt-3d-Pt(111) and Pt-3d-Pt(100) Bimetallic Structures. *J. Chem. Phys.* **2008,** *128*, 164703.

308. Menning, C. A.; Chen, J. G., General Trend for Adsorbate-Induced Segregation of Subsurface Metal Atoms in Bimetallic Surfaces. *J. Chem. Phys.* **2009,** *130*, 174709.

309. Mu, R. T.; Fu, Q.; Liu, H. Y.; Tan, D. L.; Zhai, R. S.; Bao, X. H., Reversible Surface Structural Changes in Pt-based Bimetallic Nanoparticles During Oxidation and Reduction Cycles. *Appl. Surf. Sci.* **2009,** *255*, 7296-7301.

310. Xu, C. X.; Liu, Y. Q.; Zhou, C.; Wang, L.; Geng, H. R.; Ding, Y., An *In Situ* Dealloying and Oxidation Route to Co_3O_4 Nanosheets and Their Ambient-Temperature CO Oxidation Activity. *Chemcatchem* **2011,** *3*, 399-407.

311. Schubert, M. M.; Kahlich, M. J.; Feldmeyer, G.; Huttner, M.; Hackenberg, S.; Gasteiger, H. A.; Behm, R. J., Bimetallic PtSn Catalyst for Selective CO Oxidation in H_2-Rich Gases at Low Temperatures. *Phys. Chem. Chem. Phys.* **2001,** *3*, 1123-1131.

312. Stamenkovic, V.; Arenz, M.; Blizanac, B. B.; Mayrhofer, K. J. J.; Ross, P. N.; Markovic, N. M., *In situ* CO Oxidation on Well Characterized Pt_3Sn(hkl) Surfaces: A Selective Review. *Surf. Sci.* **2005,** *576*, 145-157.

313. Yang, D. Q.; Sacher, E., Interaction of Evaporated Nickel Nanoparticles with Highly Oriented Pyrolytic Graphite: Back-Bonding to Surface Defects, as Studied by X-Ray Photoelectron Spectroscopy. *J. Phys. Chem. B* **2005,** *109*, 19329-19334.

314. Behafarid, F.; Roldan Cuenya, B., Coarsening Phenomena of Metal Nanoparticles and The Influence of the Support Pre-Treatment: Pt/TiO_2(110). *Surf. Sci.* **2012,** *606*, 908-918.

315. Jak, M. J. J.; Konstapel, C.; van Kreuningen, A.; Chrost, J.; Verhoeven, J.; Frenken, J. W. M., The Influence of Substrate Defects on the Growth Rate of Palladium Nanoparticles on a TiO_2(110) Surface. *Surf. Sci.* **2001,** *474*, 28-36.

316. Belton, D. N.; Sun, Y. M.; White, J. M., Metal-Support Interactions on Rhodium and Platinum/Titanium Dioxide Model Catalysts. *J. Phys. Chem.* **1984,** *88*, 5172-5176.

317. Park, J. B.; Conner, S. F.; Chen, D. A., Bimetallic Pt-Au Clusters on TiO_2(110): Growth, Surface Composition, and Metal-Support Interactions. *J. Phys. Chem. C.* **2008,** *112*, 5490-5500.

318. Porsgaard, S.; Ono, L. K.; Zeuthen, H.; Knudsen, J.; Schnadt, J.; Merte, L. R.; Chevallier, J.; Helveg, S.; Salmeron, M.; Wendt, S.; Besenbacher, F., *In Situ* Study of CO Oxidation on HOPG-Supported Pt Nanoparticles. *ChemPhysChem* **2013**, 1553-1557.

319. Porsgaard, S.; Merte, L. R.; Ono, L. K.; Behafarid, F.; Matos, J.; Helveg, S.; Salmeron, M.; Roldan Cuenya, B.; Besenbacher, F., Stability of Platinum Nanoparticles Supported on SiO_2/Si(111): A High-Pressure X-ray Photoelectron Spectroscopy Study. *ACS Nano.* **2012**, 10743-10749.

320. Dai, W. L.; Qiao, M. H.; Deng, J. F., XPS Studies on a Novel Amorphous Ni-Co-W-B Alloy Powder. *Appl. Surf. Sci.* **1997,** *120*, 119-124.

321. Grunthaner, P. J.; Grunthaner, F. J.; Mayer, J. W., Xps Study of the Chemical-Structure of the Nickel-Silicon Interface. *J. Vac. Sci. Technol.* **1980,** *17*, 924-929.

322. Li, F. B.; Li, X. Z., The Enhancement of Photodegradation Efficiency Using Pt-TiO_2 Catalyst. *Chemosphere* **2002,** *48*, 1103-1111.

323. Rajalakshmi, N.; Ryu, H.; Shaijumon, M. M.; Ramaprabhu, S., Performance of Polymer Electrolyte Membrane Fuel Cells with Carbon Nanotubes as Oxygen Reduction Catalyst Support Material. *J. Power Sources* **2005,** *140*, 250-257.

324. Wen, Y. N.; Zhang, H. M., Surface Energy Calculation of the Fcc Metals by Using the MAEAM. *Solid State Commun.* **2007,** *144*, 163-167.

325. Deng, L.; Hu, W.; Deng, H.; Xiao, S.; Tang, J., Au–Ag Bimetallic Nanoparticles: Surface Segregation and Atomic-Scale Structure. *J. Phys. Chem. C* **2011,** *115*, 11355-11363.

326. Cheng, D.; Yuan, S.; Ferrando, R., Structure, Chemical Ordering and Thermal Stability of Pt–Ni Alloy Nanoclusters. *J. Phys. Condens Matter.* **2013,** *25*, 1-9.

327. Abrikosov, I.; Ruban, A.; Skriver, H.; Johansson, B., Calculated Orientation Dependence of Surface Segregations in $Pt_{50}Ni_{50}$. *Phys Rev B* **1994,** *50*, 2039-2042.

328. Heggen, M.; Oezaslan, M.; Houben, L.; Strasser, P., Formation and Analysis of Core–Shell Fine Structures in Pt Bimetallic Nanoparticle Fuel Cell Electrocatalysts. *J. Phys. Chem. C.* **2012,** *116*, 19073-19083.

329. Li, W.; Österlund, L.; Vestergaard, E.; Vang, R.; Matthiesen, J.; Pedersen, T.; Lægsgaard, E.; Hammer, B.; Besenbacher, F., Oxidation of Pt(110). *Phys. Rev. Lett.* **2004,** *93*, 146104.

330. Cui, C. H.; Gan, L.; Heggen, M.; Rudi, S.; Strasser, P., Compositional Segregation in Shaped Pt Alloy Nanoparticles and their Structural Behaviour During Electrocatalysis. *Nat. Mater.* **2013,** *12*, 765-771.

331. Yu, W. T.; Porosoff, M. D.; Chen, J. G. G., Review of Pt-Based Bimetallic Catalysis: From Model Surfaces to Supported Catalysts. *Chem Rev* **2012,** *112*, 5780-5817.

332. Sinfelt, J. H., Catalytic Hydrogenolysis on Metals. *Catal. Lett* **1991,** *9*, 159-172.

333. Rodriguez, J. A.; Goodman, D. W., The Nature of the Metal Metal Bond in Bimetallic Surfaces. *Science* **1992,** *257*, 897-903.

334. Markovic, N. M.; Schmidt, T. J.; Stamenkovic, V.; Ross, P. N., Oxygen Reduction Reaction on Pt and Pt Bimetallic Surfaces: A Selective Review. *Fuel Cells* **2001,** *1*, 105-116.

335. Strasser, P., Dealloyed Core-Shell Fuel Cell Electrocatalysts. *Rev. Chem. Eng.* **2009,** *25*, 255-295.

336. Kitchin, J. R.; Norskov, J. K.; Barteau, M. A.; Chen, J. G., Role of Strain and Ligand Effects in the Modification of the Electronic and Chemical Properties of Bimetallic Surfaces. *Phys. Rev. Lett.* **2004,** *93*.

337. Jiang, Q. A.; Jiang, L. H.; Hou, H. Y.; Qi, J.; Wang, S. L.; Sun, G. Q., Promoting Effect of Ni in PtNi Bimetallic Electrocatalysts for the Methanol Oxidation Reaction in Alkaline Media: Experimental and Density Functional Theory Studies. *J. Phys. Chem. C.* **2010,** *114*, 19714-19722.

338. Pawelec, B.; Damyanova, S.; Arishtirova, K.; Fierro, J. L. G.; Petrov, L., Structural and Surface Features of PtNi Catalysts for Reforming of Methane with CO_2. *Appl. Catal. a-Gen.* **2007,** *323*, 188-201.

339. Nerlov, J.; Sckerl, S.; Wambach, J.; Chorkendorff, I., Methanol Synthesis from CO_2, CO and H_2 over Cu(100) and Cu(100) Modified by Ni and Co. *Appl. Catal. a-Gen.* **2000,** *191*, 97-109.

340. Wu, J.; Zhang, J.; Peng, Z.; Yang, S.; Wagner, F. T.; Yang, H., Truncated Octahedral Pt3Ni Oxygen Reduction Reaction Electrocatalysts. *J. Am. Chem. Soc.* **2010,** *132*, 4984-4985.

341. Chung, Y.-H.; Chung, D. Y.; Jung, N.; Park, H. Y.; Yoo, S. J.; Jang, J. H.; Sung, Y.-E., Origin of the Enhanced Electrocatalysis for Thermally Controlled Nanostructure of Bimetallic Nanoparticles. *J. Phys. Chem. C* **2014,** *118*, 9939-9945.

342. Mu, R.; Fu, Q.; Xu, H.; Zhang, H.; Huang, Y.; Jiang, Z.; Zhang, S.; Tan, D.; Bao, X., Synergetic Effect of Surface and Subsurface Ni Species at Pt−Ni Bimetallic Catalysts for CO Oxidation. *J. Am. Chem. Soc.* **2011,** *133*, 1978-1986.

343. Ahmadi, M.; Behafarid, F.; Cui, C.; Strasser, P.; Roldan Cuenya, B., Long-Range Segregation Phenomena in Shape-Selected Bimetallic Nanoparticles: Chemical State Effects. *ACS Nano* **2013,** *7*, 9195-9204.

344. Stamenkovic, V.; Mun, B. S.; Mayrhofer, K. J. J.; Ross, P. N.; Markovic, N. M.; Rossmeisl, J.; Greeley, J.; Nørskov, J. K., Changing the Activity of Electrocatalysts for Oxygen Reduction by Tuning the Surface Electronic Structure. *Angew. Chem.* **2006,** *118*, 2963-2967.

345. Su, H. Y.; Bao, X. H.; Li, W. X., Modulating the Reactivity of Ni Containing Pt(111)-skin Catalysts by Density Functional Theory Calculations. *J. Chem. Phys.* **2008,** *128*.

346. Jiang, Q. A.; Jiang, L. H.; Wang, S. L.; Qi, J.; Sun, G. Q., A Highly Active PtNi/C Electrocatalyst for Methanol Electro-oxidation in Alkaline Media. *Catal Commun* **2010,** *12*, 67-70.

347. Antolini, E.; Salgado, J. R. C.; Gonzalez, E. R., The Methanol Oxidation Reaction on Platinum Alloys with the first Row Transition Metals - The case of Pt-Co and -Ni Alloy Electrocatalysts for DMFCs: A short review. *Appl Catal B-Environ* **2006,** *63*, 137-149.

348. Greeley, J.; Nørskov, J. K.; Kibler, L. A.; El-Aziz, A. M.; Kolb, D. M., Hydrogen Evolution Over Bimetallic Systems: Understanding the Trends. *ChemPhysChem* **2006,** *7*, 1032-1035.

349. Greeley, J.; Stephens, I. E. L.; Bondarenko, A. S.; Johansson, T. P.; Hansen, H. A.; Jaramillo, T. F.; Rossmeisl, J.; Chorkendorff, I.; Nørskov, J. K., Alloys of Platinum and Early Transition Metals as Oxygen Reduction Electrocatalysts. *Nature Chemistry* **2009,** *1*, 552-556.

350. Gauthier, Y.; Schmid, M.; Padovani, S.; Lundgren, E.; Bus, V.; Kresse, G.; Redinger, J.; Varga, P., Adsorption Sites and Ligand Effect for CO on an Alloy Surface: a Direct View. *Phys. Rev. Lett.* **2001,** *87*.

351. Skoplyak, O.; Barteau, M. A.; Chen, J. G., Reforming of Oxygenates for H_2 Production: Correlating Reactivity of Ethylene Glycol and Ethanol on Pt(111) and Ni/Pt(111) with Surface d-Band Center. *J Phys Chem B* **2006,** *110*, 1686-1694.

352. Skoplyak, O.; Barteau, M. A.; Chen, J. G., Ethanol and Ethylene Glycol on Ni/Pt(111) Bimetallic Surfaces: A DFT and HREELS Study. *Surf. Sci.* **2008,** *602*, 3578-3587.

353. Nørskov, J. K.; Rossmeisl, J.; Logadottir, A.; Lindqvist, L.; Kitchin, J. R.; Bligaard, T.; Jónsson, H., Origin of the Overpotential for Oxygen Reduction at a Fuel-Cell Cathode. *J Phys Chem B* **2004,** *108*, 17886-17892.

354. Hwu, H. H.; Eng, J.; Chen, J. G., Ni/Pt(111) Bimetallic Surfaces: Unique Chemistry at Monolayer Ni Coverage. *J. Am. Chem. Soc.* **2002,** *124*, 702-709.

355. Khan, N. A.; Zellner, M. B.; Chen, J. G. G., Cyclohexene as a Chemical Probe of the Low-temperature Hydrogenation Activity of Pt/Ni(111) Bimetallic Surfaces. *Surf. Sci.* **2004,** *556*, 87-100.

356. Chen, J. G. G.; Qi, S. T.; Humbert, M. P.; Menning, C. A.; Zhu, Y. X., Rational Design of Low-Temperature Hydrogenation Catalysts: Theoretical Predictions and Experimental Verification. *Acta Phys-Chim Sin* **2010,** *26*, 869-876.

357. di Paola, C.; Baletto, F., Oxygen Adsorption on Small PtNi Nanoalloys. *Phys. Chem. Chem. Phys.* **2011,** *13*, 7701-7707.

358. Radillo-Diaz, A.; Coronado, Y.; Perez, L. A.; Garzon, I. L., Structural and Electronic Properties of PtPd and PtNi Nanoalloys. *Eur Phys J D* **2009,** *52*, 127-130.

359. Pick, S., Tight-binding model of CO adsorption at Pt/Ni(111) surface. *Surf. Sci.* **1996,** *352*, 300-304.

360. Andersson, K. J.; Calle-Vallejo, F.; Rossmeisl, J.; Chorkendorff, I., Adsorption-Driven Surface Segregation of the Less Reactive Alloy Component. *J. Am. Chem. Soc.* **2009,** *131*, 2404-2407.

361. Tomanek, D.; Mukherjee, S.; Kumar, V.; Bennemann, K. H., Calculation of Chemisorption and Absorption Induced Surface Segregation. *Surf. Sci.* **1982,** *114*, 11-22.

362. Menning, C. A.; Hwu, H. H.; Chen, J. G., Experimental and Theoretical Investigation of the Stability of Pt−3d−Pt(111) Bimetallic Surfaces under Oxygen Environment. *J Phys Chem B* **2006,** *110*, 15471-15477.

363. Hirsimaki, M.; Lampimaki, M.; Lahtonen, K.; Chorkendoff, I.; Valden, M., Investigation of the Role of Oxygen Induced Segregation of Cu During Cu_2O Formation on Cu{100}, Ag/Cu{100} and Cu(Ag) Alloy. *Surf. Sci.* **2005,** *583*, 157-165.

364. Christoffersen, E.; Stoltze, P.; Norskov, J. K., Monte Carlo Simulations of Adsorption-induced Segregation. *Surf. Sci.* **2002,** *505*, 200-214.

365. Shu, J.; Bongondo, B. E. W.; Grandjean, B. P. A.; Adnot, A.; Kaliaguine, S., Surface Segregation of Pd-Ag Membranes Upon Hydrogen Permeation. *Surf. Sci.* **1993,** *291*, 129-138.

366. Wang, G. F.; Van Hove, M. A.; Ross, P. N.; Baskes, M. I., Monte Carlo Simulations of Segregation in Pt-Ni Catalyst Nanoparticles. *J. Chem. Phys.* **2005,** *122*.

367. Ma, Y. G.; Balbuena, P. B., Pt Surface Segregation in Bimetallic Pt_3M alloys: A Density Functional Theory Study. *Surf. Sci.* **2008,** *602*, 107-113.

368. Soto-Verdugo, V.; Metiu, H., Segregation at the Surface of an Au/Pd Alloy Exposed to CO. *Surf. Sci.* **2007,** *601*, 5332-5339.

369. Tenney, S. A.; Ratliff, J. S.; Roberts, C. C.; He, W.; Ammal, S. C.; Heyden, A.; Chen, D. A., Adsorbate-Induced Changes in the Surface Composition of Bimetallic Clusters: Pt−Au on TiO_2(110). *J. Phys. Chem. C* **2010,** *114*, 21652-21663.

370. Studt, F.; Abild-Pedersen, F.; Wu, Q.; Jensen, A. D.; Temel, B.; Grunwaldt, J.-D.; Nørskov, J. K., CO Hydrogenation to Methanol on Cu–Ni Catalysts: Theory and Experiment. *J. Catal.* **2012,** *293*, 51-60.

371. Mazzone, G.; Rivalta, I.; Russo, N.; Sicilia, E., Interaction of CO with PdAu(111) and PdAu(100) Bimetallic Surfaces: A Theoretical Cluster Model Study. *J. Phys. Chem. C* **2008,** *112*, 6073-6081.

372. Gao, F.; Wang, Y.; Goodman, D. W., CO Oxidation over AuPd(100) from Ultrahigh Vacuum to Near-Atmospheric Pressures: CO Adsorption-Induced Surface Segregation and Reaction Kinetics. *J. Phys. Chem. C* **2009,** *113*, 14993-15000.

373. Abrikosov, I. A.; Ruban, A. V.; Skriver, H. L.; Johansson, B., Calculated Orientation Dependence of Surface Segregations in $Pt_{50}Ni_{50}$. *Phys Rev B* **1994,** *50*, 2039-2042.

374. Lundberg, M., Surface Segregation and Relaxation Calculated by the Embedded-Atom Method - Application to Face-Related Segregation on Platinum-Nickel Alloys. *Phys. Rev. B.* **1987,** *36*, 4692-4699.

375. Cui, C. H.; Gan, L.; Li, H. H.; Yu, S. H.; Heggen, M.; Strasser, P., Octahedral PtNi Nanoparticle Catalysts: Exceptional Oxygen Reduction Activity by Tuning the Alloy Particle Surface Composition. *Nano Lett.* **2012,** *12*, 5885-5889.

376. Shen, W. M.; Dumesic, J. A.; Hill, C. G., Criteria for Stable Ni Particle-Size under Methanation Reaction Conditions - Nickel Transport and Particle-Size Growth Via Nickel Carbonyl. *J. Catal.* **1981,** *68*, 152-165.

377. Mond, L.; Langer, C.; Quincke, F., Action of Carbon-Monoxide on Nickel (Reprinted from J Chem Soc, Vol 57, Pg 749-753, 1890). *J. Organomet. Chem.* **1990,** *383*, 1-5.

378. Croy, J. R.; Mostafa, S.; Liu, J.; Sohn, Y. H.; Roldan Cuenya, B., Size Dependent Study of MeOH Decomposition Over Size-selected Pt Nanoparticles Synthesized via Micelle Encapsulation. *Catal. Lett.* **2007,** *118*, 1-7.

379. Furstenau, R. P.; Mcdougall, G.; Langell, M. A., Initial-Stages of Hydrogen Reduction of NiO(100). *Surf. Sci.* **1985,** *150*, 55-79.

380. Mansour, A. N., Characterization of NiO by XPS. *Surf. Sci. Spectra* **1994,** *3*, 231.

381. Bianchi, C. L.; Cattania, M. G.; Villa, P., Xps Characterization of Ni and Mo Oxides before and after Insitu Treatments. *Appl. Surf. Sci.* **1993,** *70-1*, 211-216.

382. Kishi, K.; Motoyoshi, Y.; Ikeda, S., Deposition of Nickel from $Ni(CO)_4$ on Palladium and iron Surfaces Studied by X-ray Photoelectron Spectroscopy. *Surf. Sci.* **1981,** *105*, 313-324.

383. Choi, E.; Oh, S. J.; Choi, M., Charge-Transfer in Ni_xPt_{1-X} Alloys Studied by X-Ray Photoelectron-Spectroscopy. *Phys. Rev. B.* **1991,** *43*, 6360-6368.

384. Falconer, J. L.; Schwarz, J. A., Temperature-Programmed Desorption and Reaction - Applications to Supported Catalysts. *Catal. Rev.* **1983,** *25*, 141-227.